

Department of Mechanical Engineering

**A Study of the Interaction Between Inviscid Flow and a
Cantilevered Flexible Plate**

Reilly Owen George Evetts

**This thesis is presented for the Degree of
Doctor of Philosophy
of
Curtin University**

December 2017

Declaration


To the best of my knowledge and belief this thesis contains no material previously published by any other person except where due acknowledgement has been made. This thesis contains no material which has been accepted for the award of any other degree or diploma in any university.

All investigations presented in this thesis are my own except where specific reference has been made to the work of others. Some of the work presented in this thesis has been published in the following:

R. O. G. Evetts, R. M. Howell, and A. D. Lucey. A new model for wake effects upon a cantilevered flexible plate undergoing continuous oscillation due to a high Reynolds Number axial flow. In *Proceedings of the 19th Australasian Fluid Mechanics Conference*, December 2014.

R. O. G. Evetts, R. M. Howell, and A. D. Lucey. Modelling of a cantilevered flexible plate undergoing large-amplitude oscillations due to a high Reynolds Number axial flow. In *Proceedings of the 3rd Symposium on Fluid-Structure-Sound Interactions and Control*, July 2015.

R. O. G. Evetts, R. M. Howell, and A. D. Lucey. Modelling of a cantilevered flexible plate undergoing large-amplitude oscillations due to a high Reynolds Number axial flow. In *Proceedings of the 19th Australasian Fluid Mechanics Conference*, December 2018.

Signature: 

Date: 01/04/2019

Attribution Of Research Outputs

Table 1: R. O. G. Evetts, R. M. Howell, and A. D. Lucey. A new model for wake effects upon a cantilevered flexible plate undergoing continuous oscillation due to a high Reynolds Number axial flow. In *Proceedings of the 19th Australasian Fluid Mechanics Conference*, December 2014.

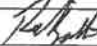

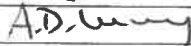
	Literature	Modelling	Analysis	Interpretation & Discussion	Paper Writing, Preparation, & Final Approval
R.O.G. Evetts	x	x	x	x	x
I acknowledge that these represent my contribution to the above research output					
Signed:					
Dr. R.M. Howell				x	x
I acknowledge that these represent my contribution to the above research output					
Signed:					
Prof. A.D. Lucey				x	x
I acknowledge that these represent my contribution to the above research output					
Signed:					

Table 2: R. O. G. Evetts, R. M. Howell, and A. D. Lucey. Modelling of a cantilevered flexible plate undergoing large-amplitude oscillations due to a high Reynolds Number axial flow. In *Proceedings of the 3rd Symposium on Fluid-Structure-Sound Interactions and Control*, July 2015.



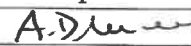
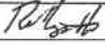


	Literature	Modelling	Analysis	Interpretation & Discussion	Paper Writing, Preparation, & Final Approval
R.O.G. Evetts	x	x	x	x	x
I acknowledge that these represent my contribution to the above research output					
Signed:					
Dr. R.M. Howell				x	x
I acknowledge that these represent my contribution to the above research output					
Signed:					
Prof. A.D. Lucey				x	x
I acknowledge that these represent my contribution to the above research output					
Signed:					

Table 3: R. O. G. Evetts, R. M. Howell, and A. D. Lucey. Modelling of a cantilevered flexible plate undergoing large-amplitude oscillations due to a high Reynolds Number axial flow. In *Proceedings of the 19th Australasian Fluid Mechanics Conference*, December 2018.

	Literature	Modelling	Analysis	Interpretation & Discussion	Paper Writing, Preparation, & Final Approval
R.O.G. Evetts	x	x	x	x	x
I acknowledge that these represent my contribution to the above research output					
Signed:					
Dr. R.M. Howell				x	x
I acknowledge that these represent my contribution to the above research output					
Signed:					
Prof. A.D. Lucey				x	x
I acknowledge that these represent my contribution to the above research output					
Signed:					

Abstract

New models are presented which explore the fluid-structure interaction between a cantilevered flexible plate and an ideal, axial flow giving rise to a flutter instability. The Euler-Bernoulli beam equation, a potential flow model, and the discrete vortex method are coupled and used to model the solid, irrotational flow component, and wake respectively. Particular attention is paid to the role of the wake formed as a result of this interaction, its effect on the system stability, and the extent to which it needs to be modelled.

Firstly linearised models are developed to examine the limits of flutter onset making use of both time-dependent initial-value and infinite-time boundary-value methods to explore the effect of coarsening the wake discretisation. Two different interpretations of the Kelvin condition are made allowing the wake effect to be included in the eigenvalue problem leading to two separate models where the strength of the wake is lumped into a single discrete vortex. It is shown that these single-vortex models are able to capture the same overall trends as the full-wake model with regard to the limits of instability onset, one of the models comparing very well for low mass ratios and showing a similar stabilising-to-destabilising wake effect with increasing mass ratio as found in the literature. A new effect is found because it is shown that the fluid-to-plate density ratio is a further non-dimensional control parameter necessary for categorising systems which include a wake which arises as a result of the Kutta condition.

Secondly a model capable of simulating non-linear disturbances is developed which takes account of boundary-layer separation from the surface of the plate upstream of its trailing edge. It is shown that at the flow speed for which the system is stable in the linear regime, flow separation can lead to the sub-critical flutter instability found in experiments presented in the literature.

The new methods developed make significant contributions to the numerical modelling and understanding of the flutter instability in cantilevered plates, showing that the density ratio is a further non-dimensional parameter which must be considered when modelling the system with a wake, and that the formation of a boundary-layer is capable of explaining the sub-critical instability found in experimental studies.

Nomenclature

$[\mathbf{A}]$, $[\mathbf{B}]$... Combined influence coefficient matrices

$[I]_{im}$ Influence coefficient of panel i on panel m

α Wake vortex core size (m)

\bar{L} Mass ratio

\bar{U} Non-dimensional flow speed

$\delta p|_{xp}$ Pressure difference across the plate (kg/ms^2)

δs Panel length (m)

δt Time step size (s)

δx Horizontal distance between panels (m)

η Vertical node displacement (m)

γ Distributed Zero-order singularity strength (m/s)

Γ^b Wake vortex strength (m^2/s)

λ First-order singularity strength (m/s)

ϕ Velocity perturbation potential (m^2/s)

ρ Plate density (kg/m^3)

ρ_f Fluid density (kg/m^3)

θ Panel angle to the horizontal (rad)

\underline{n} Unit normal vector (m)

\underline{t}	Unit tangent vector (m)
\underline{u}	Total flow velocity (m/s)
\underline{u}'	Total perturbation velocity (m/s)
\underline{u}_p^b	Wake-induced velocity vector at point p (m/s)
\underline{v}	Plate velocity vector (m/s)
ξ	Horizontal node position (m)
ζ_f	Vorticity in the flow (m ² /s)
B	Flexural rigidity (Nm)
d	Damping coefficient (kg/sm ²)
E	Young's modulus (N/m ²)
E_k	Plate kinetic energy (Nm)
E_s	Plate strain energy (Nm)
E_t	Plate total energy (Nm)
h	Plate thickness (m)
L	Plate length (m)
L_r	Reference length (m)
L_w	Wake length (m)
M	Number of panels
N	Number of plate mass points
N_b	Number of wake vortices
p	Pressure acting on the plate (kg/ms ²)
s	Distance along the plate (m)
T	Time period (s)

T_r Reference time (s)

U_∞ Flow speed (m/s)

U_c^*, U_c Critical flow speed with and without a wake (m/s)

Contents

Nomenclature	vii
List of Figures	xvii
List of Tables	xviii
I Introduction and Literature Review	1
1 Introduction	2
1.1 Overview	2
1.1.1 Flags	3
1.1.2 Snoring	3
1.1.3 Energy Generation	4
1.1.4 Biocomotion	5
1.2 Research Overview	6
1.2.1 Problem Statements	7
1.2.2 Methodology	7
1.2.3 Scope and Assumptions	8
1.2.4 Objectives and Contributions	8
1.3 Thesis layout	10
2 Literature Review	12
2.1 Introduction to Instability	12
2.2 Experimental Studies	14
2.3 Theoretical Studies	17
2.3.1 Linear Plate Deflection	18

2.3.2	Non-Linear Plate Deflection	22
2.4	Motivation	30
II	Linear Model	32
3	Theory	33
3.1	Plate Model	33
3.1.1	Boundary Conditions	35
3.1.2	Natural Frequencies	36
3.2	Fluid Model	37
3.2.1	Steady Flow Model	37
3.2.2	Wake Model	40
3.2.3	Unsteady Flow Model	43
3.3	Computational Model Assembly	45
3.3.1	Initial Value Problem	46
3.3.2	Eigenanalysis	49
3.3.3	System Non-dimensionalisation	52
4	Validation	54
4.1	Plate Model	54
4.2	Fluid Model	56
4.3	Unsteady Model	57
4.4	Wake Model	61
4.5	Full Numerical Model	61
4.6	Summary	62
5	Results	64
5.1	Initial-value (Numerical Simulation) Results	64
5.2	Boundary-value Results	66
5.3	Fluid Density Variations	69
6	Summary	74

III	Non-Linear Model	76
7	Theory	77
7.1	Beam Model	77
7.2	Fluid Model	79
7.2.1	Steady Flow Model	79
7.2.2	Wake Model	81
7.2.3	Unsteady Flow Model	82
7.3	Computational Model Assembly	84
7.3.1	Separation	85
7.3.2	System Non-dimensionalisation	86
8	Validation	88
8.1	Plate Model	88
8.2	Fluid Model	92
8.3	Unsteady Model	93
8.4	Wake Model	93
8.5	Full Numerical Model	95
8.5.1	Separation	96
8.6	Summary	101
9	Results	102
9.1	Pressure Threshold Variation	102
9.2	Hysteresis	104
9.3	Model Variation	105
10	Summary	111
IV	Conclusions	113
11	Conclusions and Further Work	114
11.1	Conclusions	114
11.1.1	Small-Amplitude Oscillations	114
11.1.2	Large-Amplitude Oscillation	115

11.2 Further Work	117
11.2.1 Linear Model	117
11.2.2 Non-Linear Model	118
Bibliography	120
Appendices	129
A Linear Equations	129
A.1 Normal Matrix	129
A.2 Pressure Equation	129
A.3 Steady Singularity Strengths	130
A.4 Unsteady Singularity Strengths	131
A.5 Expanded Pressure Equation	132
A.5.1 A^- and B^- :	132
A.5.2 A^+ :	133
A.6 The $[I^{N-+}]$ and $[I^{N+}]$ matrices	134
B Non-linear Equations	136
B.1 Non-linear Beam Disretization	136
B.2 Steady and Unsteady Singularity Strengths	138
B.2.1 Tangential Perturbation Velocity	139
B.2.2 Unsteady Velocity Potential	139
B.3 Pressure Equation	140

List of Figures

1.1	An example of the system studied when considering the fluttering motion of a flag adapted from Eloy et al. [2008].	2
1.2	From Aurégan and Depollier [1995], (a) A schematic of the human upper-airway, (b) a model of the pharynx examined in studies of snoring.	4
1.3	(a) The energy harvesting eel from Allen and Smits [2001], (b) a schematic of the flutter mill proposed by Tang et al. [2009b].	5
1.4	A figure from Müller [2003] showing the vortices and jets (arrows) which make up the wake behind a (a) flag, (b) bluff body, and (c) and (d) show the wake behind a swimming fish in moving flow.	6
2.1	The experiments of Zhang et al. [2000] showing the flexible filament deflection and associated wake in low speed flow (a). The deflection, wake, and tip displacement in a high speed flow are shown in (b) and (c) respectively.	15
2.2	Adapted from Eloy et al. [2008], showing the experimental setup.	16
2.3	The graph presented in Watanabe et al. [2002b] demonstrating the trend and discrepancy between a collection of theoretical (continuous data) and experimental (discrete data) results for critical velocity plotted against mass ratio (\bar{L}) in the literature.	20
2.4	The transition between the three instability regimes for a flag of constant rigidity and the general form of the wake associated with each regime. From Connell and Yue [2007].	26
3.1	The linear system modelled. Those vortices in the dashed box apply only to the full numerical simulation.	33

3.2	Beam discretization	34
3.3	Modal deflections for the first four eigenmodes.	37
3.4	Singularity distribution along the cantilever.	40
3.5	The system studied in the full numerical simulation.	46
3.6	The system solved through eigenanalysis.	47
4.1	<i>In vacuo</i> plate model using 50 nodes initially deflected into the first four eigenmodes in a, b, c, and d respectively. The total, strain, and kinetic energies are the solid, dashed, and dotted lines respectively in each subfigure.	56
4.2	The total (—), kinetic (⋯), and strain (---) energies, (a), and tip deflection, (b), of a cantilever initially deflected into the second mode with damping $d = 0.05 \text{ kg/sm}^2$ using 50 nodes.	57
4.3	Fluid model results comparison between the current model (+), and experimental (Δ) and theoretical (\bullet) results obtained by Houghton and Carpenter [1993] for a NACA 4412 aerofoil at an 8° angle of attack.	58
4.4	Pressure distribution and deflection given by the current model (right) and that in Howell [2006] (left, centre). 50 nodes are used and the plate is deflected in to the first three normal modes in rows 1, 2, and 3 respectively.	58
4.5	The energy and deflection of a cantilever plate at; (top) $U_\infty < U_c$, (middle) $U_\infty = U_c$, and (bottom) $U_\infty > U_c$. The initial and final deflections are shown by the blue and red lines respectively.	60
4.6	The wake following a heaving plate (not shown) of length, $L = 0.12 \text{ m}$, frequency, $f = 0.8 \text{ Hz}$, $U_\infty = 0.05 \text{ m/s}$, given by (a) the present numerical model, plotted with the trailing edge of the cantilever at $x/L = 0$, after 200 time steps using vortices of core size 0.4 m ($\approx 3L$), and (b) an example of the experimental results presented in Paraz et al. [2014].	63

5.1 Variation of critical speed with mass ratio from the numerical simulation of the initial-value model for (a) fully discretised wake model, and (b) wake modelled by a single vortex. In each of these the no-wake, full (with jerk) and no-jerk results are shown by - - -, * and • respectively. (c) and (d) show the plate deflections over one oscillation for $\bar{L} = 1$ and 10 using the full numerical simulation model. 65

5.2 (a) A comparison of instability-onset flow speeds obtained from the two boundary-value models, + using Equation 3.3.12a (model 1) and • using Equation 3.3.12b (model 2), with the results of numerical simulations, * with a fully discretised wake and - - - with no wake. (b) and (c) show the plate deflections over one oscillation for $\bar{L} = 1$ and 10 using model 1 while (d) and (e) show the plate deflections over one oscillation for $\bar{L} = 1$ and 10 using model 2. 68

5.3 Variation of critical velocities with density ratio for constant \bar{L} values predicted by the numerical simulation (left) and boundary-value model (right). Each line is the critical velocity given by: numerical simulation with * for a fully discretised wake and - - - for no wake, and Δ for the first boundary-value model with a wake (noting that with the wake effects suppressed, the boundary-value model gives the same results as the numerical simulation without a wake). The limit of the thin plate assumption where $L/h \geq 10$ is shown by the thick dashed line. 72

5.4 Eigenvalue plots at $\bar{L} = 1, 2,$ and 4 in the left, middle, and right columns respectively. Where the top and bottom rows are at $\rho_f/\rho = 4 \times 10^{-4}$ and 0.19 respectively (the x -limits of Figure 5.3). The solid and dashed lines represent the real and imaginary eigenvalue components respectively. 73

7.1 Schematic of the system studied and the approach taken to model separation. 77

7.2 Beam discretization 78

7.3	Boundary-element panel arrangement for the non-linear plate. . . .	80
7.4	Representation of the free-shear layers that form at the point of separation and from the plate trailing edge.	83
8.1	The cantilever model in the first four modes and their associated energies during one oscillation using 200 nodes. (a), (b), (c), and (d) show the first through fourth modes respectively. The total, strain, and kinetic energies are the solid, dashed, and dotted lines respectively in each subfigure.	90
8.2	Effect of amplitude on mode shape and tip deflection in the current model (d), (e), and (f) compared to the equivalent figures in Elliot et al. [2010] reproduced in (a), (b), and (c).	91
8.3	Convergence of model frequency, ω , to the linear theory at small amplitudes compared to that presented in Elliot et al. [2010] (left).	91
8.4	The pressure difference across the plate given by the present model (—) and the linear theory (- -) at increasing amplitude.	92
8.5	The plate deflection (left), tip deflection (middle), and energy (right) in time at $\bar{U} = 5.50$ (top) and $\bar{U} = 7.16$. The initial and final deflections are shown by the blue and red lines in the left column of figures respectively.	94
8.6	Tip deflections at increasing flow speed produced by the linear and non-linear fluid models without a wake.	95
8.7	The wake roll-up found by the current model (c) and (d) compared to the equivalent figures in Alben and Shelley [2008], adapted in (a) and (b). Where (a) and (c) are at $\bar{U} = 7.58$, and (b) and (d) are at $\bar{U} = 7.77$	95
8.8	A comparison between the full numerical model (right) with no shear-layer separation, and the results presented by Tang and Paidoussis [2007] (left) for $\bar{L} = 0.2$ and $\bar{U} = 59.15$	97

- 8.9 The wake formed behind a circular cylinder submerged in water, with a diameter of 1cm, and a flow speed of 1.4cm/s adapted from Van Dyke [1982] (top) and given by the present numerical model (bottom). Where the colour represents the sign of the vorticity, positive (green), negative (red), and the marker denotes the surface the vortex has been released from; upper (Δ), or lower (+). 98
- 8.10 The coefficient of lift predicted by the current model, thin aerofoil theory, and the experimental results of Abbott and Von Doenhoff [1959] for the (a) NACA 0012 and (b) NACA 4412 aerofoils. 100
- 9.1 The deflection predicted for $\bar{L} = 1$, and $\bar{U} = 7.16$ where each row from top to bottom represents the results when $P_{\text{thresh}} = 10.0, 0.1, 0.01, 0.001$, and 0.0 . In each row the first column of figures shows snapshots of the beam deflection at regular intervals throughout the experiment with the blue and red lines showing the initial and final displacement respectively. The second and third columns show a trace of the vertical tip deflection and beam energy in time. 107
- 9.2 The deflection predicted for (a) $\eta_L^{t=0} = 0.01L$, (b) $\eta_L^{t=0} = 0.1L$, and (c) $\eta_L^{t=0} = 0.2L$. Each line represents the results for a different threshold pressure value; $P_{\text{thresh}} = 0.001$ (\star), $P_{\text{thresh}} = 0.01$ (\bullet), $P_{\text{thresh}} = 0.1$ (\times). $P_{\text{thresh}} = 10.0$ is shown by the dashed line. 108
- 9.3 The maximum stable deflection achieved when first increasing and then decreasing the flow speed for (a) $P_{\text{thresh}} = 0.001$, (b) $P_{\text{thresh}} = 0.01$, and (c) $P_{\text{thresh}} = 0.1$. In each case the dashed and solid lines represent the deflection achieved when increasing and decreasing the flow speed respectively. 108
- 9.4 The hysteresis loop found in experiment for $\bar{L} = 1$, adapted from Watanabe et al. [2002a]. Where the black marker indicates the flow speed at which the oscillations began. 108

9.5 The maximum deflection achieved using a modified version of the non-linear model once the system has entered self-sustaining oscillations at various pressure gradient thresholds for $\bar{L} = 1$. The dashed and solid lines represent the results when the flow speed is increased and decreased respectively. 109

9.6 Oscillation of a cantilevered plate in axial flow at $\bar{L} = 1$. Within each group of sub-figures, the top row shows the results when wake formation is restricted to the trailing edge, and the bottom row shows corresponding results when separation is allowed to occur upstream of the trailing edge. The first column of sub-figures are snapshots in time of plate displacement; blue and red profiles are respectively the initial and final deflections. Second and third columns respectively show time series of plate-tip deflection and plate energy, the latter normalised by the strain energy of the plate in its initial deflection. 110

B.1 Normal and tangential directions on the upper and lower surfaces of wake-induced and plate-induced velocities. 141

List of Tables

4.1	Simulated oscillation frequencies at various levels of discretization.	56
4.2	Dependence of critical speed on mass ratio (non-dimensional plate length) and comparison of present results with those of Howell et al. [2009].	62
8.1	Simulated oscillation frequencies at various levels of discretization.	89

Part I

Introduction and Literature

Review

Chapter 1

Introduction

1.1 Overview

Fluid-Structure Interaction (FSI) is a widespread phenomenon which appears in many forms. The particular phenomenon under consideration in this study is the flutter of cantilevered plates in very high Reynolds number flows that predominate in engineering applications. The flutter of a flexible surface in a uniform stream has been studied extensively and has many applications including: predicting the motion of flags, human snoring, energy harvesting, and the propulsion/movement of fish. The results of the study presented in this thesis will enhance our understanding of the underlying physics of the flutter phenomenon and has applications in the modelling of each of these situations.

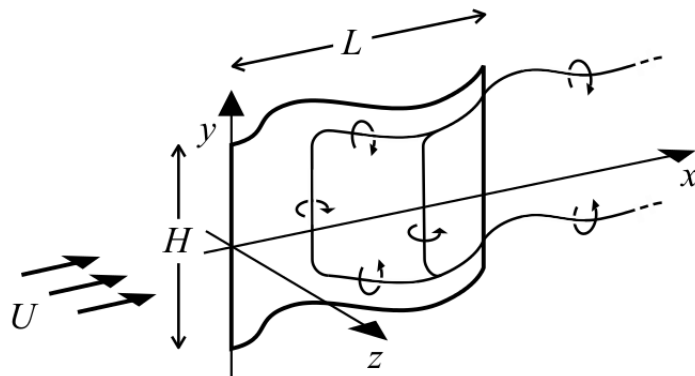


Figure 1.1: An example of the system studied when considering the fluttering motion of a flag adapted from Eloy et al. [2008].

1.1.1 Flags

The study of flutter extends back as far as the work of Rayleigh [1879] who considered the motion of flags in wind, shown schematically in Figure 1.1, an area which has been the focus of many studies since, such as the work of Argentina and Mahadevan [2008] who were able to predict the critical speed for the onset of instability. However, a consistent discrepancy between the experimental and numerical results presented in the literature was noted by Eloy et al. [2008]. This discrepancy takes the form of a hysteresis loop that manifests itself as a subcritical instability found in experiments but not present in most numerical models. Specifically, the onset of instability as flow rate is increased is found to occur at a higher velocity than that at which instability disappears as the flow rate is reduced. This subcritical hysteresis loop is not reflected in theoretical studies. For example Tang et al. [2003] found this bifurcation in their experiments; however they were unable to reproduce it with the model presented in the same paper. Eloy et al. [2012] performed a weakly non-linear analysis to test several hypotheses presented in other papers and concluded that the large hysteresis found in experiments was due to inherent planar defects arising from the manufacturing process. The numerical models were unable to produce as large a hysteresis as their experimental results but were in agreement with other works such as Tang and Paidoussis [2007] and Michelin et al. [2008]. Connell and Yue [2007] have made perhaps the most complex study of the flapping motion of a flag to date, and describe distinct regimes of response relative to the fluid-to-plate mass ratio, showing that the Duffing equation is a suitable way to describe hysteresis and that the flag is analogous to a soft non-linear spring. They also show that the mass ratio is directly linked to the stability and type of instability experienced by the flag.

1.1.2 Snoring

Another area examined, human snoring, differs from the flag flutter system in that the structural forces are dominated by the flexural rigidity, whereas in the flag problem these are dominated by the induced tension owing to large amplitude deflections. Figure 1.2 demonstrates the layout of the human upper airway and

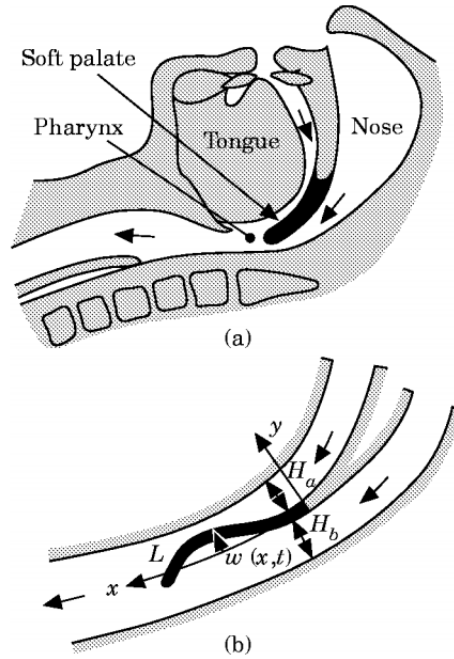


Figure 1.2: From Aurégan and Depollier [1995], (a) A schematic of the human upper-airway, (b) a model of the pharynx examined in studies of snoring.

the location of the soft palate, the flutter of which is responsible for snoring. Some examples are the work of Huang [1995] and Howell et al. [2009], who sought to suggest alternative treatments to traditional surgical approaches. Both studies confined themselves to the limit of linear deflection amplitudes, meaning that non-linear effects could be ignored, as these studies were primarily concerned with flutter onset before the plate enters finite-amplitude oscillation. Howell et al. [2009] extended the model presented by Huang [1995] to include the effect of a linearised wake on the fluid-structure system but did not include this in the boundary-value model presented in the same paper. Both Huang and Howell et al. were able to show that the stiffening of portions of the soft palate could delay the onset of instability, leading to new methods for treating snoring. These papers are covered in more detail in Section 2.3.1, which discusses model exploring small amplitude deflection systems.

1.1.3 Energy Generation

Alternative supplies of energy are becoming increasingly more important as the world moves towards harnessing renewable resources. A large amount of energy is contained within naturally occurring fluid flow and a number of methods have

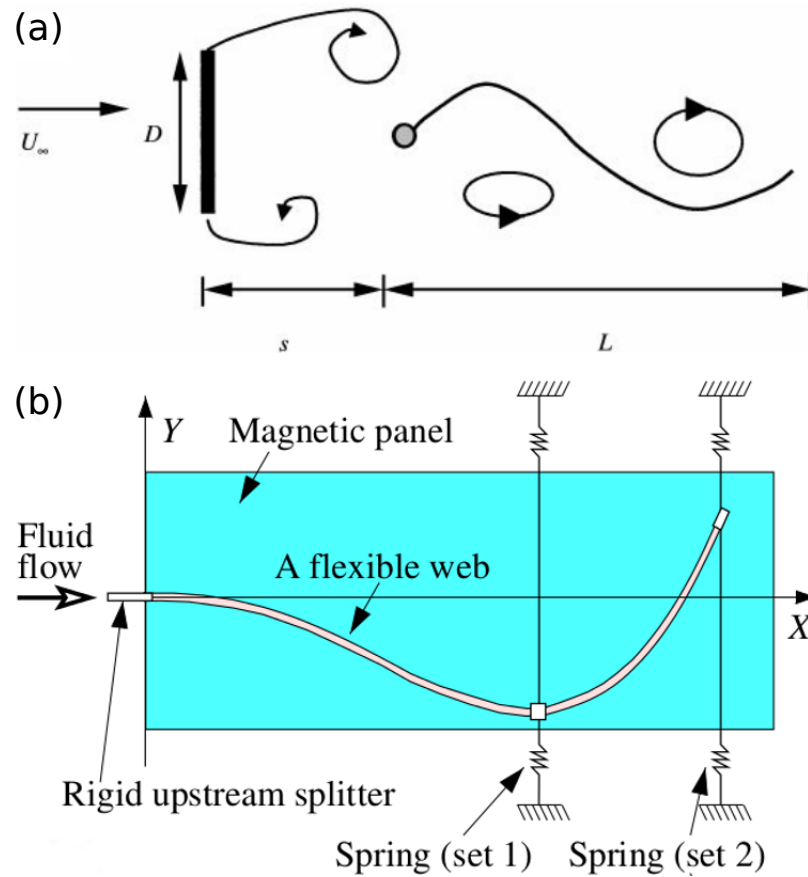


Figure 1.3: (a) The energy harvesting eel from Allen and Smits [2001], (b) a schematic of the flutter mill proposed by Tang et al. [2009b].

been developed to harvest this energy. Flutter has been proposed as a method of harvesting energy from such naturally occurring fluid flows, for example: the “Wingmill” by McKinney and DeLaurier [1981], an energy harvesting “eel” by Allen and Smits [2001] (Figure 1.3a) and Taylor et al. [2001], piezoelectric coupling discussed by Doaré and Michelin [2011], and the “Flutter Mill” by Tang et al. [2009b] (Figure 1.3b). However small to micro scale devices are still relatively impractical due to comparatively high costs and low energy outputs.

1.1.4 Biolocomotion

The locomotion of fish is a further example of an inverse flutter problem. It has been shown in a series of studies by Lighthill [1971] that the swimming mode of fish is similar to that of a cantilevered plate where the ratio of fluid-to-plate mass is 1. Liao et al. [2003a] showed that fish make use of the Kármán gait (Liao et al. [2003b]) allowing the fish to act as a self-correcting hydrofoil, using

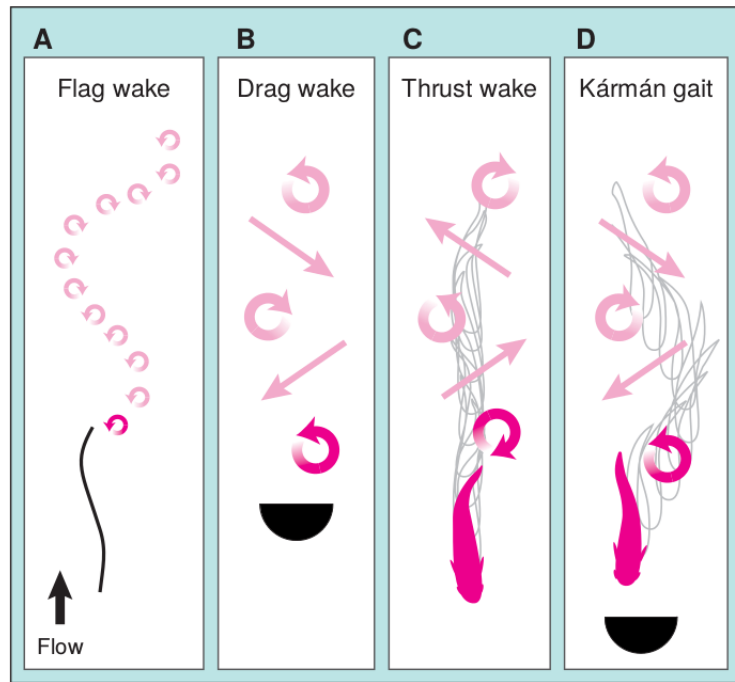


Figure 1.4: A figure from Müller [2003] showing the vortices and jets (arrows) which make up the wake behind a (a) flag, (b) bluff body, and (c) and (d) show the wake behind a swimming fish in moving flow.

the vortices to amplify its own oscillations which has the effect of reducing the energy required for locomotion. More recently Alben [2008] applied the physical properties of a hawkmoth forewing and the pectoral fin of a bluegill sunfish to a theoretical model of a driven flexible cantilever and showed that both cases were optimised for efficiency rather than thrust. Figure 1.4 illustrates the similarities between the motion of a fish and that of a flag. An analogous study by Manela and Howe [2009] examined the effect of vortices shed from an upstream flag-pole on the motion of a flag. It was found that the motion of a flag is dominated by the vortices shed from the rigid upstream support, similar to the motion of the fish behind a bluff body. Further detail about these studies can be found in Section 2.3.2, which discusses large amplitude deflection models found in the literature.

1.2 Research Overview

The work in this thesis focuses on the effect of the wake and flow separation on cantilevered plate flutter in very high Reynolds number flow. The investigation examines the onset of linear instability, and the nature and onset of non-linear

instability when a boundary layer separates from the surface of the plate. Where linear instability is described as situations where amplitudes of oscillation are vanishingly small, meaning non-linear terms in the governing equations can be neglected.

This study involves the development of a model that extends that developed by Howell et al. [2009] to include the effect of a wake, and then the extension of that model to account for non-linear motion and flow separation.

1.2.1 Problem Statements

The research can be summarised as addressing two problem statements:

Problem One: What is the extent to which a wake needs to be included in a model of a cantilevered plate undergoing linear oscillations? Is it possible to include the wake in a boundary-value model based on that in Howell et al. [2009] which is capable of generating a single frequency response using the state-space method despite the highly temporal dependence of the coupled cantilever-wake system.

Problem Two: Is boundary layer separation at large amplitude oscillations the cause of the sub-critical instability found in the experimental data available in the literature?

1.2.2 Methodology

The methods applied to the two problem statements stem from the same equations: a Euler-Bernoulli beam model is used for the plate, the fluid is modelled as potential flow using the Boundary-element method (BEM) with the Discrete Vortex Method used for the wake. The differences arise in the application and combination of these three models:

Problem One: The fully linearised beam, fluid, and wake models are coupled and solved using a time-marching iterative scheme developed by Lucey and Carpenter [1992]. A new model is then developed which makes use of interpretations of the Kelvin Condition to determine the strength of a simplified wake such that it can be included in a boundary-value model. The results generated by this new model will then be compared with the full, initial-value model results. Con-

clusions will be drawn revealing the extent to which the wake must be modelled and whether the new models developed are suitable.

Problem Two: Non-linear models of the beam, potential flow, and wake will be developed and combined in a similar way to the linear models, again solved using the semi-implicit method of Lucey and Carpenter. A new model will be developed which will predict the point at which the flow separates and models the separated boundary layer formed as a free-shear layer composed of discrete vortices. When combined with the non-linear models, a new numerical model of a cantilevered plate experiencing flow separation will be produced and will be used to show whether the separation of the boundary-layer could be a route to the non-linear instabilities shown to appear below the critical velocity in experimental results found in the literature.

The methods briefly outlined here will lead to a greater understanding of the underlying physics of the flutter instability in cantilevered plates, particularly with regard to the role of the wake and boundary layer in that instability.

1.2.3 Scope and Assumptions

In each model developed it is assumed that the plate is infinitely wide, clamped at its leading edge, and immersed in a two-dimensional axial potential flow. Owing to the inviscid nature of potential flow the Reynolds Number is considered infinite, which is a suitable assumption in many engineering applications and was shown by Watanabe et al. [2002b] to give a very close approximation of a viscous flow at high Reynolds numbers.

Recent studies (for example Tang and Paidoussis [2007] and Eloy et al. [2012]) have attributed the apparent hysteresis found in experimental work to structural effects present in finite aspect ratio plates, however, the work here continues to explore the two-dimensional modelling with a view to exposing the underlying phenomena involved in the flutter instability.

1.2.4 Objectives and Contributions

This study has two main aims, firstly to develop a boundary-value model which takes account of the wake, and secondly to produce a numerical model capable of

simulating the behaviour of a cantilevered flexible plate experiencing large amplitude oscillation due to an inviscid flow which includes the effects of an unsteady wake and boundary-layer separation. There are a number of objectives which must be met to achieve these aims:

1. Develop an initial-value model of a cantilevered plate within the limit of linear-amplitude oscillations based on that presented in Howell et al. [2009] which includes the effects of a wake which forms at the trailing edge.

2. Modify the model created in objective 1 to suit the state-space method developed by Pitman and Lucey [2009] such that a boundary-value model is created which includes a wake.

3. Develop a non-linear plate model based on the equations developed by Semler et al. [1994] and Moretti [2003], extending the linear fluid-dynamic model to account for non-linear fluid effects.

4. Develop a method for predicting and simulating flow separation and the free shear layer created as a result of large-amplitude oscillations present during non-linear oscillations.

The new models developed in this thesis will result in new methods which can be applied to each of the areas discussed earlier. A comparison between the models created as a result of objectives 1 and 2 will elucidate the importance of the wake and the extent to which it must be considered when modelling the linear FSI system. The combination of the models produced in objectives 3 and 4 will enable close examination of the affect of flow separation and determine whether it has a role in, or is a path to, the sub-critical instability found in the experimental data presented in the literature. In addition the models developed will be fairly simple and easily applied to other geometries or extended to include other phenomena.

1.3 Thesis layout

The work contained within this thesis is split between four parts containing ten chapters. Part one contains the introduction and literature review. Parts two and three hold the body of the thesis and describe the theory and results related to the linear and non-linear models respectively. Finally, part 4 contains the conclusions and suggestions for further work.

Part I – Introduction and Literature Review

Chapter 1 gives an overview of the research area and briefly discusses some of the models found in the literature across a range of systems which are dominated by flutter, along with the main objectives of the work presented in this thesis.

Chapter 2 is a more specific review of the history and current state of the literature examining the phenomenon of flutter categorised by whether the work presented focuses on the linear or non-linear problem.

Part II – Linear Model

Chapter 3 details the theory involved in the development of each of the individual components of the linear model before discussing their assembly into the numerical-simulation and boundary-value models.

Chapter 4 contains a component-by-component validation of the linear models against results found in the literature.

Chapter 5 firstly presents the results generated by the initial-value model exploring the extent to which the wake must be modelled. Secondly those results generated by the boundary-value model are compared to the initial-value results presented. Finally the results of varying the density of either the plate or the fluid are shown.

Chapter 6 is a summary of the conclusions drawn from the results shown in the previous chapter.

Part III – Non-Linear Model

Chapter 7 describes the theory behind each of the individual components of the non-linear model and combines them in to the full non-linear model.

Chapter 8 contains the validation of the non-linear model against results found in the literature and the linear model presented in **Part II**.

Chapter 9 presents the results of the non-linear model and examines the separation criteria required to reproduce the results seen in the literature.

Chapter 10 is a summary of the conclusions drawn from the previous chapter.

Part IV – Conclusions

The final part of this thesis summarises the overall conclusions from both the linear and non-linear parts and proposes future studies using the models developed during this study.

Chapter 2

Literature Review

This chapter presents a review of past studies of flutter of cantilevered plates and the various situations in which this phenomena arises. The review is divided into experimental and theoretical studies of the flutter phenomenon, and the relevant results and conclusions are examined and summarised in mainly chronological order, revealing the history and motivations behind the work presented in this thesis.

2.1 Introduction to Instability

The interaction between fluids and structures is the primary source of instability in many systems. There is a critical velocity at which the forces in the fluid and structural forces in the flexible plate come into balance and steady state oscillations arise. An exploration of the types of instability which manifest themselves beyond this critical velocity was made by Benjamin [1960, 1963] and Landahl [1962] who described three different classes of instability:

- Class A: Negative energy waves such as Tollmien-Schlichting waves destabilised by dissipation in the system,
- Class B: Positive energy waves, for example Travelling-wave flutter, which are stabilised by dissipation,
- Class C: Instabilities unaffected by dissipation, e.g. divergence and Kelvin-Helmholtz instability.

Class A and B disturbances are the result of an ongoing energy exchange between the fluid and the structure, and class C instability occurs in the case of a unidirectional energy transfer into the structure. Carpenter and Garrad [1986] classified a coalescence between class A and B disturbances as a fourth class of instability, and showed that standing-wave disturbances composed of multiple modes could coalesce giving rise to a class C instability. In ideal flow class A instabilities cannot arise due to the absence of viscosity, leaving only flutter and divergence type disturbances. Howell et al. [2009] were the first to elucidate the nature of the instability of cantilevered plates with regards to modal-coalescence and single-mode type flutter. Howell et al. showed that long cantilevered plates lose stability by modal-coalescence flutter in a similar way to flexible panels (which are restrained at each end), while short plates destabilise by single-mode flutter.

Infinitely long surfaces are only able to support modal-coalescence flutter because single-mode flutter is an artifact solely of the finiteness of a plate as the pressure effects, due to the leading and trailing edges, create a phase shift between the fluid pressure and surface velocity to allow the surface to destabilise via irreversible energy transfer. In terms of the present study single-mode flutter is a class B instability, while modal-coalescence flutter is class C.

The problem of flag flutter has been broadly characterised across the literature in terms of the fluid-to-plate mass ratio (\bar{L}) and critical velocity (U_c), for example in Huang [1995], or Connell and Yue [2007]. In this thesis the mass ratio is given by,

$$\bar{L} = \frac{\rho_f L}{\rho h}, \quad (2.1.1)$$

where ρ_f , ρ , L , and h are the fluid and solid density, plate length, and plate thickness respectively, and the critical velocity is the flow velocity at which the plate loses stability. A summary of the physics of the FSI of cantilevers is shown in Figure 2.3.

2.2 Experimental Studies

As stated briefly in the introduction, the study of flutter extends back to the late 19th century. Rayleigh [1879] compared the flapping of a flag to the motion associated with a Kelvin-Helmholtz instability and predicted that the fluttering of the flag was a result of any perturbation to the flag or flow. However, the model lacked a description of the flag's inertial and mechanical forces. The study of Thoma [1939] corrected this omission and showed that flag flutter had a dependence on the mass of the flag, and that the flow over a deformed surface produces elevated and reduced pressures in the troughs and crests respectively and that this tended to increase amplitudes developing a travelling wave. Stearman [1959] made an experimental and theoretical study of the problem of a flexible membrane pinned at its trailing edge and found that as the critical velocity was approached a flag would undergo small-amplitude deflections before losing stability at the critical velocity and entering large unstable oscillations of increasing amplitude. Though these experiments are for a different problem, the conclusions are relevant to the linear plate deflection studies discussed in Section 2.3.1.

The first major experimental study was performed by Taneda [1968], who studied flags made of various fabrics. Taneda showed that at low flow speeds when flags do not flutter a thin von Kármán wake forms downstream of the flag. Increasing the flow speed resulted in steady, periodic oscillations accompanied by a large trailing vortex wake, and further increasing the flow speed resulted in aperiodic oscillations. Taneda commented that during flutter the Kutta condition seemed not to be satisfied by the complex flow at the trailing edge of the flag. It was also noted that during large oscillations the wake separates from the surface of the flag. The Kutta condition states that *a body with a sharp trailing edge which is moving through a fluid will create about itself a circulation of sufficient strength to hold the rear stagnation point at the trailing edge* (Kuethe and Schetzer [1959]). This holds true for small deformations of the flag. However at larger amplitudes the unsteadiness of the flow and flow separation serve to violate the Kutta condition (Katz and Plotkin [2010]) as in the observations made by Taneda. Similar experiments on the stability of hanging strips were performed by Datta and Gottenberg [1975], who measured the critical velocities of plates

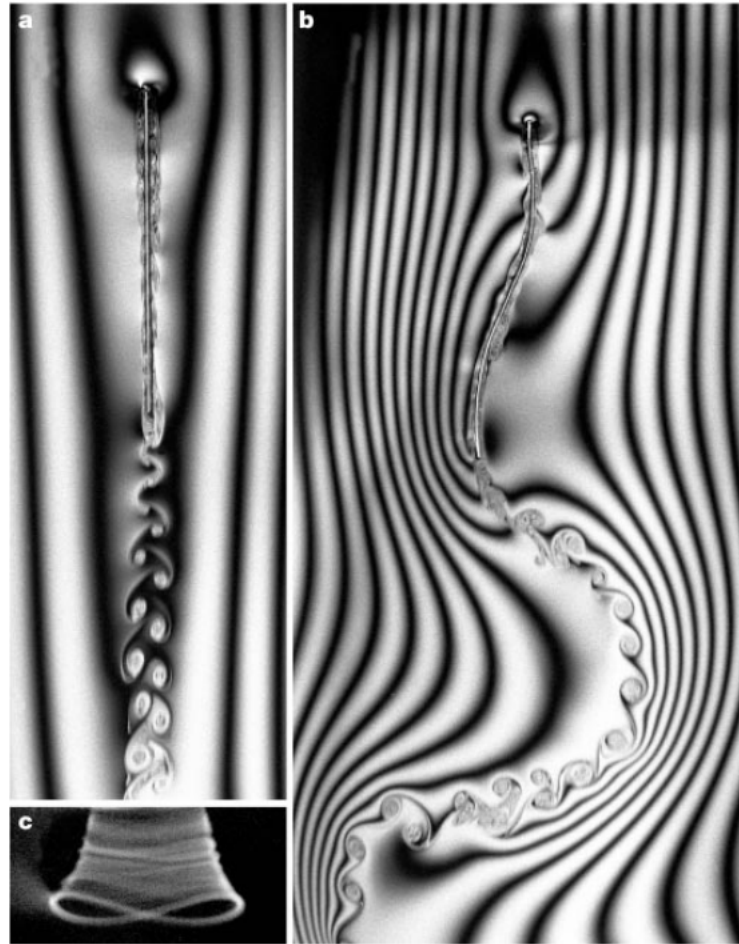


Figure 2.1: The experiments of Zhang et al. [2000] showing the flexible filament deflection and associated wake in low speed flow (a). The deflection, wake, and tip displacement in a high speed flow are shown in (b) and (c) respectively.

with different aspect ratios and thicknesses. In agreement with the experiments of Stearman [1959] it was observed that as the critical velocity was approached the plates would undergo small-amplitude oscillations before losing stability and entering into large-amplitude oscillations.

A more recent example of experimental work is the study of Zhang et al. [2000], who used a flowing soap film to experimentally examine the phenomenon of flutter by investigating the oscillations and wakes of single (Figure 2.1) and double filament configurations. The double filament configuration is analogous to flow within and outside of a flexible two dimensional channel, whereas the single filament configuration is an experimental representation of the one dimensional plate in a two dimensional flow which the present study examines. Contrary to Rayleigh's predictions, the fluttering observed by Zhang et al. was not caused by perturbations in the flow owing to an upstream support, but rather by the

interaction between the mechanical properties of the flexible filament and the fluid flow. During steady state oscillations the fluid and filament mass were in balance, and the strain energy in the filament balanced the kinetic energy in the fluid. It was also noted that no instability would occur if the filament was initially flat, and hysteresis was found using the length as a control parameter. Hysteresis was also found in the experiments of Watanabe et al. [2002a] who used flow speed as the control parameter in their studies of paper flutter, a limiting factor in the speed of paper production and printing processes. Shelley et al. [2005] observed hysteresis and bi-stability in their experiments using an articulated flag in water designed to be able to flutter in one dimension while avoiding sagging under its own weight. It was found that above the critical flow velocity, a sheet in axial flow began to flap with a Strouhal number within the characteristic range of animal locomotion. This study emphasised the role of plate inertia in overcoming the stabilising effects of rigidity and fluid drag. Lemaitre et al. [2005] examined ribbons made of different materials hanging in axial air flow and found that the critical velocity depended strongly on the length of short ribbons and weakly for long ribbons.

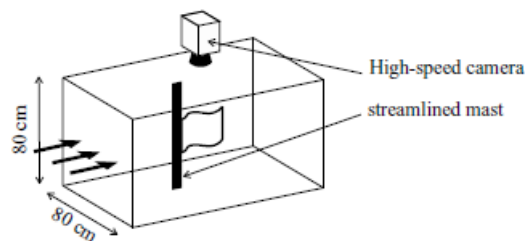


Figure 2.2: Adapted from Eloy et al. [2008], showing the experimental setup.

Eloy et al. [2008] studied the effect of aspect ratio where width is defined span-wise to the flow, as shown in Figure 2.2) on flutter instability and found that hysteresis was absent for aspect ratios ≤ 1 , and for larger aspect ratios (≥ 1) that the observed hysteresis would greatly increase. It was also seen that for large aspect ratio plates, the top corner of the plate would exhibit sub-critical flutter while the rest of the plate remained motionless, and that the amplitudes reached by this corner of the plate were greater than the rest of the trailing edge. Eloy et al. [2008] propose that this phenomena is a result of a non-uniform pressure

field developing over the plate and gravitational effects causing compression at the top corner, leading to a reduction in tension at that point, and as tension has a stabilising effect this reduction causes a loss of stability sooner than at other points on the plate.

The effect of in-plane tension on the stability of a cantilevered sheet in flow was examined by Morris-Thomas and Steen [2009]. It was shown that an increase in tension resulted in a reduced drag coefficient and increased stability, leading to higher critical velocities. The low flexural rigidity associated with flexible sheets complicates experimental studies. To circumvent this, most studies are of a vertically mounted sheet (such as in the studies of Taneda, Datta and Gottenberg, and Lemaitre et al.) where a gravity-induced tension dominates the fluid-induced tension. Studies of horizontally mounted sheets (e.g. Watanabe et al. [2002a]) require pre-tensioning, or articulation in the case of Shelley et al. [2005], to ensure the sheet is flat until the critical velocity is reached. Morris-Thomas and Steen also reported that the drag coefficient would decrease with increasing Reynolds number as a result of the increasingly irregular oscillations present at those higher Reynolds numbers, and that heavier sheets had a much lower critical velocity than lighter sheets. The work of Zhao et al. [2012] confirmed the observations of Eloy et al. [2008] and Lemaitre et al. [2005], that hysteresis was present for large aspect ratio plates and absent for small aspect ratio plates, and that the critical velocity depended strongly on the length of short plates, and was almost independent of the length of long plates. Where a short plate is one with a mass ratio $\bar{L} < 1$, and a long plate where $\bar{L} > 1$. Zhao et al. also found that a stable plate subjected to an external disturbance would flutter at the same amplitude as that reached through self-excitation at the same flow velocity.

2.3 Theoretical Studies

Alongside the foregoing experiments, theoretical studies have primarily been split into two areas of interest: those seeking to explore the onset of flutter have generally confined themselves to the limit of linear deflections, while those exploring bi-stability, chaos, and post-critical flutter have modelled large-amplitude deflec-

tions. To mirror this split, the remainder of this literature review will be separated in to those works which study geometrically linear models, and those which study geometrically non-linear models.

2.3.1 Linear Plate Deflection

Linear studies assume that the deflection of the plate is vanishingly small, such that non-linear effects can be neglected and a point on the surface of the plate can be assumed to move only perpendicular to the plate. The result of this assumption is that the motion of the plate is restrained in the horizontal (x) direction, and free in the vertical (y) direction. An analytical study of the problem was first made by Kornecki et al. [1976] who employed a two-dimensional potential flow model coupled with an infinitely wide plate and determined that the type of instability depended on the plate end conditions. This showed that a plate fixed at its leading and trailing edges lost stability by divergence (a static instability where the plate undergoes an amplifying deflection from the initial position), while cantilevered plates lose stability by flutter. Through comparison with experimental results it was shown that a cantilevered plate of infinite width exposed to flow on both surfaces behaves as a thin flexible aerofoil, and that circulation and wake vortices have a significant effect on the loss of stability. Shayo [1980] extended the work of Korneki et al. for finite large aspect ratio cantilevered panels and confirmed the importance of the effect of the wake with regards to the loss of stability, particularly for large fluid-to-plate mass ratios (\bar{L}), reporting that a two-dimensional analysis which excludes wake effects overestimated the critical flow velocity.

Huang [1995] used a similar model to Shayo in his study of human snoring, but included viscous effects through a Kutta condition at the trailing edge, and compared generated theoretical results with his own experimental results. Good agreement was found between the experimental and theoretical critical flow speeds, and necking, a narrowing of the deflection envelope, was observed in the deflection envelope in experiment close to the theoretically predicted position of the neck. The presence of the neck confirmed that the vibration was a combination of the first two *in vacuo* modes, agreeing with theoretical predictions. Also

observed was the growth of small-amplitude oscillations as the critical velocity was approached, in agreement with the experimental observations of Datta and Gottenberg [1975]. It was discovered that the wake had a significant effect on the amplitude and frequency of plate oscillation and that the system is controlled by the flow speed and mass ratio. Though experimental studies show that the Kutta condition does not apply to the cantilever flutter FSI problem, the Kutta condition is relevant at small amplitudes, shown by the theoretical studies in this regime. However, at large amplitudes, or in cases where there is a complicated trailing edge flow system the Kutta condition will not apply. This is discussed in Section 7.2.1.

Guo and Païdoussis [2000] extended the work of Huang on the effect of the mass ratio, examined the effects of different boundary conditions on stability, and found that cantilevered plates lose stability by single-mode flutter of the second mode. Increases in critical velocity with increasing mass ratio were due to the rising number of modes involved with the associated instability. Watanabe et al. [2002b] demonstrated that a simple eigenmode analysis using potential flow theory produced results which compared very well to those generated by a more complex simulation composed of a Navier-Stokes equation solver coupled with a beam deflection solver. Watanabe et al. also presented a comparison between a collection of experimental and theoretical results (Figure 2.3), showing that a consistent trend in the relationship between critical velocity and mass ratio was being captured over a large range of parameters in a number of studies. Also highlighted by this comparison was the fact that theory consistently under-predicted the critical velocity.

Zhu and Peskin [2002] modelled a filament in viscous flow, mirroring the experiments of Zhang et al. [2000], using an immersed boundary method and observed the same bi-stability of long filaments as in experiments, where bi-stability is a phenomena where the system can exist in two different stable states under the same conditions. The numerical results of Zhu and Peskin also highlighted the importance of plate mass without which the plate was seen to remain undisturbed, and increasingly large-amplitude oscillations were observed for filaments of increasing mass. Importantly it was found that even at a much lower Reynolds

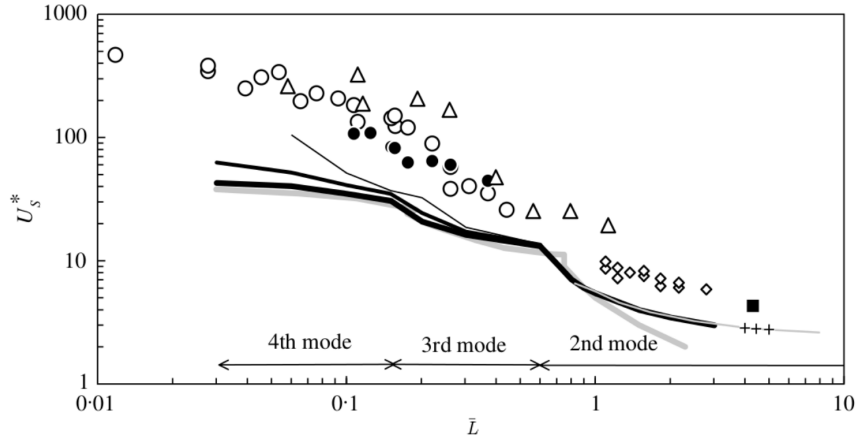


Figure 2.3: The graph presented in Watanabe et al. [2002b] demonstrating the trend and discrepancy between a collection of theoretical (continuous data) and experimental (discrete data) results for critical velocity plotted against mass ratio (\bar{L}) in the literature.

number (≈ 200) than was used in the experiments of Zhang et al. (≈ 20000) very similar results both quantitatively and qualitatively were obtained, leading Zhu and Peskin to conclude that the Reynolds number was not a controlling parameter and suggest that non-dimensional plate mass is an important parameter. Balint and Lucey [2005] also included fluid viscosity in their simulations to explore the flow around the soft palate in the human upper airway, combining a two-dimensional Navier-Stokes solver with a linear beam model, and produced results similar to those of Huang [1995]. Balint and Lucey demonstrated that instability occurred beyond a critical Reynolds number where the fluid-to-plate energy transfer rate was greater than that of the plate energy dissipation rate. This study also highlighted the importance of the mass ratio and its effects on plate stability. Lemaitre et al. [2005] developed a numerical model based on the Galerkin method that used an unsteady potential flow and found a consistent under-prediction of critical velocity by their theoretical model as compared to their experimental results. Lemaitre et al. also found that as the length of the plate was increased an increasing number of modes were required to accurately predict the plate motion, agreeing with the observations of Guo and Païdoussis [2000].

Argentina and Mahadevan [2008] presented a model for a two-dimensional flag of large aspect ratio in a two-dimensional fluid, selecting parameters such that the effect of the downstream wake would be minimised. A comparison of

their results with and without flow-induced tension and three-dimensional flow effects, specifically the influence of plate aspect ratio, showed that their results were much closer to experimental data when these effects were included. When these effects were excluded the predicted critical velocity was consistently lower than found in experiments, in agreement with other theoretical results found in the literature. Including three-dimensional effects was shown to modify the added mass parameter and pressure by a factor less than unity, and including the Blasius boundary layer stabilised the flag as the tension induced by the fluid flow serves to stretch the flag, hence increasing the predicted critical velocity. Eloy et al. [2007] examined the effects of a three-dimensional inviscid flow on a plate experiencing two-dimensional flutter motion using a Galerkin method coupled with Fourier transform methods. This study determined that the inclusion of the plate aspect ratio increased the accuracy of their predicted theoretical critical velocity, and that a plate of finite aspect ratio is more stable than a plate whose aspect ratio is infinite. This is the result of lower overall fluid force generated across a small aspect ratio plate.

Howell et al. [2009] used a two-dimensional potential flow model and a one-dimensional plate model applied to the human upper airway, and analysed the stability of the coupled system using two methods. Firstly using a numerical analysis which included the effects of a linearised wake similar to that presented in Argentina and Mahadevan [2008], and secondly excluding the wake and directly extracting the eigenvalues. These differing approaches allowed Howell et al. to examine transients and the effect of spatial variations in stiffness along the plate, and also make predictions of the infinite-time behaviour of the plate. It was found, in agreement with Guo and Païdoussis [2000], that the instability of short plates is dominated by single-mode flutter, and that modal-coalescence flutter causes the destabilisation of long plates. A study of the plate energetics revealed that for short and long plates the principal regions of irreversible energy transfer from the fluid to the plate were in the middle and trailing edge portions of the plate respectively. Howell et al. [2009] also showed that the effect on a system owing to a linear wake was dependent upon the mass ratio. The wake was found to have a slightly destabilising effect on plates of high mass ratio, and a greater

stabilising effect on low mass ratio plates. The numerical methods presented allowed the plate to arrive at a steady-state oscillation developed in time, while Galerkin methods compose the final steady-state oscillation from a pre-selected set of *in-vacuo* cantilevered plate modes. Additionally a time-stepping model enables the examination of transients in the system, which are excluded from Galerkin methods owing to the nature of their construction.

A further paper (Howell et al. [2011]) examined the effect of inertial inhomogeneity on plate flutter in the absence of a wake and showed that adding a discrete mass to short (low mass ratio) plates could promote destabilisation into single-mode or modal-coalescence flutter at lower or higher critical velocities respectively, depending on the position of the mass. Adding the same mass to long (high mass ratio) plates was found to only destabilise the system as it served to either promote modal-coalescence flutter or replace it with single-mode flutter at a lower critical velocity. Huang and Zhang [2013] examined the eigenvalue solution for plates of mass ratio of around unity and attempted to explain whether the wake effect should be included. It was shown that the Kutta condition is responsible for the coupling between the lift induced by the second mode and the vibration velocity caused by the first mode. In agreement with other studies it was also shown that higher-order *in vacuo* modes are involved with the flutter instability at higher mass ratios. The effect of adding a concentrated mass to the middle and trailing edge of the plate, similar to that in Howell et al. [2011], was shown to have very stabilising and destabilising effects respectively, suggesting a method of delaying or promoting the onset of flutter.

2.3.2 Non-Linear Plate Deflection

Non-linear studies examine limit-cycle or chaotic oscillations of a cantilevered plate undergoing large-amplitude deflections at flow speeds above the critical velocity. Semler et al. [1994] derived a set of equations for modelling the non-linear motion of inextensible cantilevered pipes conveying fluids and compared them with other equations already found in the literature. The fundamental differences between cantilevered pipes and pipes with both ends fixed were also shown. Non-linearities in an inextensible cantilevered pipe were mainly due to

the large curvature experienced during motion, while in pipes fixed at both ends the non-linearities were associated with the pipe stretching. Yadykin et al. [2001] developed a numerical model solved using the Galerkin method. The structural model used was similar to that developed by Semler et al. except for the inclusion of drag terms and the lack of internal fluid mass. It was found that eight modes were required to accurately represent the instability and that the nature of the instability changed with increasing flow speed; changing from regular standing-wave type to irregular travelling-wave type oscillations and jumping in amplitude and frequency.

Tang and Dowell [2002] derived the non-linear equations of motion for a cantilevered plate using Hamilton's principle. In combination with a three-dimensional linear vortex lattice method, they used these to calculate the linear flutter boundary and limit cycle oscillations of a flexible plate fixed to the trailing edge of a rigid aerofoil. The wake was modelled as a horseshoe vortex and acted as a continuation of the panel surface. It was found that for the linear stability analysis the flutter mode was dominated by the second *in vacuo* mode which is in agreement with previous work. Beyond the critical velocity, limit-cycle oscillations were found, increasing in size with flow velocity but with decreasing frequency. A following paper by Tang et al. [2003] focused on validating the model presented in Tang and Dowell [2002] against experimental results. Good agreement was found between the theoretical and experimental results for the linear flutter boundary. However, as the flow speed increased beyond this point, a large jump in oscillation amplitude was observed in the experiments which was not reflected in the theoretical predictions. Hysteresis, observed in their experiments, was also absent from the theoretical results. These are attributed to the linear aerodynamic model employed, which does not account for such large structural motions. It was shown that the range of flow velocities for which non-linear aerodynamic effects can be ignored is very small, and concluded that these effects must be included in future models seeking to model the limit-cycle oscillations of cantilevered plates. Attar et al. [2003] extended the work of Tang and Dowell to include a non-linear aerodynamic model. It was found that the system would lose stability sooner than predicted by the same coupled system using the linear

aerodynamic model, and that despite the inclusion of a non-linear fluid model the theoretical model developed was unable to reproduce the hysteresis observed in the experiments of Tang and Dowell.

Moretti [2003] performed an analytical study of a perfectly flexible yet inextensible one-dimensional plate in two-dimensional ideal flow. Moretti considered the source and influence of the induced tension in the body, showing that during flapping this tension becomes very significant. In a subsequent paper, Moretti [2004], concluded that the tension induced in the flag by the boundary layer opposes the flutter induced by the flow field and that this tension limits the flutter amplitude, an observation shared by Zhang et al. [2000] and Argentina and Mahadevan [2008]. Linear models do not include tension in their governing equation for plate deflection and hence over-predict flutter amplitudes.

Tang and Païdoussis [2007] investigated the non-linear dynamics and limit-cycle oscillations of a cantilevered plate in axial flow. Coupling a non-linear equation of plate motion based on the inextensibility condition of Semler et al. [1994] and an unsteady lumped vortex model related to that described in Katz and Plotkin [2010], solved using the Galerkin method. In this model the wake was shed from the trailing edge and the wake vortices were unaffected by neither the bound vorticity nor the other wake vortices. The model of Tang and Païdoussis was similar to that of Tang and Dowell [2002], but improved most notably by including the effects of tension and longitudinal plate displacements associated with large-amplitude oscillations. It was shown that the critical velocity was very sensitive to plate length for short plates, and comparatively invariant when the plate is sufficiently long, in agreement with the experimental observations of Lemaitre et al. [2005]. Consistent results are seen between those results generated by Tang and Païdoussis and experimental data presented in the literature for the critical velocity. Hysteresis was not found in their initial theoretical model, but was found when a non-physical von Kármán wake street was added to the undulating wake to explore the phenomenology. The results presented in Tang and Païdoussis [2007] suggest that the velocity at which the plate returns to a neutral state is higher than that at which it loses stability, this is referred to as a supercritical bifurcation, while in experiments this bifurcation normally appears

sub-critically. Tang and Païdoussis suggest that the hysteresis in experiment could be a result of spanwise bending acting to stiffen the plate delaying the onset of instability, which is then ironed-out once flutter has taken hold. A follow-up paper elucidated the effect of the wake on the stability of cantilevered flexible plates (Tang and Païdoussis [2008]) and showed that the wake has very little effect on the stability of long plates. Through a comparison with plates of differing mass ratio, it was shown that as the mass ratio increases the wake-induced flow velocity decreases significantly, having approximately 16% the strength at $\bar{L} = 20$ than was present at $\bar{L} = 0.2$ owing to the increased flutter frequency at higher mass ratios. This increase in flutter frequency results in shorter wavelengths in the wake, meaning that successive wake vortices of alternating signs are closer to each other and tend to cancel each other out, leading to the wake having an overall smaller influence on the plate. This explained how theoretical results in the literature, which included or excluded the wake, gave comparable results for sufficiently long plates.

The models presented in Tang and Païdoussis [2007], Tang and Païdoussis [2008], and a further paper (Tang et al. [2009a]) which examined the effect of several variations on the classical system, culminated in a novel concept for generating electrical power, the “flutter mill”, proposed by Tang et al. [2009b]. The “flutter mill” uses the flapping of flexible conductive elements as a source of driven motion through a magnetic field to generate electricity. The proposed design was optimised based on the results of adding supporting springs and concentrated masses presented in Tang et al. [2009a]. The energy characteristics were compared to a stall-regulated wind turbine and found to have a comparable power output, given the assumption of the authors that the flutter mill would be able to convert 10% of the energy extracted into electrical power.

Connell and Yue [2007] provide the most complete study to date of a flag in viscous flow using a simulation coupling a finite-element model to a solver for thin membrane dynamics of arbitrarily large motion. They identified three distinct regimes of instability with increasing mass ratio: (I) fixed-point stability, in which the flag settles into a stable non-oscillatory straight form; (II) limit-cycle flapping, where the body enters steady oscillations of constant amplitude

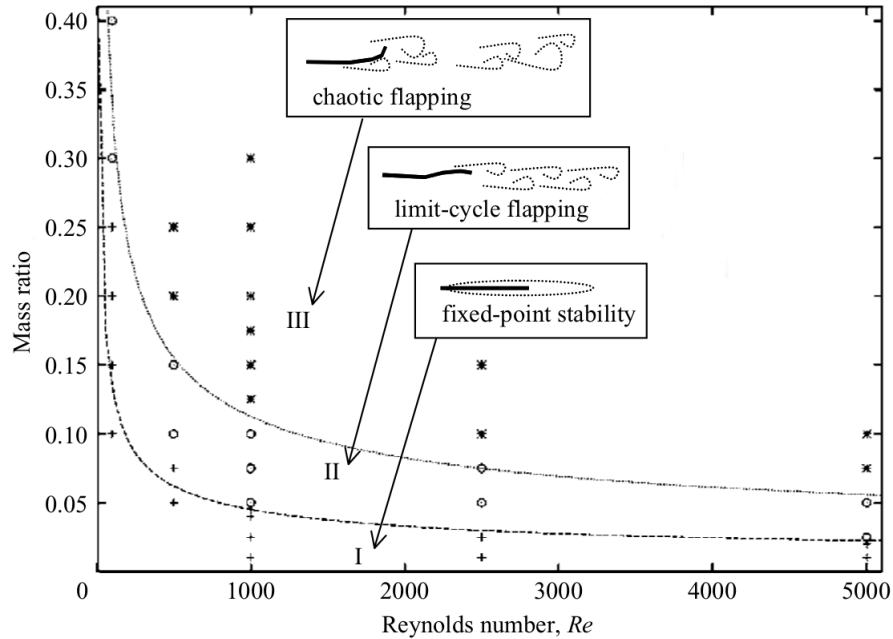


Figure 2.4: The transition between the three instability regimes for a flag of constant rigidity and the general form of the wake associated with each regime. From Connell and Yue [2007].

and frequency; and (III) chaotic flapping, where the flag undergoes irregular non-periodic flutter. Figure 2.4 demonstrates the transition between each of the three instability regimes as a function of the mass ratio and Reynolds number. As the mass ratio is increased, the flutter instability becomes increasingly irregular as does the associated wake. Connell and Yue also show that hysteresis can be approximated by the Duffing equation and that the flag is analogous to a softening non-linear spring. Owing to the complexity of their model, it is very difficult to explore the underlying physics with regards to the specific interactions involved and their individual roles in the FSI system.

A study by Alben and Shelley [2008] explored the effect of rigidity for a given mass ratio on a two-dimensional plate in inviscid flow with a free vortex sheet. It was shown that a very slight reduction in flag rigidity would change the instability from steady limit-cycle oscillations into chaotic flapping, with the associated wake similarly changing from a steady von Kármán type vortex street to an irregular wake structure, in agreement with Connell and Yue [2007]. Alben and Shelley observed that the flag would experience less drag when in chaotic motion than in the steady-state oscillation regime, an observation shared in the experimental work of Morris-Thomas and Steen [2009]. Good agreement is found between

the model of Alben and Shelley and the results of the experiment by Shelley et al. [2005] at low mass ratios for the limit of linear stability. Their model was to the author's knowledge the first of its type to be able to demonstrate sub-critical bi-stability, though only a very small hysteresis loop was found, suggesting that the larger hysteresis found experimentally may be due to fluid viscosity and structural damping effects. A following paper by Alben (Alben [2009a]) elucidated the numerical method employed in Alben and Shelley [2008] and explored the dynamics of a periodically driven flexible plate with reference to biocomotion problems. It was shown that non-linear behaviour arises gradually as a result of wake roll-up occurring downstream of the trailing edge.

Extending the linear work presented in their previous paper in 2007 and accompanying their experimental results discussed earlier, Eloy et al. [2008] explore the effect of aspect ratio in a theoretical model of three-dimensional potential flow interacting with a finite plate. It was found that the critical velocity would decrease with increasing aspect ratio, and that the measured critical velocities were closely matched by linear stability analysis. However, for large aspect ratios, linear analysis tended to underpredict the critical velocity. They were also able to confirm the results of Kornecki et al. [1976], and found that instability was lost in increasingly higher order modes with increasing mass ratio; for $\bar{L} \leq 1.5$ the cantilever would lose stability into the second mode, for $1.5 \leq \bar{L} \leq 5$ stability was lost into the third mode, and further modes when $\bar{L} \geq 5$. Agreement was also found with their experimental results; hysteresis was largely absent from low aspect ratio plates, and very clearly present in the case of large aspect ratio plates. It was shown that for large aspect ratio plates that the flutter mode was not one-dimensional as parts of the plate were seen to flutter sooner or at larger amplitudes than others. Eloy et al. suggested that the hysteresis was supercritical and caused by two-dimensional span-wise plate deflections relating to material imperfections. They also suggested that the two-dimensional plate deflections could originate from upstream vortex shedding.

Michelin et al. [2008] developed a model of the wake using unsteady point vortices shed from the trailing edge of a two-dimensional flag in a steady two-dimensional potential flow. They observed the same three instability regimes

identified by Connell and Yue and very good agreement was found between their linear stability analysis and that presented by Kornecki et al. [1976]. They were also able to observe hysteresis in their model, though far smaller than that presented in Eloy et al. [2008].

Manela and Howe [2009] studied the influence of vortices shed from an upstream support on the onset of instability in a flag by separating the deflection into vortex-induced and self-induced components. Manela and Howe found that these upstream vortices cause instability at much lower flow speeds than predicted by the linear theory, concluding that models which exclude these vortices are incomplete and that it is necessary to consider the upstream support in the accurate modelling of real flags. The vortices shed from an upstream bluff body were a key component in the energy generation device proposed by Allen and Smits [2001], and in the research into fish locomotion by Müller [2003], both of which discuss how these free vortices promote a forced motion of a flexible body. However, for the purposes of comparison with experimental results, it is noted that frequencies predicted from the linear theory presented in the literature which exclude these upstream vortices match very closely the experimentally determined frequencies. Additionally, the majority of the experimental results presented are obtained under carefully controlled conditions and place the flexible plate behind a thin aerofoil to minimise or remove the vortices that would be shed from a bluff body (see for example the experiments of; Eloy et al. [2008], Tang and Dowell [2002]). Furthermore, in the flow visualisations available (e.g. Zhang et al. [2000], Taneda [1968]) no obvious flag pole related vortices can be seen. This leads to the conclusion that for the purposes of exploring the underlying physics of the problem it is not necessary to account for the vortices shed from an upstream support. It is possible, however, that these shed vortices are responsible for the sub-critical small-amplitude oscillations observed experimentally before the onset of large-amplitude flutter.

Zhao et al. [2012] present a comparison between the model presented in Tang and Paidoussis [2007] and their own experimental results, which showed excellent agreement for the limit of linear stability. However, the theoretical model predicted a supercritical bifurcation while their experiment demonstrated a sub-

critical bifurcation. Zhao et al. reiterate the explanation posed by Tang and Païdoussis [2007] and Eloy et al. [2008] with regards to the origin of hysteresis in experiment: that large aspect ratio plates suffer more from spanwise deformations which have a psuedo-stiffening effect leading to higher critical velocities. However, once the plate is unstable these spanwise deformations are removed as the flutter mode is essentially one-dimensional thereby generating a hysteresis loop when the flow speed is decreased. A study of human snoring was made by Elliot et al. [2010] who included the effects of viscosity and finite plate thickness. Though the focus of the paper is on demonstrating a model which is able to more faithfully reproduce the physiology of the upper airway by taking into account the finite thickness of the soft palate, Elliot et al. also provide examples of finite amplitude *in vacuo* oscillations of a cantilevered plate which will be useful for the purpose of validation in this thesis.

Eloy et al. [2012] sought to explain, through a weakly non-linear stability analysis and experiment, the origin of the large sub-critical hysteresis observed in experiments and the comparatively small, mainly supercritical hysteresis present in numerical experiments presented in the literature (reference is made to a few papers where a sub-critical hysteresis loop is found for large mass ratio plates, for example Alben and Shelley [2008]). Very good agreement was found between the predicted and experimental flutter amplitudes for both slender-body and two-dimensional limits at a various aspect ratios. The experiment and the two-dimensional models showed sub-critical bifurcation, while the slender-body model showed supercritical bifurcation. An experimental comparison between flat and pre-curved plates showed that pre-curved plates would lose stability later than flat plates as a result of the increased stiffness associated with the curvature. This supports the explanation of the hysteresis loop proposed by Tang and Païdoussis [2007] and the experimental observations regarding in-plane tension by Morris-Thomas and Steen [2009]. They suggested that this is also responsible for the poor repeatability observed in experiments of flows of increasing velocity, but note that the threshold predictions of linear stability models are in excellent agreement with the experimental results of threshold in a decreasing velocity flow. Though elegant, this does not explain the presence of hysteresis in the experiments of

Zhang et al. [2000], but it does preclude other proposed explanations such as blockage effects and energy dissipation through structural damping.

2.4 Motivation

There are a number of motivating factors for undertaking this study leading from the review of current literature:

1. Generation of simpler models: a model will be developed which will combine a linear wake model with the geometrically linear coupled plate-fluid model presented in Howell et al. [2009] and arranged to form a state-space solution. This will allow for a quick and efficient analysis of the system stability at the infinite time limit without the need to pre-define or limit the number of modes involved in the solution as is necessary to the Galerkin method. Additionally, and as a point of difference from other work found in the literature (for example that presented in Tang and Dowell [2002]), it will allow the exploration of the effect and necessity of the wake and the extent to which it must be considered when modelling the system.
2. The work presented in the literature does not explore from first-principles the effects of boundary-layer separation observed in the flow visualisations available (for example those presented in Taneda [1968] and Watanabe et al. [2002a]). Another possible source of the two-dimensional plate deflections discussed by Eloy et al. [2012] as a cause for the hysteresis observed in experiments could be the wake associated with the flutter instability. The most notable difference between those models able to show hysteresis, however small, and those unable to, seems to lie with whether the model allows the roll-up of the wake. Alben and Shelley [2008], Michelin et al. [2008], and Zhu and Peskin [2002] all permit wake roll-up, and all show hysteresis, while Tang and Païdoussis [2007], and Tang and Dowell [2002] do not. In fact Tang and Païdoussis are able to simulate some hysteresis when they impose a pre-defined von Kármán roll-up street on their simplified wake model, suggesting that the ability of the wake to roll-up may be a contributing factor in the appearance of sub-critical hysteresis in the stability

of a flexible cantilevered plate in axial flow. Thus, it is a motivation of this study to develop a model capable of simulating the effects of boundary-layer separation to examine this as a possible candidate for the cause of the hysteresis loop discussed in the literature.

3. To generate models capable of furthering the understanding of flutter and elucidating the underlying physical phenomena which surround the instability.

The outcomes of this research will have applications to each of the areas discussed in the introduction and will contribute to the growing body of work that addresses the questions posed by flutter.

Part II

Linear Model

Chapter 3

Theory

This chapter concerns the theory and assembly of linear boundary-value and numerical simulation models. The final models are capable of demonstrating the effect of a wake on a cantilever in uniform inviscid flow and exploring the underlying physics of the phenomena of the system shown in Figure 3.1. Owing to the small-amplitude deflection, simplifications and assumptions can be made and these are discussed in the following sections.

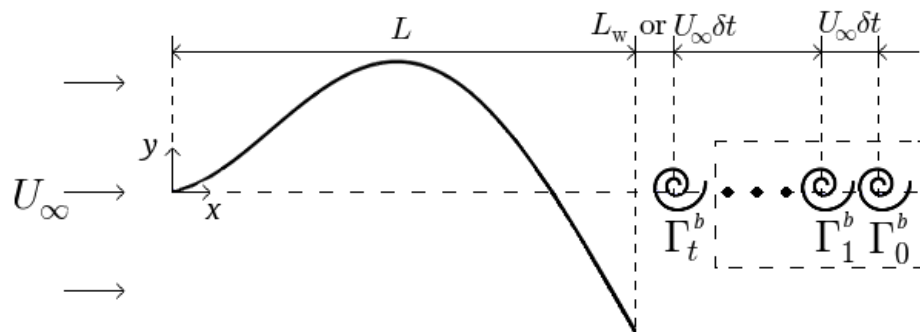


Figure 3.1: The linear system modelled. Those vortices in the dashed box apply only to the full numerical simulation.

3.1 Plate Model

The cantilever is discretized into N mass points each separated by a distance, δs , of L/N where L is the length of the cantilever, and M individual panels. Figure 3.2 shows this discretization, noting that at very small deflections $\delta s = \delta x$. The mechanical properties of the plate are lumped at each mass point.

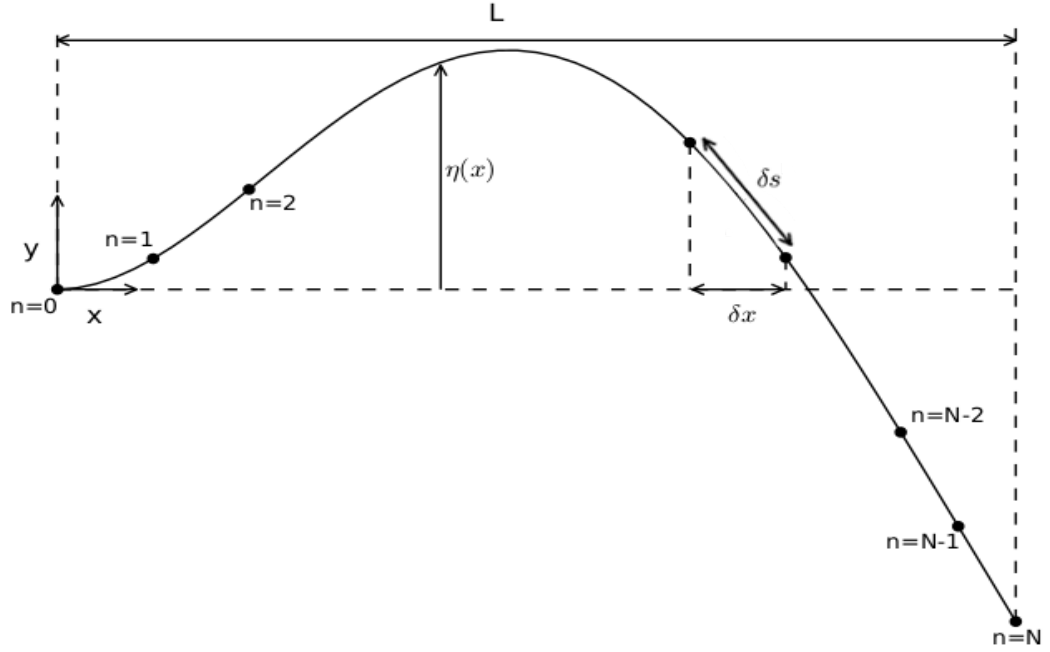


Figure 3.2: Beam discretization

The plate is modelled using a linearised Euler-Bernoulli beam equation,

$$\rho h[\mathbf{I}]\ddot{\eta} + d[\mathbf{I}]\dot{\eta} + B\mathbf{D}_4\eta = -\delta p, \quad (3.1.1)$$

where ρ , h , d and B are the plate density, thickness, damping and flexural rigidity respectively. η is the vertical displacement of mass points along the beam and δp is the fluid loading. \mathbf{D}_4 is the fourth spatial derivative of η which takes the form,

$$\mathbf{D}_4\eta_n = \frac{1}{\delta x^4} (\eta_{n-2} - 4\eta_{n-1} + 6\eta_n - 4\eta_{n+1} + \eta_{n+2}). \quad (3.1.2)$$

The plate is assumed to be infinitely wide, leading to a correction in the flexural rigidity as the flexible surface experiences no plane strain,

$$B = \frac{Eh^3}{12(1-\nu^2)}, \quad (3.1.3)$$

where E and ν are the Young's modulus and Poisson's ratio respectively. The plate is also assumed to be very thin, and hence deforms by bending only, experiencing neither its own weight nor shear.

3.1.1 Boundary Conditions

The system being examined is the clamped-free case, yielding the following boundary conditions,

$$\eta_{n=0} = 0, \quad (3.1.4)$$

$$\frac{\partial \eta_{n=0}}{\partial x} = 0, \quad (3.1.5)$$

$$\frac{\partial^2 \eta_{n=N}}{\partial x^2} = 0, \quad (3.1.6)$$

$$\frac{\partial^3 \eta_{n=N}}{\partial x^3} = 0. \quad (3.1.7)$$

These enforce zero deflection and slope at the clamped end where $n = 0$ and zero bending moment and shear force at the free end where $n = N$. Numerically, these are applied in the following ways at the leading edge,

$$\frac{\partial \eta_{n=0}}{\partial x} = \frac{-\eta_{-1} + \eta_1}{2\delta x}, \quad (3.1.8)$$

$$= -\eta_{-1} + \eta_1, \quad (3.1.9)$$

$$\eta_{-1} = \eta_1. \quad (3.1.10)$$

Zero bending is applied through the second derivative,

$$\frac{\partial^2 \eta_{n=N}}{\partial x^2} = \frac{\eta_{N-1} - 2\eta_N + \eta_{N+1}}{\delta x^2}, \quad (3.1.11)$$

$$= \eta_{N-1} - 2\eta_N + \eta_{N+1}, \quad (3.1.12)$$

$$\eta_{N+1} = 2\eta_N - \eta_{N-1}, \quad (3.1.13)$$

and zero shear stress is applied through the third derivative,

$$\frac{\partial^3 \eta_{n=N}}{\partial x^3} = \frac{-\eta_{N-2} + 2\eta_{N-1} - 2\eta_{N+1} + \eta_{N+2}}{2\delta x^3}, \quad (3.1.14)$$

$$= -\eta_{N-2} + 2\eta_{N-1} - 2\eta_{N+1} + \eta_{N+2}, \quad (3.1.15)$$

$$= -\eta_{N-2} + 2\eta_{N-1} - 2\eta_{N+1} + (2\eta_{N+1} - \eta_N), \quad (3.1.16)$$

$$= -\eta_{N-2} + 2\eta_{N-1} - \eta_N. \quad (3.1.17)$$

3.1.2 Natural Frequencies

The natural frequencies of an *in vacuo* cantilevered plate each have an associated mode shape. These mode shapes are given by the equation (Nowacki [1963]),

$$\eta_x = C \left(U(\lambda_n x) - \frac{S(\beta_n)}{T(\beta_n)} V(\lambda_n x) \right). \quad (3.1.18)$$

Where $U(\lambda_n x)$, $S(\beta_n)$, $T(\beta_n)$, and $V(\lambda_n x)$ are given by,

$$\begin{aligned} U(\lambda_n x) &= \frac{\cosh(\lambda_n x) - \cos(\lambda_n x)}{2}, \\ S(\beta_n) &= \frac{\cosh(\beta_n) + \cos(\beta_n)}{2}, \\ T(\beta_n) &= \frac{\sinh(\beta_n) + \sin(\beta_n)}{2}, \\ V(\lambda_n x) &= \frac{\sinh(\lambda_n x) - \sin(\lambda_n x)}{2}, \end{aligned}$$

and C is a scaling constant and $\lambda_n = \beta_n/L$, where β_n are the solutions to,

$$\cosh \beta_n \cos \beta_n + 1 = 0,$$

the first four solutions of which are: $\beta_1 = 1.875$, $\beta_2 = 4.694$, $\beta_3 = 7.855$, and $\beta_4 = 10.996$, with the general solution $\beta_n = (2n - 1)\pi/2$. The mode shapes associated with these values of β_n are shown in Figure 3.3.

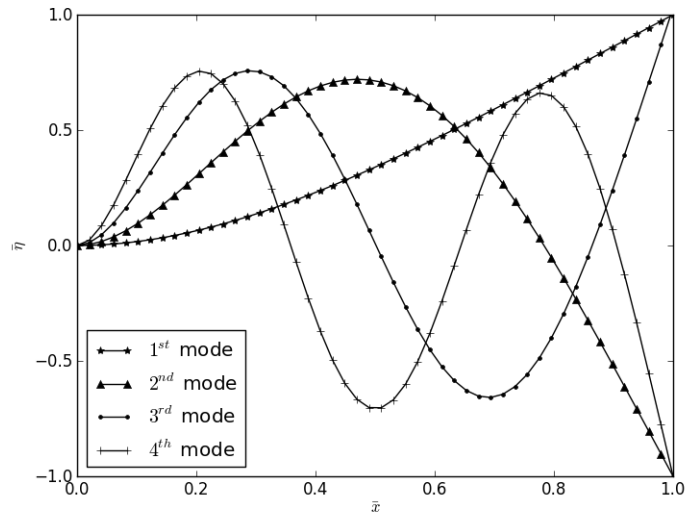


Figure 3.3: Modal deflections for the first four eigenmodes.

3.2 Fluid Model

The fluid is assumed to be ideal, hence potential-flow theory is used to predict the pressure exerted by the fluid owing to the motion of the flexible plate and is found through a panel/boundary-element method. Panel methods use a distribution of singularities over a surface in an infinite potential flow field to approximate that surface as a streamline of the flow. A combination of zero- and first-order vortices are used, providing constant and linearly varying vorticity along the length of a panel respectively. The effect of this is a continuously distributed vorticity along the cantilever. The adaptation of the panel method to the linear problem is now described.

3.2.1 Steady Flow Model

As the plate is able to change the momentum of the fluid and experience circulation the plate acts as a lifting surface. A single row of first-order vortices are used to model the cantilever as they can increase the velocity on one side of the cantilever while simultaneously decreasing the velocity on the other. Howell [2006] states that the use of a purely zero-order vortex method leads to correct but oscillatory solutions for velocity perturbation and potential. The use of first-

order vortices ensures a continuous variation of vorticity along the length of the cantilever, leading to a more stable result.

Formulation

The total velocity about a body of arbitrary shape in a uniform flow may be defined by \underline{u} ,

$$\underline{u} = \underline{U}_\infty + \underline{u}', \quad (3.2.1)$$

where \underline{U}_∞ is the free-stream flow and \underline{u}' is the disturbance perturbation due to the body (Houghton and Carpenter [1993]). As the disturbance is irrotational \underline{u}' may be written as $\nabla\phi$. Examining this relationship at the surface of the cantilever and applying the no-flux condition, which ensures that at the surface, the normal component of the total velocity is equal to the normal component of the plate velocity. This gives,

$$\underline{v}_p \cdot \underline{n} = \underline{U}_\infty \cdot \underline{n} + \nabla\phi \cdot \underline{n}, \quad (3.2.2)$$

where \underline{n} is a vector normal to the moving surface, and \underline{v}_p is the velocity of that surface. Owing to the linearity of the model the motion of the flexible surface is restrained to the y -direction, hence $\underline{v}_p = 0\underline{i} + \dot{\eta}\underline{j}$. The no-flux condition ensures that there is no net flow across the surface of the cantilever, and enables the strength of the vortices to be determined. Katz and Plotkin [2010] show how $\nabla\phi$ can be calculated as a combination of singularity strengths and corresponding influence coefficients. Howell [2006] demonstrates that when this is applied, Equation 3.2.2 becomes,

$$\underline{v}_p \cdot \underline{n} = \underline{U}_\infty \cdot \underline{n} + [I^{N_\gamma}] \gamma + [I^{N_\lambda}] \lambda, \quad (3.2.3)$$

where γ and λ are the zero- and first-order vortex strengths respectively. $[I^{N_\gamma}]$ and $[I^{N_\lambda}]$ are two $[M \times M]$ influence coefficient matrices which calculate the normal velocity induced by each vortex on each panel, where M is the number of panels. The zero-order and first-order vortex terms can be combined and solved

for using,

$$\begin{Bmatrix} \gamma \\ \dots \\ \lambda \end{Bmatrix} = [I^N]^{-1} \{ \underline{v}_p \cdot \underline{n} - \underline{U}_\infty \cdot \underline{n} \}, \quad (3.2.4)$$

where $[I^N]$ is a $[2M \times 2M]$ influence coefficient matrix which contains the vortex influence coefficients and boundary conditions, the layout of which is shown in Appendix A.1. The solution to Equation 3.2.4 is shown in Section 3.3.1. From these vortex strengths the tangential velocity and perturbation potential at any point can be found (Howell et al. [2009]),

$$u_i^{T'} = \sum_{m=1}^M [I^{T\gamma}]_{im} \gamma_m + \sum_{m=1}^M [I^{T\lambda}]_{im} \lambda_m, \quad (3.2.5a)$$

$$\phi_i = \sum_{m=1}^M [I^{\phi\gamma}]_{im} \gamma_m + \sum_{m=1}^M [I^{\phi\lambda}]_{im} \lambda_m, \quad (3.2.5b)$$

where the $[I^\phi]$ matrices are the perturbation potential influence coefficients for the zero- and first-order vortex distributions. Equations 3.2.5a and 3.2.5b can be used in the unsteady Bernoulli equation (shown in Appendix A.2) to calculate the pressure at control points located at the centre of each panel along the plate, which is shown in Figure 3.4.

Application

As the influence coefficients depend solely on the deflection of the plate, and owing to the small amplitude oscillations of the model, the vortices are assumed to lie along the x -axis at $y = 0$, as shown in Figure 3.4. This simplification allows for the pre-calculation of all the influence coefficients which otherwise would require calculation at every time step. This has been shown by Lucey [1989] to be an excellent approximation at very small displacements. The use of first-order vortices means that the vorticity at any point over the length of a panel is given by,

$$\gamma_\xi = \gamma_m + \xi \lambda_m, \quad (3.2.6)$$

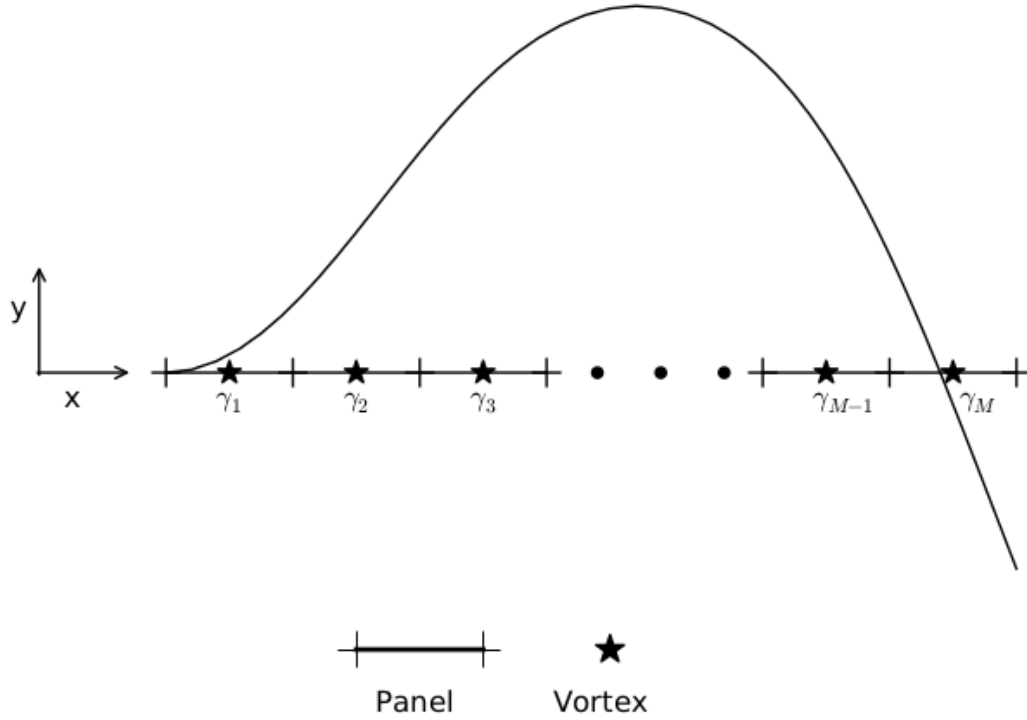


Figure 3.4: Singularity distribution along the cantilever.

where ξ varies linearly between $-\delta s/2$ and $\delta s/2$. This leads to $M - 1$ boundary conditions which enforce continuity of vorticity between panels,

$$\gamma_m + \frac{\delta s}{2} \lambda_m = \gamma_{m+1} - \frac{\delta s}{2} \lambda_{m+1}. \quad (3.2.7)$$

The Kutta condition provides the final boundary condition, implicitly introducing a viscous effect into the model allowing the plate to experience circulation, and hence act as a lifting surface. To satisfy the Kutta condition Howell [2006] proposes,

$$\gamma_{\text{TE}} + \lambda_{\text{TE}} \frac{s}{2} = 0, \quad (3.2.8)$$

which is enforced at the trailing edge (TE) of the cantilever. This condition is applied through the normal influence coefficient matrix, $[I^N]$.

3.2.2 Wake Model

Due to its motion, the vorticity bound within the cantilever changes over the course of an oscillation. To satisfy Kelvin's theorem (in potential flow), that there

can be no net change in circulation within a closed system in time, an amount of vorticity equal to the change in bound vorticity is shed as a discrete vortex from the trailing edge of the cantilever into the fluid, forming a wake. As a result of the inclusion of viscous effects, specifically, the shedding of vorticity into the flow the unsteady Bernoulli equation is no longer valid. However, for linear scale deflections the pressure difference across the boundary layer formed by the shedding of vorticity is small enough such that the pressure outside the boundary layer is a close approximation for the pressure at the surface of the cantilever. It has been shown by Cafolla [1997] that close to the surface of the cantilever the correct pressure equation gives approximately the same result as the unsteady Bernoulli equation.

Discrete Vortex Method

The wake is modelled using the discrete vortex method. The principles of the method are found in Chorin [1973]. The two-dimensional Navier-Stokes equations for an inviscid fluid reduce to,

$$\frac{D\zeta_f}{Dt} = 0, \quad (3.2.9)$$

where ζ_f is the vorticity in the flow. This vorticity is separated into discrete vortex “blobs” such that for N_b vortices,

$$\zeta_f = \sum_{n=0}^{N_b} \Gamma_n^b. \quad (3.2.10)$$

Where Γ^b is the strength of a wake vortex and the flow field created by each discrete vortex is perfectly cylindrical. The flow speed induced by a vortex blob at a distance r measured from the centre of the vortex to a point of interest, indicated by the subscript p , is given by,

$$u_p^b = \frac{\Gamma^b}{2\pi r}. \quad (3.2.11)$$

However, using Equation 3.2.11 leads to the velocity field becoming unbounded as r approaches 0, thus the Lamb-Oseen vortex equation is used (Saffman [1992]).

This modifies Equation 3.2.11 to give each vortex a viscous core (of diameter α) which prevents the velocity tending towards infinity close to the vortex (Lamb [1945], Saffman and Baker [1979]),

$$u_p^b = \frac{\Gamma^b}{2\pi r} (1 - \exp^{-r^2/\alpha^2}). \quad (3.2.12)$$

This can be separated into normal and tangential velocity components acting at point p in the flow,

$$u_p^{T_b} = \Gamma^b \frac{-y}{2\pi r^2} (1 - \exp^{-r^2/\alpha^2}), \quad (3.2.13a)$$

$$u_p^{N_b} = \Gamma^b \frac{x}{2\pi r^2} (1 - \exp^{-r^2/\alpha^2}). \quad (3.2.13b)$$

Where x and y are the horizontal and vertical components of \underline{r} . Thus the total velocity induced at a point by a wake vortex is,

$$\underline{u}_p^b = u^{T_b} \underline{i} + u^{N_b} \underline{j}. \quad (3.2.14)$$

Application

Owing to the very small oscillation amplitudes, the motion of the wake vortices is restrained in the y -direction. The wake vortices are shed only from the trailing edge of the cantilever, and their motion is not affected by the cantilever or other wake vortices. It is assumed therefore that the wake vortices travel downstream carried only by the free-stream velocity such that the distance between vortices is $U_\infty \delta t$. This enables the pre-calculation of the wake influences in the linear model. The restraining of vortices to lie along the x -axis, combined with the very small deflections experienced by the cantilever, reduce the tangentially-induced velocity given by Equation 3.2.13a to zero, hence,

$$\underline{u}_p^b = u^{T_b} \underline{i} + u^{N_b} \underline{j} = 0 \underline{i} + u^{N_b} \underline{j}. \quad (3.2.15)$$

Once created, the strength and core size of a vortex will not change in time, and the core size will be the same for all vortices. The velocity induced by the wake vortices is applied to the cantilever through the normal-boundary (no-flux)

condition (Equation 3.2.2). The effect of modifying the core size was explored in Howell [2006], where it is shown that a reduction in core size resulted in less travel downstream, but an increase in vorticity. Following the work presented by Howell et al. [2009], the magnitude of the core size, α , is assumed to be 0.4.

3.2.3 Unsteady Flow Model

The perturbation velocities generated by the panel method are used in the unsteady Bernoulli equation,

$$P + \frac{1}{2}\rho_f \underline{u} \cdot \underline{u} + \rho_f \frac{\partial \phi}{\partial t} = F(t), \quad (3.2.16)$$

where P is the pressure, ρ_f is the fluid density, and $F(t)$ is a time-dependant forcing term. At a point far from the cantilever the flow is undisturbed, so $\underline{u} = (U_\infty, 0)$. Following a streamline from this point to a point on the surface yields $\underline{u} = (U_\infty + u^{T'} + u^{T_b}, u^{N'} + u^{N_b})$, where $u^{T'}$ and $u^{N'}$ are the tangential and normal components of the perturbation velocity on the surface of the cantilever respectively. The discretization and linearisation of 3.2.16 is shown in Appendix A.2, and results in an equation for the pressure difference across the cantilever,

$$\delta p_i \Big|_{xp} = -2\rho_f U_\infty u_i^{T'} - \rho_f \frac{\partial \phi_i}{\partial t} \Big|_{xp}, \quad (3.2.17)$$

where i denotes a panel control point.

Tangential Velocity Perturbation

The tangential-velocity perturbation is given by the matrix form of Equation 3.2.5a,

$$\{u^{T'}\} = [I^{T\gamma}]\{\gamma\} + [I^{T\lambda}]\{\lambda\}, \quad (3.2.18)$$

which requires the calculation of vortex strengths. This is done by using Equation 3.2.4, the expansion and linearisation of which is shown in Appendix A.3 and

results in,

$$\{\gamma_i\} = [I^{N_\gamma}]^{-1}\{\dot{\eta}^{av} + U_\infty\theta - u^{N_b}\}, \quad (3.2.19a)$$

$$\{\lambda_i\} = [I^{N_\lambda}]^{-1}\{\dot{\eta}^{av} + U_\infty\theta - u^{N_b}\}. \quad (3.2.19b)$$

Where $\dot{\eta}^{av} = (\dot{\eta}_n + \dot{\eta}_{n+1})/2$ and θ is the angle of a panel to the horizontal, assuming $\theta \approx \sin\theta \approx \tan\theta$ for small values of θ . The averaging of the node velocity gives the velocity at the panel control point which is where the fluid calculations are performed. Inserting Equations 3.2.19a and 3.2.19b in to Equation 3.2.18 gives the final calculation for tangential perturbation velocity,

$$\begin{aligned} \{u_i^{T'}\} &= \left[[I^{T_\gamma}][I^{N_\gamma}]^{-1} + [I^{T_\lambda}][I^{N_\lambda}]^{-1} \right] \{\dot{\eta}^{av} + U_\infty\theta - u^{N_b}\}, \\ &= [\mathbf{A}]\{\dot{\eta}^{av} + U_\infty\theta - u^{N_b}\}. \end{aligned} \quad (3.2.20)$$

Unsteady Velocity Potential

As the velocity potential influence coefficients are constant with time, the change in velocity potential across the cantilever with respect to time is given by,

$$\left\{ \frac{\partial\phi}{\partial t} \right\} = [I^{\phi_\gamma}]\{\dot{\gamma}\} + [I^{\phi_\lambda}]\{\dot{\lambda}\}. \quad (3.2.21)$$

The derivation of the unsteady singularity strengths is shown in Appendix A.4. Undergoing the same process as was used in arriving at Equation 3.2.20 yields an expression for the unsteady velocity potential,

$$\begin{aligned} \left\{ \frac{\partial\phi}{\partial t} \right\} &= \left[[I^{\phi_\gamma}][I^{N_\gamma}]^{-1} + [I^{\phi_\lambda}][I^{N_\lambda}]^{-1} \right] \{\ddot{\eta} + U_\infty\dot{\theta} - \dot{u}^{N_b}\} \\ &= [\mathbf{B}]\{\ddot{\eta} + U_\infty\dot{\theta} - \dot{u}^{N_b}\}. \end{aligned} \quad (3.2.22)$$

Pressure Equation

Equations 3.2.20 and 3.2.22 are inserted in to Equation 3.2.17 yielding,

$$\begin{aligned}
 -\{\delta p\}|_{x_p} &= 2\rho_f U_\infty [\mathbf{A}]\{\dot{\eta} + U_\infty \theta - u^{N_b}\} + \rho_f [\mathbf{B}]\{\ddot{\eta} + U_\infty \dot{\theta} - \dot{u}^{N_b}\}, \\
 &= \underbrace{2\rho_f U_\infty^2 [\mathbf{A}]\{\theta\}}_{\text{Hydrodynamic stiffness}} + \underbrace{2\rho_f U_\infty [\mathbf{A}]\{\dot{\eta}^{av}\}}_{\text{Hydrodynamic damping I}} \\
 &+ \underbrace{\rho_f U_\infty [\mathbf{B}]\{\dot{\theta}\}}_{\text{Hydrodynamic damping II}} + \underbrace{\rho_f [\mathbf{B}]\{\ddot{\eta}\}}_{\text{Hydrodynamic inertia}} - \{\delta p^b\}, \quad (3.2.23)
 \end{aligned}$$

where δp^b is the pressure contribution due to the effect of the wake, the composition of which depends on the specific boundary condition applied to the wake. The named terms in Equation 3.2.23 refer to the effects of the fluid through components of the pressure term. The *hydrodynamic stiffness* term is proportional to the curvature of the cantilever. It arises due to the curvature of the cantilever and the resistance of the fluid to deformation. This is the primary component of the total pressure leading to divergence instability. The *hydrodynamic damping* terms are proportional to the rate of change of the slope and velocity of the cantilever. These terms relate to the stabilising or destabilising effect of the fluid motion, moving in or out of phase with cantilever movement. This is the pressure component primarily responsible for flutter instability. The *hydrodynamic inertia* or “added mass” term is proportional to the acceleration of the cantilever. This is the mass which is effectively added to the cantilever by the need to accelerate the fluid at the surface of the cantilever. When the free-stream velocity is reduced to zero this is the only pressure term that continues to affect the cantilever.

3.3 Computational Model Assembly

The linearised cantilever and fluid-flow models are now combined to produce three models capable of capturing the onset of instability in a full linear fluid-structure interaction system examining the method of applying the wake. Equation 3.2.23 can be written in terms of the plate displacement, velocity and acceleration (see

Appendix A.5),

$$\begin{aligned}
 -\{\delta p_m\}|_{xp} &= 2\rho_f U_\infty^2 \frac{1}{\delta x} [\mathbf{A}^-] \{\eta_m\} + \rho_f U_\infty [\mathbf{A}^+] \{\dot{\eta}_m\} \\
 &\quad + \rho_f U_\infty \frac{1}{\delta x} [\mathbf{B}^-] \{\dot{\eta}_m\} + \rho_f [\mathbf{B}] \{\ddot{\eta}_m\} - \{\delta p^b\}.
 \end{aligned} \tag{3.3.1}$$

Coupling Equation 3.3.1 and the discretized form of Equation 3.1.1,

$$\rho h [\mathbf{I}] \{\ddot{\eta}\} + d [\mathbf{I}] \{\dot{\eta}\} + B [\mathbf{D}_4] \{\eta\} = -\{\delta p\}|_{xp}, \tag{3.3.2}$$

and rearranging for $\ddot{\eta}$ yields,

$$\{\ddot{\eta}\} = [\mathbf{E}] \{\dot{\eta}\} + [\mathbf{F}] \{\eta\} - [\mathbf{G}] \{u^{N_b}\} - [\mathbf{H}] \{\dot{u}^{N_b}\}. \tag{3.3.3}$$

Where $[\mathbf{E}]$, $[\mathbf{F}]$, $[\mathbf{G}]$, and $[\mathbf{H}]$ are combinations of influence coefficients, their composition depending on the wake model employed. Equation 3.3.3 is solved using two methods - firstly a full numerical simulation, and secondly an eigenanalysis - solving the systems shown in Figures 3.5 and 3.6 respectively.

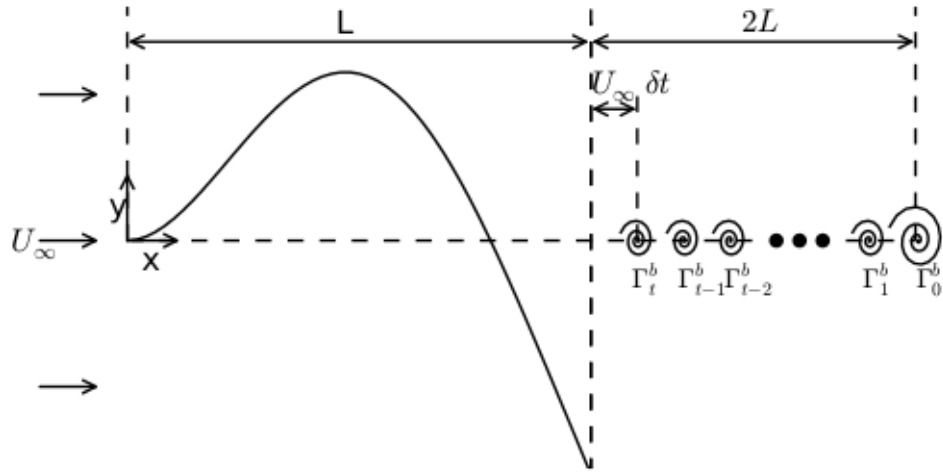


Figure 3.5: The system studied in the full numerical simulation.

3.3.1 Initial Value Problem

This model is based on that developed in Howell et al. [2009] and describes the system shown in Figure 3.5. The plate is given an arbitrary initial deflection to begin the simulation. Then the vertical displacement of the mass points is

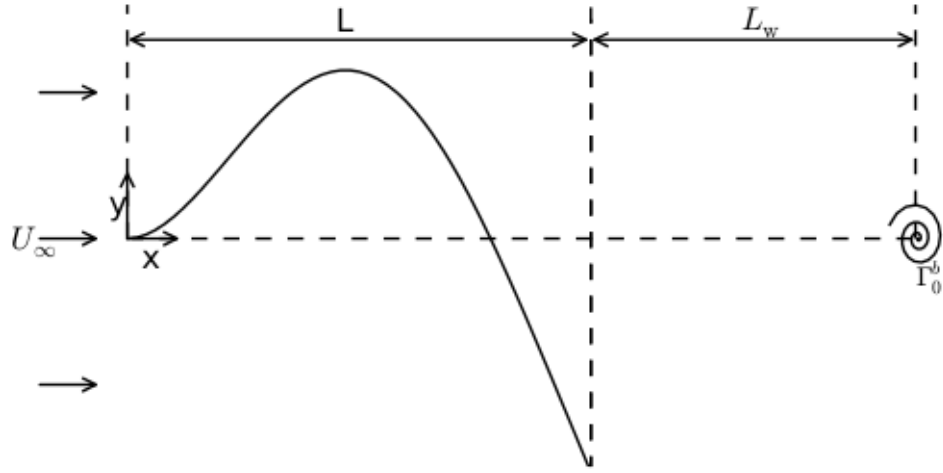


Figure 3.6: The system solved through eigenanalysis.

calculated iteratively at a series of time steps. A wake vortex is to be released every time step. The strength of the wake vortex released at each time step is calculated using the Kelvin condition, that there is no change in circulation within a closed system in time. At $t = 0$ in the simulation, all the vorticity is contained within the cantilever. As vorticity must be conserved and can not change in time, this is the maximum vorticity present in the system at all subsequent time steps,

$$\zeta_{total} = \zeta^{t=0} = \sum_{i=0}^M \gamma_i^{t=0} \delta x. \quad (3.3.4)$$

Hence the strength of the wake vortex released at time t is equal to the difference between the total vorticity at time $t = 0$, the bound vorticity at time t , and the total vorticity contained within the wake (excluding the vortex forming at time t). This is given by,

$$\Gamma^{b,t} = \zeta_{total} - \left(\sum_{i=0}^M \gamma_i^t \delta x + \sum_{i=0}^{t-1} \Gamma_i \right). \quad (3.3.5)$$

Vortices enter the wake a distance of $U_\infty \delta t$ from the trailing edge of the cantilever, and maintain this distance between other wake vortices. A *cut-off length* of $2L$ is enforced; vortices that have travelled past this point are removed and their strengths summed into a far-wake strength variable. For this method of applying

the wake the derivation of Equation 3.3.1 results in,

$$-\{\delta p\}_{\text{ns}}^b = - \underbrace{2\rho_f U_\infty [\mathbf{A}]}_{\text{Hydrodynamic damping}} \{u^{N_b}\} - \underbrace{\rho_f [\mathbf{B}]}_{\text{Hydrodynamic inertia}} \{\dot{u}^{N_b}\} . \quad (3.3.6)$$

Where the forms of the matrices in Equation 3.3.3 for this method are,

$$[\mathbf{E}]_{\text{ns}} = [\mathbf{C}]_{\text{ns}}^{-1} \left[\rho_f U_\infty [\mathbf{A}^+] + \rho_f U_\infty [\mathbf{B}^-] \right], \quad (3.3.7a)$$

$$[\mathbf{F}]_{\text{ns}} = [\mathbf{C}]_{\text{ns}}^{-1} \left[2\rho_f U_\infty^2 [\mathbf{A}^-] - \mathbf{B}[\mathbf{D}_4] \right], \quad (3.3.7b)$$

$$[\mathbf{G}]_{\text{ns}} = [\mathbf{C}]_{\text{ns}}^{-1} \left[2\rho_f U_\infty [\mathbf{A}] \right], \quad (3.3.7c)$$

$$[\mathbf{H}]_{\text{ns}} = [\mathbf{C}]_{\text{ns}}^{-1} \left[\rho_f [\mathbf{B}] \right], \quad (3.3.7d)$$

where,

$$[\mathbf{C}]_{\text{ns}} = \left[\rho h [\mathbf{I}] - \rho_f [\mathbf{B}] \right]. \quad (3.3.8)$$

Using Equation 3.3.3 it is possible to predict nodal velocity and displacement at each time step using semi-implicit Crank-Nicholson type approximations,

$$\{\dot{\eta}\}^{t+\delta t} = \{\dot{\eta}\}^t + \frac{\{\ddot{\eta}\}^{t+\delta t} + \{\ddot{\eta}\}^t}{2} \delta t, \quad (3.3.9a)$$

$$\{\eta\}^{t+\delta t} = \{\eta\}^t + \frac{\{\dot{\eta}\}^{t+\delta t} + \{\dot{\eta}\}^t}{2} \delta t. \quad (3.3.9b)$$

Equations 3.3.3, 3.3.9a, and 3.3.9b are solved iteratively at each time step using Gauss-Siedel sweeps over the beam mass points to predict the acceleration, velocity, and displacement of the mass points along the beam. This model is initiated in two ways; the cantilever is given an initial deflection, or an impulse is applied to the trailing edge of the cantilever at time $t = 0$. In each case, the combined influence coefficient matrices (in Equations 3.3.7a-d) are then calculated. The model then estimates values for $\eta^{t+\delta t}$, $\dot{\eta}^{t+\delta t}$ and $\ddot{\eta}^{t+\delta t}$ iteratively until these terms are converged before moving on to the next time step where this process is repeated.

3.3.2 Eigenanalysis

Figure 3.6 shows the layout of the system to be modelled using eigenanalysis. A boundary-value model is employed to determine the infinite-time system behaviour using a state-space method similar to that described in Howell et al. [2009] and Pitman and Lucey [2009]. Choosing,

$$w_1(t) = \eta(t), \quad (3.3.10a)$$

$$w_2(t) = \dot{\eta}(t) = \dot{w}_1(t), \quad (3.3.10b)$$

$$\dot{w}_2(t) = \ddot{\eta}(t), \quad (3.3.10c)$$

for the state-space variables, the second-order system developed (Equation 3.3.3) is reduced to a first-order problem. Equations 3.3.10a, b, and c are substituted into Equation 3.3.3 and the matrices are rearranged to form a $2N \times 2N$ companion matrix $[\mathbf{H}]$,

$$\begin{aligned} \begin{Bmatrix} \dot{w}_1 \\ \dot{w}_2 \end{Bmatrix} &= \begin{bmatrix} \mathbf{0} & \mathbf{I} \\ \mathbf{F} & \mathbf{E} \end{bmatrix} \begin{Bmatrix} w_1 \\ w_2 \end{Bmatrix}, \\ \{\dot{w}\} &= [\mathbf{H}]\{w\}. \end{aligned} \quad (3.3.11)$$

Assuming a single-frequency response where all perturbations are $\propto e^{i\omega t}$ where $\omega = \omega_R + i\omega_I$. Once the companion form has been assembled, the eigenvalues are extracted: these have both a real and imaginary component which quantify the coupled system stability and oscillation frequency respectively. The wake is modelled using a single vortex, this allows the wake to be described entirely in terms of η and $\dot{\eta}$. This results in the $[\mathbf{G}]$ and $[\mathbf{H}]$ matrices in Equation 3.3.3 no longer being required. The strength of the single wake vortex is based on two different interpretations of the Kelvin condition,

$$\Gamma_1^b = \sum \frac{\delta\gamma}{\delta t} \delta x T, \quad (3.3.12a)$$

or

$$\Gamma_2^b = - \sum \gamma \delta x, \quad (3.3.12b)$$

and is placed at a distance L_w from the trailing edge of the cantilever where $L_w = U_\infty T$, T being the period of oscillation. Equation 3.3.12a assumes that the vorticity entering the wake is equal to the change in bound vorticity in time, while Equation 3.3.12b (from the studies of Giesing [1968, 1969, 1970]) sets the wake vorticity equal and opposite to the bound vorticity. These two conditions lead to two different models that are described below.

Model 1

Equation 3.3.12a enforces the condition that the wake vortex must have a strength equal to the change in bound vorticity during an oscillation of the cantilever. Substituting Equation 3.2.4 in to Equation 3.3.12a yields,

$$\begin{aligned}\Gamma_1^b &= \delta x_i T \left(\frac{1}{\delta x_i} U_\infty [\mathbf{I}^{\mathbf{N}}]^{-1-+} \{\dot{\eta}\} + [\mathbf{I}^{\mathbf{N}}]^{-1+} \{\ddot{\eta}\} \right), \\ &= T U_\infty [\mathbf{I}^{\mathbf{N}}]^{-1-+} \{\dot{\eta}\} + \delta x_i T [\mathbf{I}^{\mathbf{N}}]^{-1+} \{\ddot{\eta}\}.\end{aligned}\quad (3.3.13)$$

The ‘-+’ superscript denotes that the matrix was first differenced along each row, then summed down each column, whereas the lone ‘+’ denotes a summing along each row following the process outlined in Appendix A.6. Equation 3.3.13 is applied through Equations 3.2.20 and 3.2.22, and results in a wake-induced pressure contribution given by,

$$-\{\delta p\}_1^b = \underbrace{-2\rho_f L_w U_\infty [\mathbf{P}]_1 \{\dot{\eta}\}}_{\text{Hydrodynamic damping}} - \underbrace{2\rho_f L_w [\mathbf{Q}]_1 \{\ddot{\eta}\} - \rho_f L_w [\mathbf{R}]_1 \{\ddot{\eta}\}}_{\text{Hydrodynamic inertia}}. \quad (3.3.14)$$

Where the $[\mathbf{P}]_1$, $[\mathbf{Q}]_1$ and $[\mathbf{R}]_1$ matrices are further combinations of influence coefficients. Inserting Equation 3.3.14 into Equation 3.3.1 and rearranging into the form of Equation 3.3.3 yields,

$$[\mathbf{E}]_1 = [\mathbf{C}]_1^{-1} \left[\rho_f U_\infty ([\mathbf{A}^+] + [\mathbf{B}^-] - 2L_w [\mathbf{P}]_1) \right], \quad (3.3.15)$$

$$[\mathbf{F}]_1 = [\mathbf{C}]_1^{-1} \left[2\rho_f U_\infty^2 [\mathbf{A}^-] - B[\nabla^4] \right], \quad (3.3.16)$$

$$[\mathbf{C}]_1 = [\rho h [\mathbf{I}] - \rho_f [\mathbf{B}] + 2\rho_f L_w [\mathbf{Q}]_1 + \rho_f L_w [\mathbf{R}]_1]. \quad (3.3.17)$$

An initial guess for L_w is made and several iterations of the system are required to finalise the location of the wake vortex. The temporal change in wake strength present in Equation 3.3.12a gives rise to a *jerk* term that is a third-order time derivative of η : to retain the $(2N \times 2N)$ shape of the state-space companion matrix we neglect this term - the validity of this omission is tested using the initial-value method in the results chapter below.

Model 2

Equation 3.3.12b, used in Giesing [1969], states that the “vorticity in the wake” is equal and opposite to that in the cantilever at all times. Applying this equation in the same fashion as in Model 1, the pressure contribution from the wake in this case is,

$$-\{\delta p\}_2^b = -\rho_f \left(\underbrace{2U_\infty^2 [\mathbf{P}]_2 \{\eta\}}_{\text{Hydrodynamic stiffness}} + \underbrace{U_\infty [\mathbf{Q} + \mathbf{R}]_2 \{\dot{\eta}\}}_{\text{Hydrodynamic damping}} + \underbrace{[\mathbf{S}]_2 \{\ddot{\eta}\}}_{\text{Hydrodynamic inertia}} \right). \quad (3.3.18)$$

Where $[\mathbf{P}]_2$, $[\mathbf{R}]_2$, $[\mathbf{Q}]_2$, and $[\mathbf{S}]_2$ are once again combinations of influence coefficients. Inserting Equation 3.3.18 into Equation 3.3.1 and rearranging into the form of Equation 3.3.3 yields,

$$[\mathbf{E}]_2 = [\mathbf{C}]_2^{-1} \left[\rho_f U_\infty ([\mathbf{A}^+] + [\mathbf{B}^-] - [\mathbf{Q}]_2 - [\mathbf{R}]_2) \right], \quad (3.3.19)$$

$$[\mathbf{F}]_2 = [\mathbf{C}]_2^{-1} \left[2\rho_f U_\infty^2 ([\mathbf{A}^-] - [\mathbf{P}]_2) - B[\nabla^4] \right], \quad (3.3.20)$$

$$[\mathbf{C}]_2 = [\rho h[\mathbf{I}] - \rho_f[\mathbf{B}] + \rho_f[\mathbf{S}]_2]. \quad (3.3.21)$$

The jerk term does not arise in this second model as there is no time differential of the lumped-vortex strength in Equation 3.3.12b; therefore, L_w is also absent from Equation 3.3.18 as there is now no need to balance the additional time term - however, as in model 1 the wake vortex is located at L_w from the trailing edge of the plate and it is again necessary to iterate to find the position of the wake vortex. This is because the frequency of the plate is affected by the position of the wake vortex, and the position of the wake vortex relates to the frequency of oscillation.

3.3.3 System Non-dimensionalisation

Howell [2006] reduced the system to two control parameters using the method of Crighton and Oswell [1991]. The system equation is assembled by combining the beam equation and the unsteady Bernoulli equation (Equations 3.1.1 and 3.2.17 respectively).

$$\rho h \frac{\partial^2 \eta}{\partial t^2} + d \frac{\partial \eta}{\partial t} + B \frac{\partial^4 \eta}{\partial x^4} = -\delta p = 2\rho_f U_\infty u^{T'} + \rho_f \frac{\partial \phi}{\partial t}. \quad (3.3.22)$$

Non-dimensional forms of individual properties are found by comparing the dimensional form with a reference length (L_r) or time (T_r),

$$\eta = \bar{\eta} L_r, \quad x = \bar{x} L_r, \quad t = \bar{t} T_r, \quad U_\infty = \bar{U} \frac{L_r}{T_r}, \quad \phi = \bar{\phi} \frac{L_r^2}{T_r}, \quad u^{T'} = \bar{u}^{T'} \frac{L_r}{T_r}, \quad (3.3.23)$$

where T_r and L_r have units of seconds and metres respectively. Substituting these relationships in to Equation 3.3.22 yields,

$$\begin{aligned} \rho h \frac{L_r}{T_r^2} \frac{\partial^2 \bar{\eta}}{\partial \bar{t}^2} + d \frac{L_r}{T_r} \frac{\partial \bar{\eta}}{\partial \bar{t}} + B \frac{1}{L_r^3} \frac{\partial^4 \bar{\eta}}{\partial \bar{x}^4} &= 2\rho_f \frac{L_r^2}{T_r^2} \bar{U} \bar{u}^{T'} + \rho_f \frac{L_r^2}{T_r^2} \frac{\partial \bar{\phi}}{\partial \bar{t}}, \\ \rho h \frac{1}{L_r} \frac{\partial^2 \bar{\eta}}{\partial \bar{t}^2} + d \frac{T_r}{L_r} \frac{\partial \bar{\eta}}{\partial \bar{t}} + B \frac{T_r^2}{L_r^5} \frac{\partial^4 \bar{\eta}}{\partial \bar{x}^4} &= 2\rho_f \bar{U} \bar{u}^{T'} + \rho_f \frac{\partial \bar{\phi}}{\partial \bar{t}}. \end{aligned} \quad (3.3.24)$$

Choosing,

$$L_r = \frac{\rho h}{\rho_f}, \quad T_r = \frac{(\rho h)^{5/2}}{\rho_f^2 B^{1/2}}, \quad \text{and} \quad \bar{d} = d \frac{(\rho h)^{3/2}}{\rho_f^2 B^{1/2}}, \quad (3.3.25)$$

where L_r is the standard length scale used in this type of FSI problem (for example, Zhao et al. [2012]). Equation 3.3.24 becomes,

$$\frac{\partial^2 \bar{\eta}}{\partial \bar{t}^2} + \bar{d} \frac{\partial \bar{\eta}}{\partial \bar{t}} + \frac{\partial^4 \bar{\eta}}{\partial \bar{x}^4} = 2\bar{U} \bar{u}^{T'} + \frac{\partial \bar{\phi}}{\partial \bar{t}}. \quad (3.3.26)$$

There are now two control parameters governing the system response, \bar{U} and \bar{d} , where \bar{U} is a non-dimensionalised flow speed and is given by,

$$\bar{U} = U_\infty \frac{T_r}{L_r} = U_\infty \frac{(\rho h)^{3/2}}{\rho_f B^{1/2}}. \quad (3.3.27)$$

The mass ratio, (\bar{L}), is a further control parameter, for a plate of finite length, L ,

$$\bar{L} = \frac{\rho_f L}{\rho h}. \quad (3.3.28)$$

The non-dimensional angular frequency of oscillation of the plate is given by,

$$\bar{\omega} = \omega \frac{(\rho h)^{5/2}}{\rho_f^2 B^{1/2}}. \quad (3.3.29)$$

When plotting results for the linear model real and imaginary non-dimensional frequencies from the state-space models are given by $\bar{\omega}$. For plate deflections the non-dimensional forms of distance along the plate and the plate deflection are $\bar{x}(= x/L)$ and $\bar{\eta}$; in the latter, values of η are normalised by the value of initial maximum-deflection for the initial-value problem or the overall maximum-deflection for the boundary-value problem.

Chapter 4

Validation

This chapter covers the validation of the linear plate, fluid, wake, and flow models and their combination in to computational models as discussed in the linear theory section. The results have been non-dimensionalised with the scheme described in Section 3.3.3 except in the *in vacuo* cases where $\rho_f = 0$, otherwise $\rho_f = 1 \text{ kg/m}^3$. For the purposes of validation, the plate energy will also be calculated. It has been shown by Balint and Lucey [2005] that multiplying Equation 3.1.1 by $\dot{\eta}$ and integrating along the length of the plate yields expressions for the strain (E_s) and kinetic (E_k) energies of the plate,

$$E_s = \frac{1}{2}B \int_0^L \left(\frac{\delta^2 \eta}{\delta x^2} \right)^2 dx, \quad (4.0.1a)$$

$$E_k = \frac{1}{2}\rho h \int_0^L \dot{\eta}^2 dx. \quad (4.0.1b)$$

The total plate energy (E_t) is given by $E_s + E_k$. E_t can also be given by $\delta p \dot{\eta} + d\dot{\eta}^2$ as shown by Howell et al. [2009]. In non-zero damping cases the dissipated energy is ignored. In the results the energy is normalised by the total energy at time $t = 0$.

4.1 Plate Model

The plate model is validated in three ways; the computed period of oscillation is compared to analytical values, the kinetic and potential energies are calculated over the course of several oscillations, and finally the effect of damping is exam-

ined. In each of these validation steps the mechanical properties of the plate are chosen to be the same as those used in Howell et al. [2009]: $E = 7 \times 10^7$ N/m², $\rho = 2710$ kg/m³, $\nu = 0.3$, $h = 5 \times 10^{-4}$ m and $L = 1.355$ m. Energy is initially given to the beam by deflecting the beam into one of the fundamental eigenmodes before being released and allowed to oscillate freely. In the undamped *in vacuo* case the energy in the system is wholly contained within the beam and does not dissipate over time. Thus there is no net change in energy in time and kinetic and potential energy change in perfect antiphase. This is shown in Figures 4.1 a-d, where the energy development in time is shown as well as the form of the oscillation for each of the first four modes. These figures show that the beam undergoes stable neutral oscillations fully recovering the mode shape into which it was initially deflected. The theoretical period of oscillation can be calculated analytically using,

$$\omega_n = \frac{\beta_n^2}{L^2} \sqrt{\frac{B}{\rho h}}, \quad (4.1.1)$$

where values for β_n are the solutions to the transcendental equation $\cosh \beta_n \cos \beta_n + 1 = 0$. For example, $\beta_1 = 1.875$, $\beta_2 = 4.694$, $\beta_3 = 7.855$, $\beta_4 = 10.996$. The accuracy of the observed oscillation frequency depends upon the level of discretization of the plate. To examine this dependence, the beam was initially deflected into each of the first four mode shapes shown in Figure 3.3 and the progress of a single node was tracked over several oscillations before being used to calculate the period. Table 4.1 shows that a discretization of 50 nodes gives very good agreement with the theoretical values of oscillation period when the beam is *in vacuo*. The increase in plate resolution is accompanied by a rapid increase in computational load, resulting in much longer model run times (of the order of 10 times those of the coarser models). Figures 4.2 (a) and (b) show the gradual decrease in beam energy and oscillation amplitude that occurs when the *in vacuo* beam is subjected to damping.

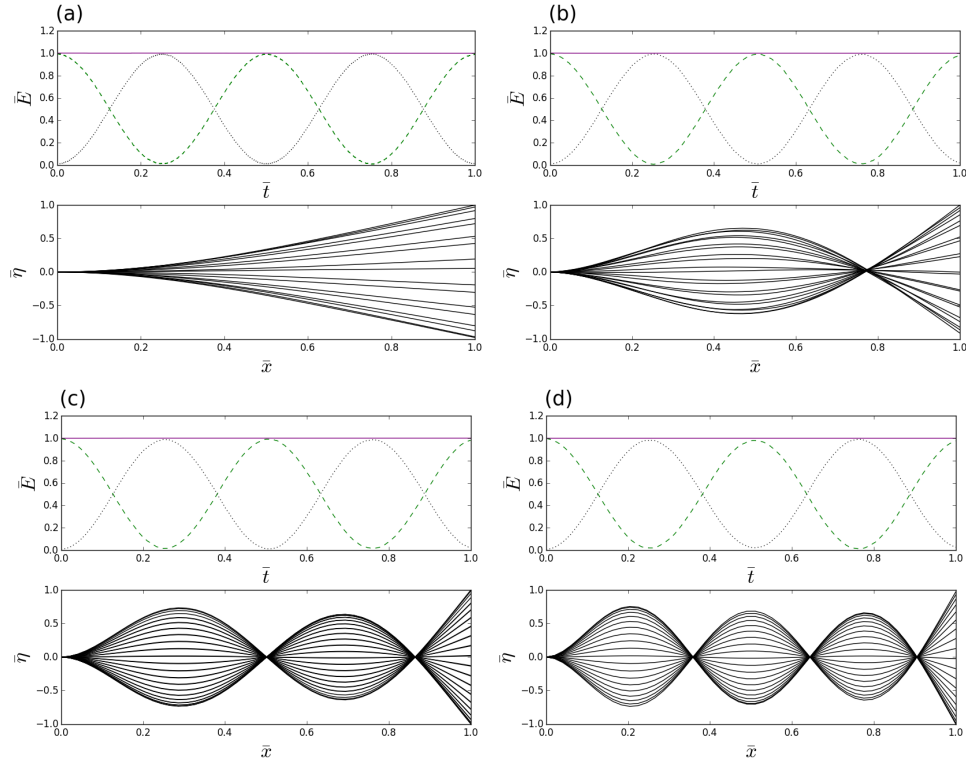


Figure 4.1: *In vacuo* plate model using 50 nodes initially deflected into the first four eigenmodes in a, b, c, and d respectively. The total, strain, and kinetic energies are the solid, dashed, and dotted lines respectively in each subfigure.

Table 4.1: Simulated oscillation frequencies at various levels of discretization.

Mode	Theoretical Period (/s)	Simulation period (/s)		
		50 nodes	100 nodes	200 nodes
1	133.363	132.479	133.102	133.363
2	21.279	21.123	21.201	21.278
3	7.541	7.480	7.513	7.540
4	3.878	3.829	3.855	3.878

4.2 Fluid Model

The fluid-flow model was first applied to a NACA 4412 aerofoil, with the panels distributed evenly along the upper and lower surface of the aerofoil geometry. The resulting pressure coefficients are shown in Figure 4.3, these are compared with the experimental and numerical results presented in Houghton and Carpenter [1993] who arranged their panels similarly. The pressure coefficients from the present numerical model are very similar to those of Houghton and Carpenter. There is a difference between the numerical and experimental results, particularly on the upper surface. This is the result of the exclusion of viscosity in the numer-

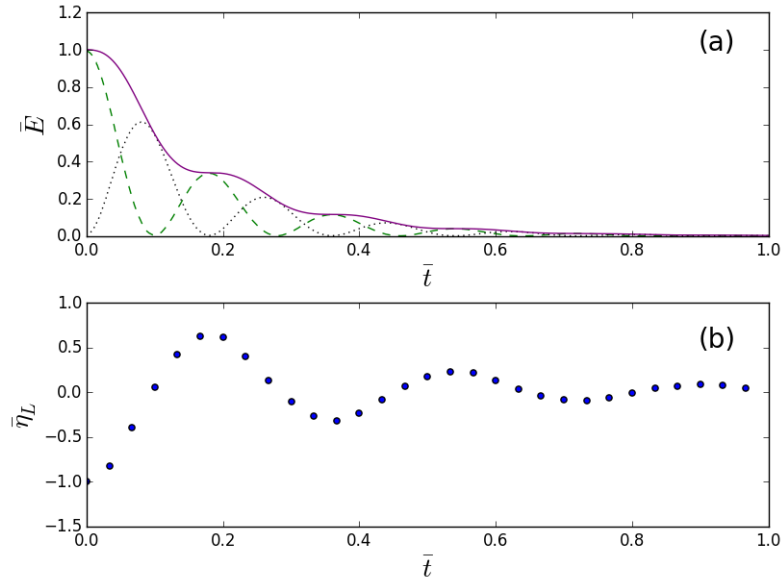


Figure 4.2: The total (—), kinetic (···), and strain (---) energies, (a), and tip deflection, (b), of a cantilever initially deflected into the second mode with damping $d = 0.05 \text{ kg/sm}^2$ using 50 nodes.

ical models and the relatively high angle of attack. However at lower angles of attack the experimental and theoretical results converge. This lends confidence to the validity of the fluid model for scenarios where the amplitude of oscillation is very small. Better agreement the theoretical result and the experimental could have been obtained with a non-linear arrangement of panels, with finer resolution at the leading edge to better capture the curvature of the surface. However the final numerical model presented will have a linear distribution of panels, and having the panels arranged in this way allows a better comparison with other theoretical results. When applied to the fluid-structure system the pressures calculated along the surface of a static, deflected plate compare very well to those presented in Howell [2006], shown in Figure 4.4. The pressure can be seen to decrease in regions of high velocity where the curvature of the beam is high.

4.3 Unsteady Model

At a critical flow speed, U_c , the energy transferred between the fluid and the solid will be in balance and the system will enter neutrally-stable oscillations. The modal shape of the oscillations at U_c is termed the critical mode. Above or below this critical speed the amplitude of plate oscillation will increase or

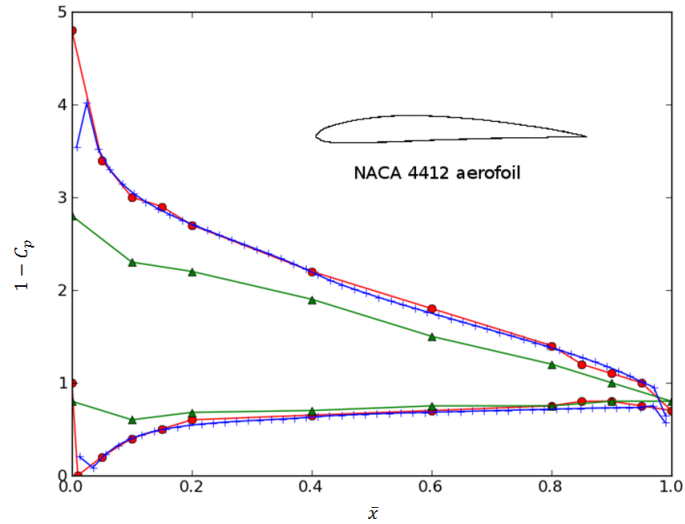


Figure 4.3: Fluid model results comparison between the current model (+), and experimental (Δ) and theoretical (\bullet) results obtained by Houghton and Carpenter [1993] for a NACA 4412 aerofoil at an 8° angle of attack.

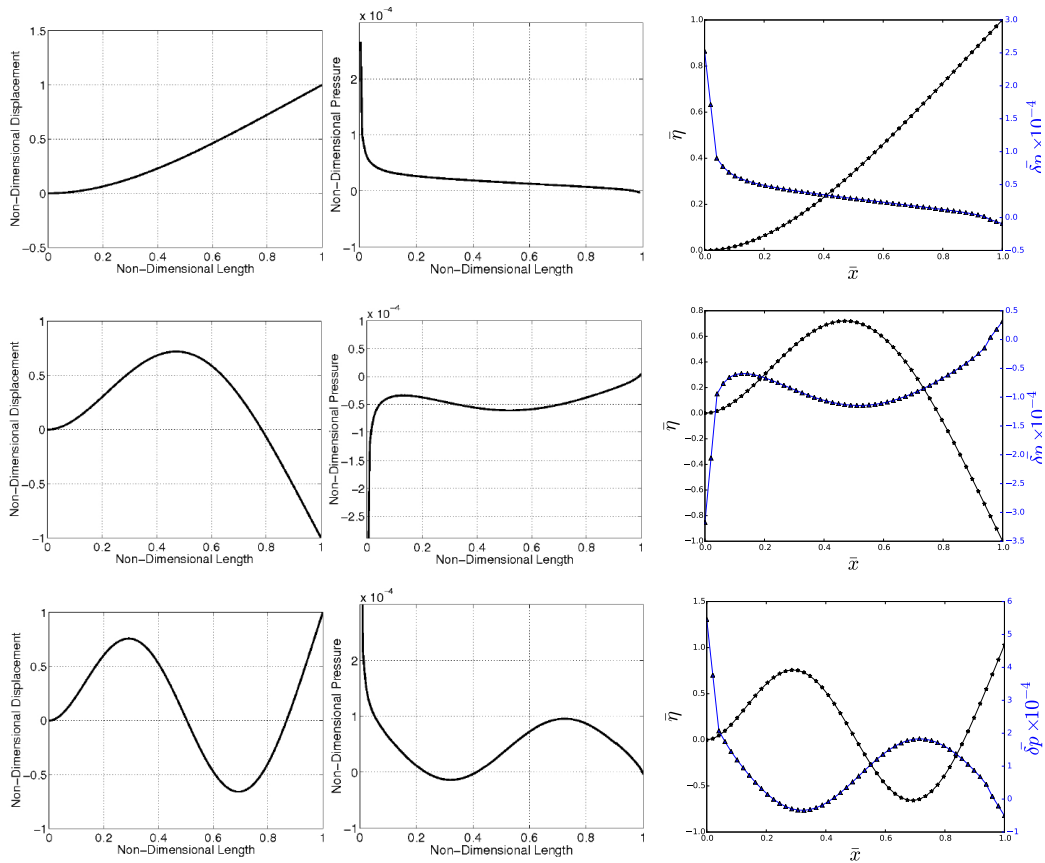


Figure 4.4: Pressure distribution and deflection given by the current model (right) and that in Howell [2006] (left, centre). 50 nodes are used and the plate is deflected in to the first three normal modes in rows 1, 2, and 3 respectively.

decrease respectively. For $\bar{L} = 1$, U_∞ was varied until U_c was reached. The plate deflections and energies for an oncoming flow speed less than, equal to, and

greater than the critical flow velocity are shown in Figure 4.5. When given the same initial deflection of the second eigenmode at each flow speed the amplitude of oscillation and the energy in each case behaves as expected, decreasing for $U_\infty < U_c$, remaining constant at $U_\infty = U_c$, and increasing for $U_\infty > U_c$. For the cases shown in the top and bottom sub-figures of Figure 4.5, the system has not reached an equilibrium by the end of the time period shown, and so the oscillation envelopes appear to narrow and grow respectively around a non-zero position. It is shown that the form of the oscillation is in the second mode, this is also found by Howell et al. [2009] and Huang [1995]. When initially deflected into a different eigenmode the oscillations return to the form of the second eigenmode after sufficient time has passed in the simulation. A comparison between the results of Howell et al. [2009] and the current model is made in Table 4.2, and discussed in Section 4.5.

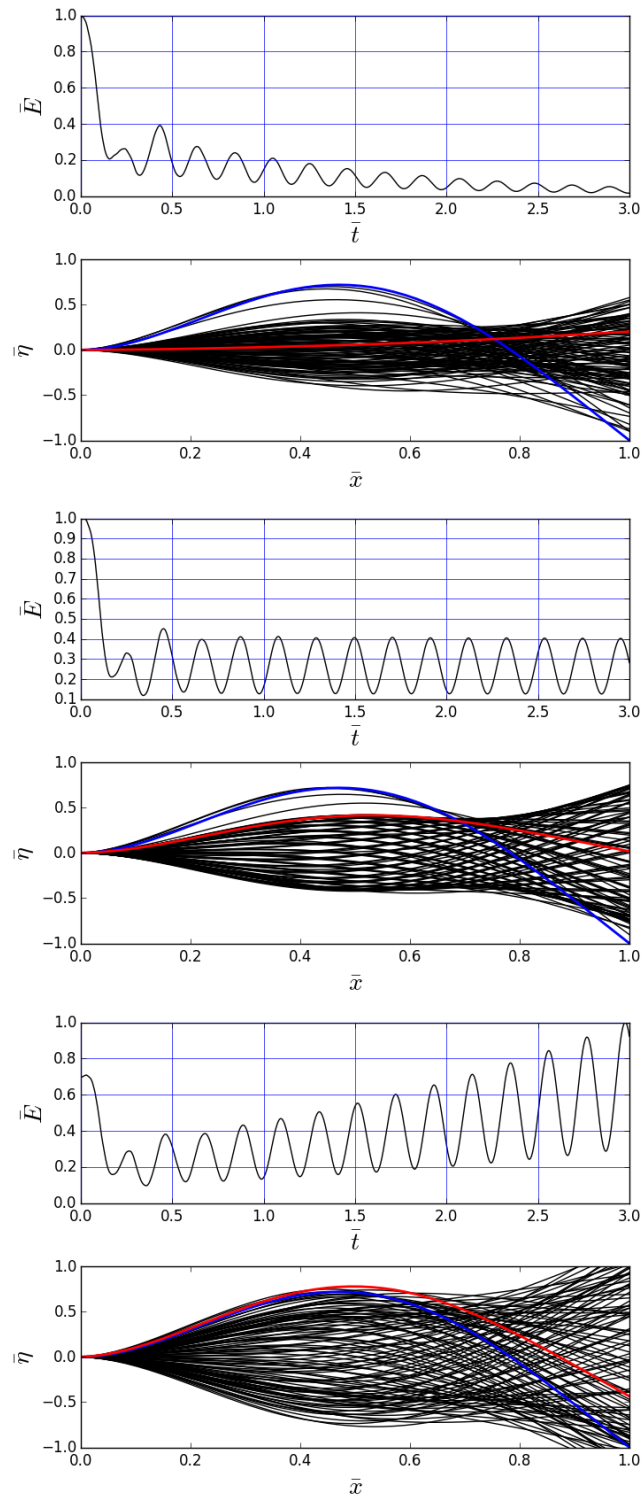


Figure 4.5: The energy and deflection of a cantilever plate at; (top) $U_\infty < U_c$, (middle) $U_\infty = U_c$, and (bottom) $U_\infty > U_c$. The initial and final deflections are shown by the blue and red lines respectively.

4.4 Wake Model

To validate the vorticity model, it was applied to a model of a heaving plate in axial flow and compared to experimental results found in the literature. The properties of the plate, frequency, and flow speed were chosen to match those presented in Paraz et al. [2014] and the model allowed to run for 200 time steps. The result of this simulation and a figure adapted from Paraz et al. [2014] are shown in Figure 4.6(a) and (b) respectively. In the numerical model the characteristic Von-Karman vortex street is seen to form at the trailing edge of the plate (at $x = 0$), and the form of the wake is very similar to that shown in the experimental results by Paraz et al. [2014]. However, as the current model is an inviscid calculation the diffusion of vorticity seen in the experimental results is not captured.

4.5 Full Numerical Model

When the model is fully assembled and the wake and unsteady models are combined the wake has a stabilising or destabilising affect on the plate depending on the mass ratio. Table 4.2 lists the critical flow speeds predicted by the current model without (\bar{U}_c) and with (\bar{U}_c^*) a wake, comparing the latter with the corresponding results in Howell et al. [2009] along with percentage difference between the two. Very good agreement is seen and by comparing these critical speeds with those predicted in the absence of a wake, the effect of the wake on the FSI system is seen to be stabilising for plates with low \bar{L} and destabilising for those with high \bar{L} . An explanation for this is given in Howell et al. [2009]; the wake modifies the phase difference between pressure and plate velocity. For short (low \bar{L}) plates whose instability is dominated by single-mode flutter this change in phase slows the rate of energy transfer between the plate and the fluid, increasing the critical velocity. For longer plates (high \bar{L}) this change of phase owing to the wake results in a slightly destabilising effect because they are destabilised primarily by modal-coalescence flutter which is promoted when a wake is present. The discretization of the beam would lead to increased errors in subsequent models (specifically the wake model) which rely on the number of nodes on the plate surface as the

interface between the two models. However, for Table 4.2 the number of nodes for both the with- and without- a wake models was constant, so the entire error can be attributed to the addition of the wake model.

Table 4.2: Dependence of critical speed on mass ratio (non-dimensional plate length) and comparison of present results with those of Howell et al. [2009].

\bar{L}	\bar{U}_c	$\bar{U}_{c, \text{Howell et al. [2009]}}^*$	\bar{U}_c^*	% Difference
0.6	9.65	11.47	11.65	1.57
1.0	5.50	5.95	5.73	3.70
1.2	4.60	4.73	4.68	1.06
1.4	4.01	3.95	3.97	0.51
1.6	3.63	3.44	3.47	0.87

4.6 Summary

A discretization of 50 mass points will be used for the plate in numerical simulations as it has been found that this provides a suitable compromise between accuracy and computation time. To reduce the time needed for numerical models to reach a steady state the plate will be initially deflected into the second mode, as this has been shown to be the critical mode. Very good agreement has been found between the fully assembled model and the model presented in Howell et al. [2009]. Thus it is proposed that the numerical model has been sufficiently validated and can be used to generate new results.

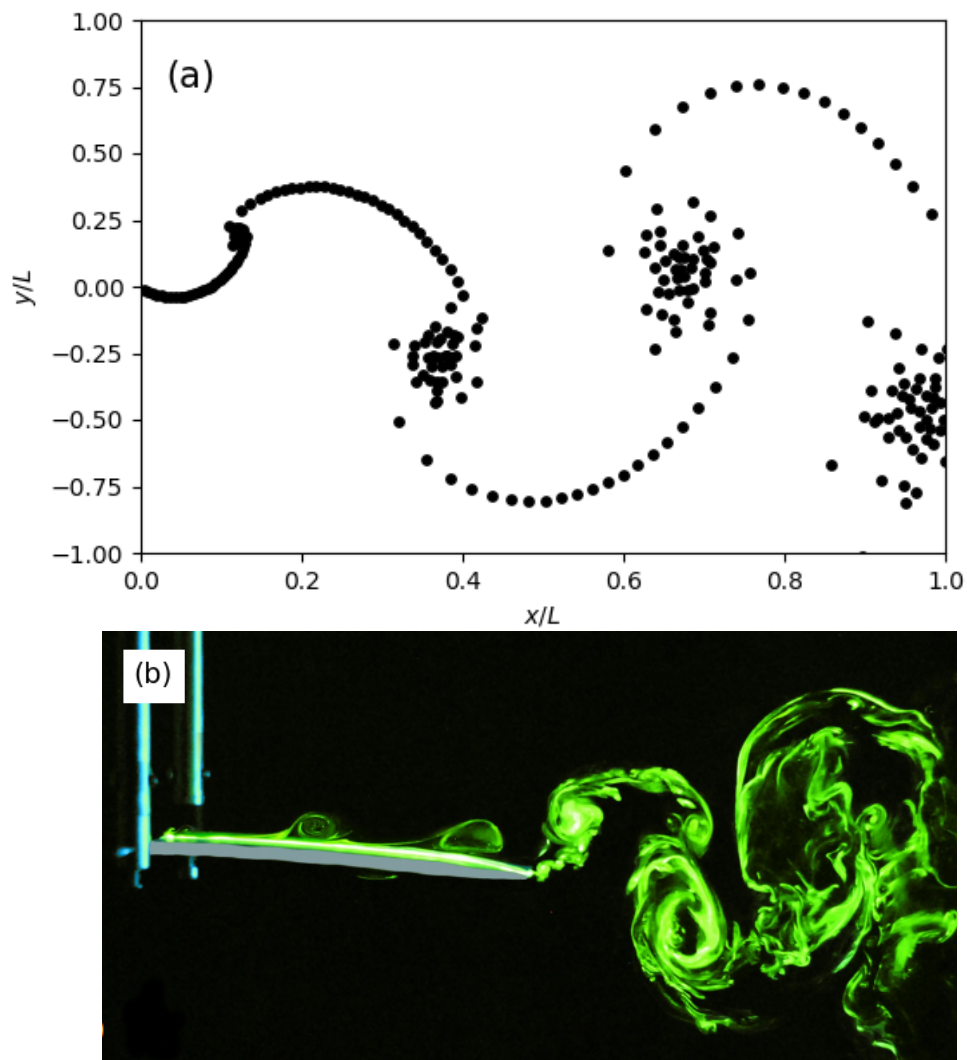


Figure 4.6: The wake following a heaving plate (not shown) of length, $L = 0.12$ m, frequency, $f = 0.8$ Hz, $U_\infty = 0.05$ m/s, given by (a) the present numerical model, plotted with the trailing edge of the cantilever at $x/L = 0$, after 200 time steps using vortices of core size 0.4 m ($\approx 3L$), and (b) an example of the experimental results presented in Paraz et al. [2014].

Chapter 5

Results

The focus of the results is upon the critical speed after which flutter of the flexible plate first occurs. It has been shown in Section 3.3.3 and by previous studies (e.g. Howell et al. [2009]) that the behaviour of the FSI system can be described by two control parameters, the non-dimensional flow speed \bar{U} and the mass ratio \bar{L} , and thus these parameters are used herein. The results of various simplifications to the model for the purposes of generating more versatile boundary-value models and the effects of varying the density of the fluid and length of the cantilever while maintaining a constant mass ratio are presented. In what follows \bar{U}_c^* and \bar{U}_c are the critical non-dimensional flow velocities at which instability occurs with and without a wake respectively.

5.1 Initial-value (Numerical Simulation) Results

To examine the effect of the jerk on the system and to judge the appropriateness of its omission in the two boundary-value models, simpler versions of the initial value model are assessed. First, the fully discretised wake is replaced by a single vortex and, second, the jerk term is removed from both, (a), the fully discretised wake and, (b), single-vortex models. Figures 5.1 (a) and (b) respectively show the variations of critical speed with mass ratio for these simplifications along with the results of the fully discretised wake (in (a) only) and the results in the complete absence of a wake. Overall these results show that (i) when jerk is omitted, the model over-predicts the critical speed, and (ii) when a single-vortex

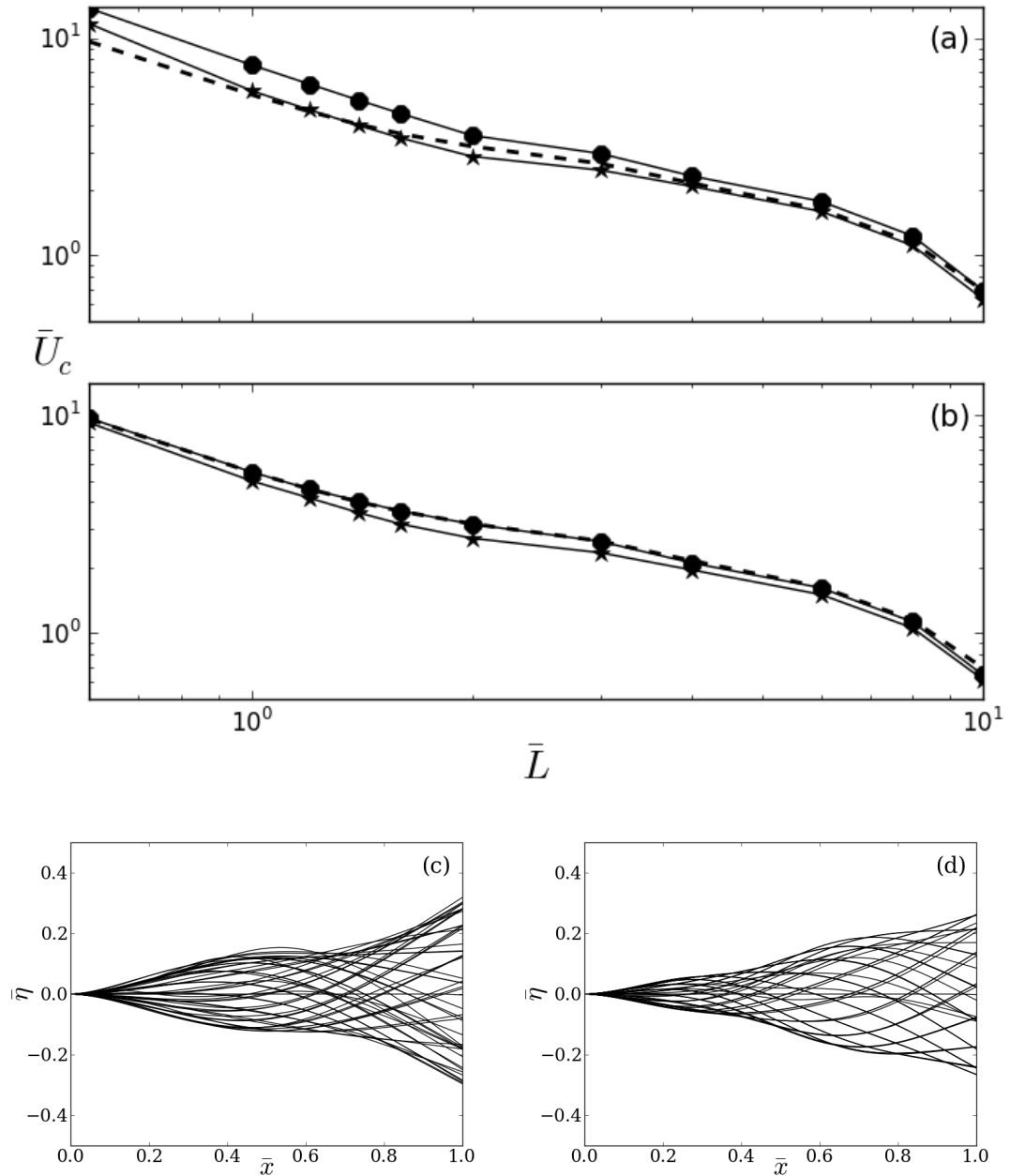


Figure 5.1: Variation of critical speed with mass ratio from the numerical simulation of the initial-value model for (a) fully discretised wake model, and (b) wake modelled by a single vortex. In each of these the no-wake, full (with jerk) and no-jerk results are shown by - - -, \star and \bullet respectively. (c) and (d) show the plate deflections over one oscillation for $\bar{L} = 1$ and 10 using the full numerical simulation model.

is used to represent the wake, the critical speed is under-predicted. However, it is evident that the single-vortex approximation, either with or without jerk, yields results that are very close to those when a full discretization of the wake is applied and certainly good enough for engineering predictions and the basis to develop a more versatile boundary-value solution for the system incorporating a

wake. Also shown in Figures 5.1 (a) and (b) is the swapping from the second to the third mode with increasing mass ratio at approximately $\bar{L} = 4$, indicated by the kink in each of the models at this point which is a feature similar though less pronounced than in equivalent results presented in the literature (for example Eloy et al. [2008] and Tang and Paidoussis [2007]). This kink is a result of the increase in mass ratio causing higher order modes to be excited above lower order modes, and leads to the system losing stability into those higher modes.

Figures 5.1 (c) and (d) show the instability-mode deformations at low and high mass ratios for which the effect of the wake is respectively stabilising and destabilising, a difference that also occurs in the models that omit the jerk term. At the lower mass ratio, flutter is dominated by second-mode content while at the higher mass ratio the flutter displays both second- and third-mode contributions; the former is described as a single-mode flutter, and the latter a modal-coalescence flutter. These findings agree with the results of Howell et al. [2009] and Tang and Paidoussis [2008]. It is also noted that as the mass ratio increases, yielding critical modes of higher order, the effect of the wake on the stability of the flexible plate becomes negligible.

5.2 Boundary-value Results

The predictions of instability-onset flow speed for the two boundary-value models developed in Section 3.3.2 are shown in Figure 5.2 (a) and compared to the model without a wake. Also included in this figure is the result from numerical simulations using a fully discretised wake and which also appeared as the solid line Figure 5.1 (a); this is the most complete model against which the more economical boundary-value results are assessed. It is seen that the first boundary-value model, developed using Equation 3.3.12a (where the strength of the wake is equal to the change in bound vorticity in time), yields results that compare well to that of the fully discretised wake for $\bar{L} \leq 2$. However as the mass ratio increases the first model shows that the wake has a very strong destabilising effect on the system, while the second model (where the strength of the wake is equal and opposite to the bound vorticity) gives results that are very similar to those when

the wake is absent across the range of mass ratios examined. The first model gives results which show the same stabilising-destabilising trend of the wake effect as the numerical simulation while the second model results show that the wake is mildly stabilising over a wider range of mass ratios. The same kink at $\bar{L} = 4$ is observed as in Figure 5.1 (a) and is again a result of mode-switching.

Figures 5.2 (b and c) and (d and e) show the mode shapes predicted by the first and second boundary-value models respectively and correspond to Figures 5.1 (c) and (d) obtained using full numerical simulation; very good agreement is seen between all three models for $\bar{L} = 1$, and between the first boundary-value model and the numerical simulation for $\bar{L} = 10$. The mode shape predicted by the second boundary-value model is noticeably different from that predicted by the numerical model, having wider and narrower oscillations over the first and second halves of the plate respectively. Thus, the first boundary-value model provides an accurate but simpler alternative for the prediction of the long-time response of the system when the mass ratio is approximately greater than unity. Both models 1 and 2 display the stabilising or destabilising effect of the wake on the plate depending on the mass ratio, though model 2 only begins to show the destabilising effect at $\bar{L} \geq 10$, and show the move from single-mode flutter to modal-coalescence with increasing mass ratio.

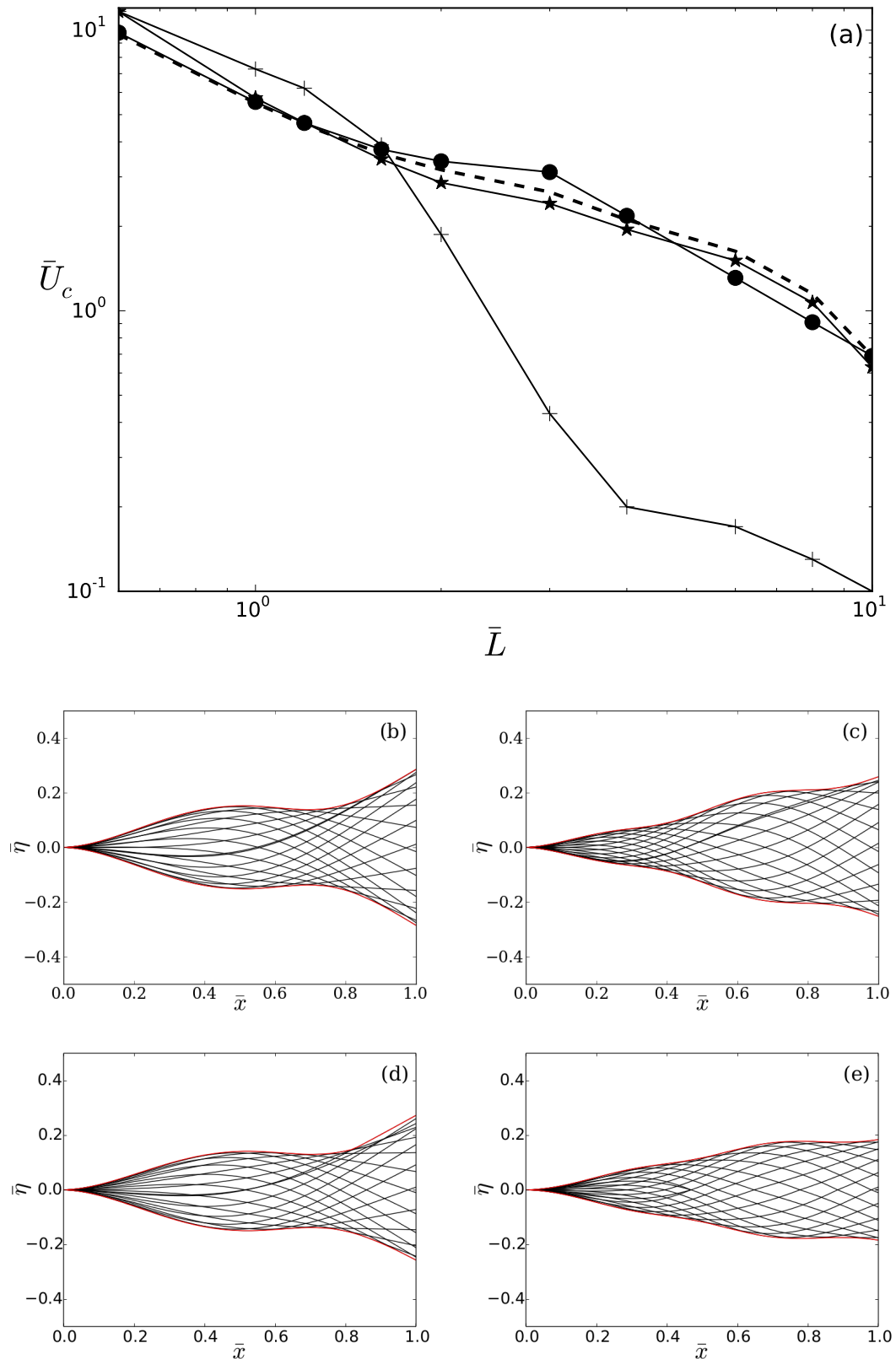


Figure 5.2: (a) A comparison of instability-onset flow speeds obtained from the two boundary-value models, + using Equation 3.3.12a (model 1) and • using Equation 3.3.12b (model 2), with the results of numerical simulations, * with a fully discretised wake and - - - with no wake. (b) and (c) show the plate deflections over one oscillation for $\bar{L} = 1$ and 10 using model 1 while (d) and (e) show the plate deflections over one oscillation for $\bar{L} = 1$ and 10 using model 2.

5.3 Fluid Density Variations

Although presented in non-dimensional form, all of the preceding results were obtained using air $\rho_f = 1.2 \text{ kg/m}^3$ as the fluid, as is the case in nearly all numerical studies found in the literature. The wake models developed in this thesis have also been used with fluids of much higher densities to assess whether the non-dimensionalisation of the system is complete. Figure 5.3 shows the variation of the non-dimensional instability-onset flow speed for five mass ratios, $\bar{L} = 0.6, 0.8, 1.0, 2.0,$ and 4.0 , in which the fluid-to-plate (ρ_f/ρ) density ratio is varied but the value of \bar{L} is held constant by varying the length of the plate. The figure shows the numerical-simulation (left panel) results from the fully discretized wake (including jerk) and the case where the wake is omitted, along with the predictions of the first boundary-value (right panel) model that was found to give a more accurate representation, both in terms of the shape of the oscillation envelope predicted, and in terms of the point of transition from stability to instability, of wake effects in the foregoing sub-section. There is no variation of critical speed when the wake is absent and this demonstrates that \bar{L} and \bar{U} fully describe the system. However, when the wake is included, the critical speed does depend upon the density ratio and the commensurate change in plate length; as the density ratio increases, the critical speed asymptotes to that when the wake is absent. In each case, dependence upon density ratio is found. In Figure 5.3, for $\bar{L} < 1$ the boundary-value model gives a very good approximation of the full numerical simulation results. For $\bar{L} \geq 1$ the boundary-value model demonstrates the same trend as the numerical simulation results, however with exaggerated values. Overall these results show that the wake effects - stabilising for low \bar{L} and destabilising for high \bar{L} - only apply for fluids with low density as compared with that of the structure.

Figures 5.4 (a-f) highlight the differences between the eigenvalue plots at low and high density ratio at $\bar{L} = 1, 2,$ and 4 . The solid and dashed lines represent the real and imaginary components of the eigenvalues, where the real component indicates the growth/decay rate in that particular mode, and the imaginary component shows the frequency of that mode for a given flow speed. When a solid line crosses 0 on the y-axis, it indicates that the system has lost stability in the mode which that solid line represents. Areas where a line splits into two distinct

lines indicate that the system can exist in multiple stable states at those points. The system will lose stability into whichever mode has a real part that becomes positive first. However, the dominant mode can change as the flow speed is increased. An example of this can be seen in Figure 5.4b, where the plate loses stability in the 4th mode; however, as the flow speed continues to increase the 2nd mode becomes more dominant because it is more unstable.

The peaks present in Figure 5.3 for $\bar{L} = 2$ and 4 are caused by the switching of the critical mode from the second mode to the fourth. Figures 5.4 (a-f) demonstrate this clearly, by displaying changes in the dominant mode as flow speed increases. This mode-switching is shown clearly in the centre and right columns of figures in Figure 5.4. The movement from single-mode flutter to modal-coalescence type flutter can be seen here also; in the left column of figures the instability shown is single-mode flutter as the line representing the second mode moves in to the positive region with no opposite, comparative motion of the other modes. However in the central column of figures coalescence can be clearly seen between the second and third modes, and in the right column of figures more complex coalescence between the second to fifth modes can be seen. This increasing combination of modes contributing to the critical mode at increasing mass ratio was demonstrated by Watanabe et al. [2002b] and Yamaguchi et al. [2000a]. Confidence can be had in the conclusions drawn about the peaks in Figure 5.3, as the change in critical mode is observed in Figure 5.4. This same change in mode is clear in the boundary-value model; however, can also be observed in the higher fidelity numerical model, though is less immediate owing to the time-dependent nature of this model.

The present results show that when the wake is modelled, the non-dimensionalised FSI system is no longer completely characterised by \bar{U} and \bar{L} because the fluid-to-solid density ratio ρ_f/ρ also becomes a control parameter. This control parameter arises as a result of the implicit inclusion of viscosity through the Kutta condition, leading to the appearance of the Strouhal number which is a dimensionless parameter which describes viscous oscillatory flow systems. The Strouhal number arises in combination with the density ratio as the components of the system

dynamic stiffness,

$$\text{Dynamic Stiffness} = \frac{\text{force}}{\text{system response}} = \frac{\rho_f U_\infty^2}{\rho (L\omega)^2} = \frac{\rho_f}{\rho} \left(\frac{1}{S_t} \right)^2. \quad (5.3.1)$$

Figure 5.3 shows that the density ratio has a greater effect on the system in the boundary-value model than in the full numerical model. This can be explained by the relationship shown in Equation 5.3.1. In the boundary-value model the frequency that vorticity is shed into the wake is locked to the oscillation frequency of the plate, resulting in $S_t \approx 1$, whereas in the numerical model the frequency of vortex shedding is unrelated to the plate's oscillation frequency. At low \bar{L} , where single-mode flutter is the main mechanism for instability, the plate oscillation and vortex shedding frequencies are more closely matched resulting in a larger effect of the density ratio on the system. At high \bar{L} , where the primary instability mechanism is modal-coalescence, the oscillation frequency of the plate is much higher than the shedding frequency resulting in a higher Strouhal number, hence greatly reducing the effect of the density ratio.

This separate density ratio does not appear in the non-dimensionalisation as the system equations are for an inviscid system, and the Kutta condition represents a viscous effect not accounted for in those equations. Though the models which exclude the wake also include a Kutta condition, the same dependence on density ratio is not seen as the Kutta condition only acts at the very edge of the simulation so the effect of this implicitly included viscosity is unable to propagate a change upstream of the trailing edge. The dependence on density or inertia ratio was also noted by Carpenter et al. [2001] in their study of compliant panels in viscous boundary layer flow.

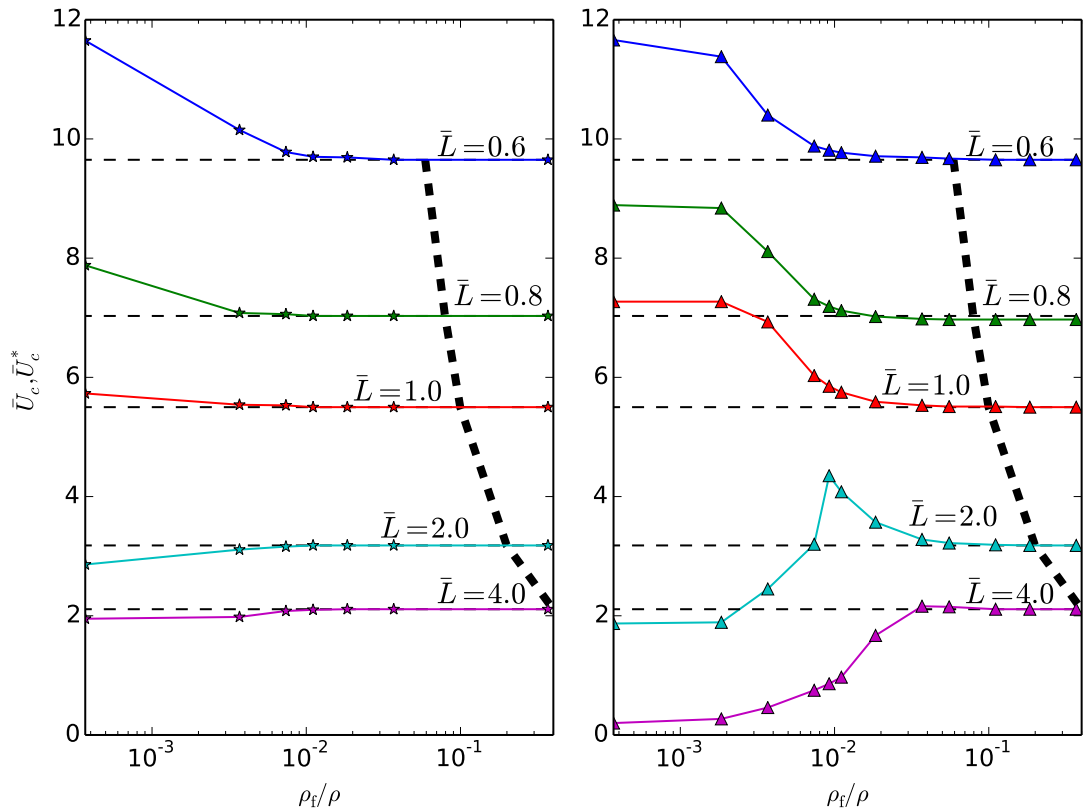


Figure 5.3: Variation of critical velocities with density ratio for constant \bar{L} values predicted by the numerical simulation (left) and boundary-value model (right). Each line is the critical velocity given by: numerical simulation with \star for a fully discretised wake and - - - for no wake, and Δ for the first boundary-value model with a wake (noting that with the wake effects suppressed, the boundary-value model gives the same results as the numerical simulation without a wake). The limit of the thin plate assumption where $L/h \geq 10$ is shown by the thick dashed line.

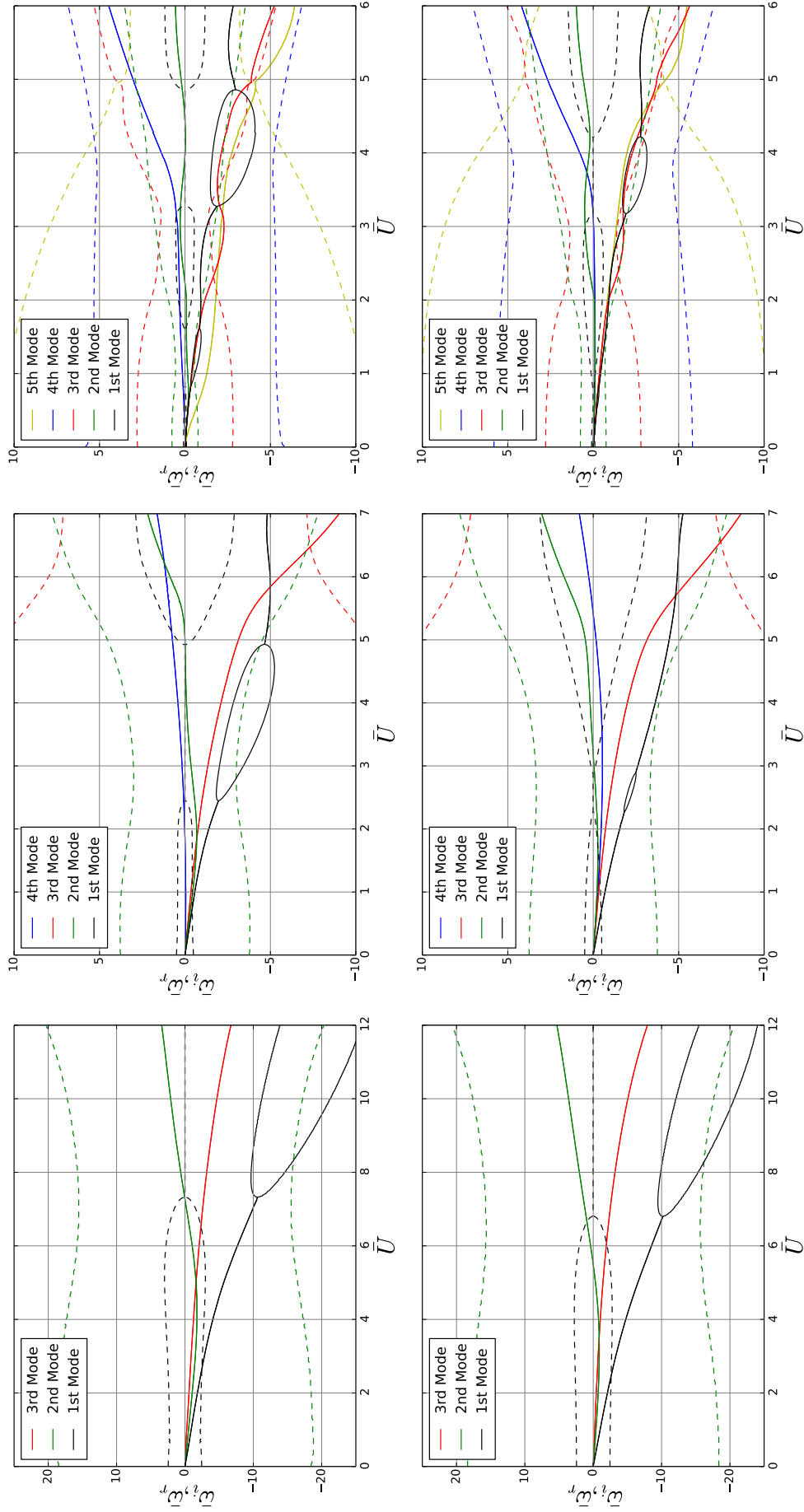


Figure 5.4: Eigenvalue plots at $\bar{L} = 1, 2,$ and 4 in the left, middle, and right columns respectively. Where the top and bottom rows are at $\rho_f/\rho = 4 \times 10^{-4}$ and 0.19 respectively (the x -limits of Figure 5.3). The solid and dashed lines represent the real and imaginary eigenvalue components respectively.

Chapter 6

Summary

A number of new theoretical and computational models have been developed to investigate the effect of the wake on the stability of a cantilevered flexible plate in an ideal flow. Numerical simulations when a fully discretised wake is modelled, show that the wake is stabilising or destabilising for low and high mass ratios respectively, as shown in the literature. The effect of the jerk (rate of change of acceleration) term is examined and its omission is shown to yield more stable predictions than those of the full system. Numerical simulations using just a single vortex to represent the wake are shown to yield predictions of instability onset that are in reasonable agreement with those of the faithfully represented distributed wake-vorticity model.

New models are developed which extend the state-space method developed in Howell et al. [2009] and Pitman and Lucey [2009] to solve the boundary-value problem when wake effects are incorporated. These new models show that it is possible to qualitatively capture the effect of a wake on a cantilevered plate using only a single wake vortex. In particular, it is shown that a wake-shedding model based upon the Kelvin condition yields values of critical velocity that are in very good agreement with full numerical simulations (after sufficient time has passed for transients to be convected away) when $\bar{L} \leq 2$ for a much lower computational cost. The switching from single-mode flutter to modal-coalescence flutter and to higher mode oscillation, which was demonstrated in the numerical model of Howell et al. [2009], is also seen in the boundary-value model.

Finally a new result is found concerning the non-dimensional characterisation

of the FSI system. A dependence on the mass ratio has been noted across the literature studying similar systems. However the results presented here demonstrate that an additional parameter is necessary to fully describe the system characteristics. In the absence of a wake, only two non-dimensional control parameters, the flow speed \bar{U} and the mass ratio \bar{L} , fully describe the system behaviour. But when wake effects are included the fluid-to-solid density ratio must additionally be accounted for. This ratio arises as a result of the viscosity implicitly included in the model owing to the Kutta condition. The present results show that, for any fixed mass ratio, when the fluid-to-solid density ratio is low the wake effects on stability described in the opening paragraph are found to hold. However, as the density ratio increases these wake effects decrease, and for fluids with high density compared to the plate the wake has a negligible effect. The density ratio must be considered when modelling the linear fluid-structure system and can be used to determine whether or not it is necessary to model the wake.

Part III

Non-Linear Model

Chapter 7

Theory

This section deals with the extension of the theory contained in the linear part of this thesis to account for large-amplitude deflections permitted by a non-linear model of the fluid and plate motions. Additionally a model capable of predicting flow separation from the surface of the plate and the non-linear motion of the wake vortices is developed. The system under consideration is shown in Figure 7.1.

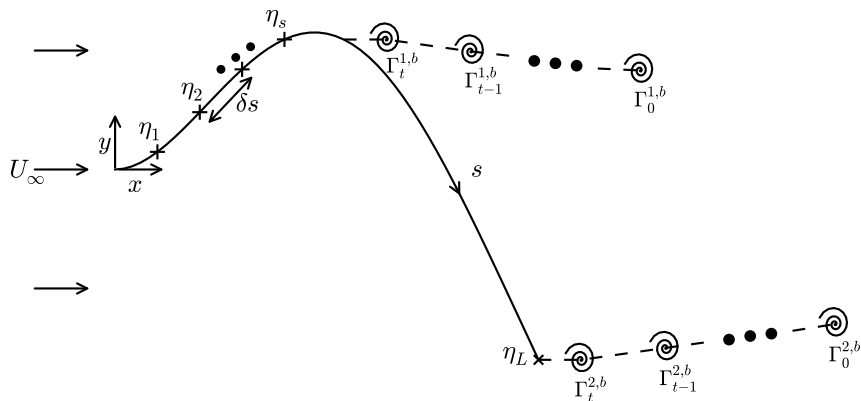


Figure 7.1: Schematic of the system studied and the approach taken to model separation.

7.1 Beam Model

The non-linear beam model is an extension of the linear model presented in Section 3.1. Again the plate is discretized into N mass points (shown in Figure

7.2) each separated by a distance $\delta s = L/N$ where L is the length of the plate and the mechanical properties of the plate are lumped at each mass point.

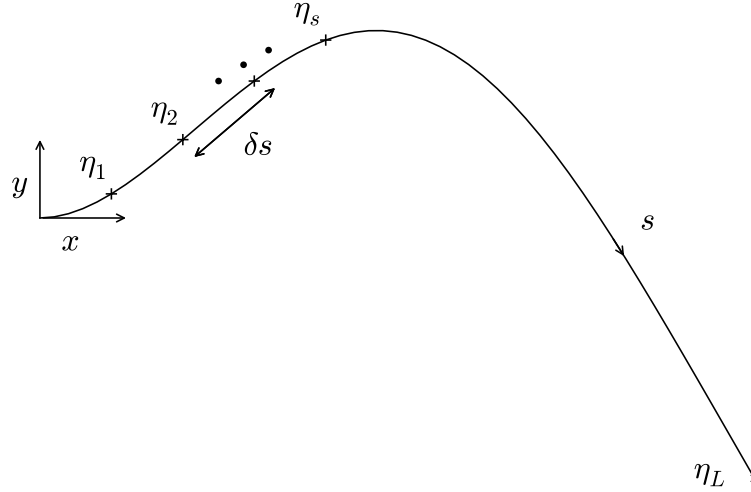


Figure 7.2: Beam discretization

The large amplitude deflection introduces additional forces in the form of induced tension due to centripetal forces. The full Euler-Bernoulli beam equation, derived in Tang and Dowell [2002] and Moretti [2003] following the method of Semler et al. [1994], includes these induced tension terms and is used to model the non-linear plate motion,

$$\begin{aligned}
 -\delta p = & \underbrace{\rho h \ddot{\eta}_s + \rho h \frac{\partial \eta}{\partial s} \int_0^s \left(\left(\frac{\partial^2 \eta}{\partial t \partial s} \right)^2 + \frac{\partial \eta}{\partial s} \frac{\partial^3 \eta}{\partial t^2 \partial s} \right) ds}_{\text{Induced tension I}} \\
 & - \underbrace{\rho h \frac{\partial^2 \eta}{\partial s^2} \int_s^L \int_0^s \left(\left(\frac{\partial^2 \eta}{\partial t \partial s} \right)^2 + \frac{\partial \eta}{\partial s} \frac{\partial^3 \eta}{\partial t^2 \partial s} \right) ds ds}_{\text{Induced tension II}} \\
 & + B \left[\frac{\partial^4 \eta}{\partial s^4} + \underbrace{\frac{\partial^4 \eta}{\partial s^4} \left(\frac{\partial \eta}{\partial s} \right)^2 + 4 \frac{\partial \eta}{\partial s} \frac{\partial^2 \eta}{\partial s^2} \frac{\partial^3 \eta}{\partial s^3} + \left(\frac{\partial^2 \eta}{\partial s^2} \right)^3}_{\text{Additional structural terms}} \right], \quad (7.1.1)
 \end{aligned}$$

where ρ , h , and B , are the plate density, thickness, and stiffness respectively. Additional damping terms have been ignored, as their effects will not form part of the study presented in this thesis. $\delta \eta$ is the vertical displacement between nodes, and s the longitudinal distance along the plate. The induced tension terms intro-

duce the inertia and coriolis-type terms created by large amplitude deflections, while the additional structural terms account for the large curvature experienced by the plate that is not present in the linear model. This equation is based upon the assumption that the plate is inextensible; thus, L and therefore δs are constant. As in the linear case the plate is assumed to be infinitely wide and is also assumed to be very thin, hence deforming by bending only, experiencing neither its own weight nor shear. In addition to solving for the vertical displacement of each node it is also necessary to calculate the horizontal displacement. This is achieved using the inextensibility condition from Semler et al. [1994],

$$V = -\frac{1}{2} \int_0^s \left(\frac{\partial \eta}{\partial s} \right)^2 ds, \quad (7.1.2)$$

where V is based on the curvature of the plate and is a modification to the horizontal node displacements of a flat plate (ξ_{flat}) such that,

$$\xi(t) = \xi_{\text{flat}} + V(t), \quad (7.1.3)$$

where ξ is the horizontal node displacement.

7.2 Fluid Model

The solution of the Laplace equation detailed below utilises a non-linear boundary-element flow solution similar to that developed in Lucey et al. [1997] and is an extension of the second-order linear boundary-element method detailed in the linear part of this thesis and Howell et al. [2009] so as to capture finite-amplitude effects.

7.2.1 Steady Flow Model

Owing to the large-amplitude oscillations permitted in this model the vortex panels are allowed to move with the plate in contrast to the linear model where the panels are held in the horizontal axis at $y = 0$. This layout is shown in Figure 7.3. The normal boundary/no-flux condition allows the calculation of the

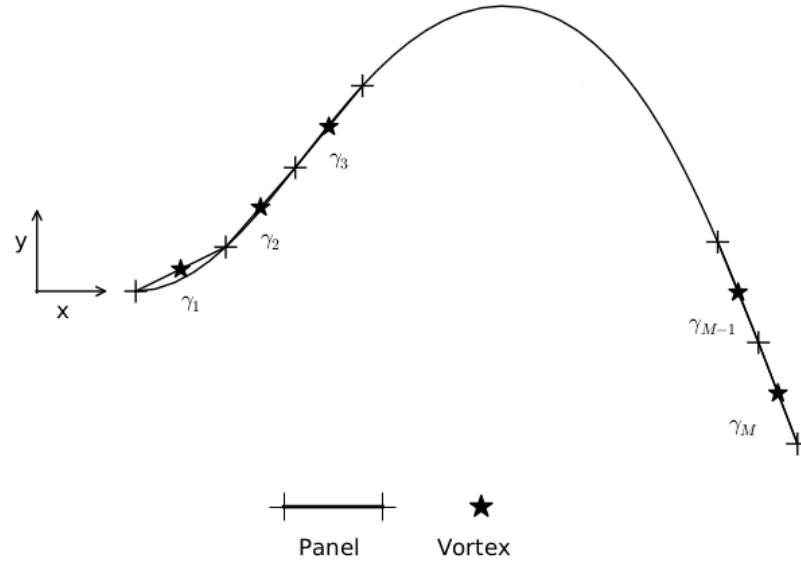


Figure 7.3: Boundary-element panel arrangement for the non-linear plate.

non-linear distributed bound vortex strengths and may be written as,

$$[\mathbf{I}^{\mathbf{N}}]\{\gamma\} = \underline{v}_p \cdot \underline{n} - \underline{U}_\infty \cdot \underline{n} - \underline{u}^b \cdot \underline{n}, \quad (7.2.1)$$

where \underline{n} is a vector normal to a surface which has the velocity $\underline{v}_p = \dot{\xi}\underline{i} + \dot{\eta}\underline{j}$, $\dot{\xi}$ and $\dot{\eta}$ are the horizontal and vertical velocity components of the surface respectively, \underline{u}^b is the wake-induced velocity vector, $[\mathbf{I}^{\mathbf{N}}]$ is the matrix of normal influence coefficients, and $\{\gamma\}$ is a vector of zero-order vortex strengths. As the panels can now move the influence coefficients must be recalculated at every time step. One further difference from the linear model is that as a result of flow separation owing to the large-amplitude deflections the Kutta condition may not hold (Taneda [1968], Katz and Plotkin [2010]) as full circulation is not guaranteed at every time step. This condition is used in conjunction with the Kutta condition proposed by Howell [2006] given in Equation 3.2.8 and restated here,

$$\gamma_{\text{TE}} + \lambda_{\text{TE}} \frac{s}{2} = 0, \quad (7.2.2)$$

such that the fully assembled model switches between these two conditions depending on whether separation occurs and is applied through the normal influence coefficient matrix as in the linear model. The physical implications of these

boundary conditions is primarily that in the latter, a stagnation point is enforced at the trailing edge. This is not the case in the former.

7.2.2 Wake Model

The wake is modelled using the discrete vortex method described in section 3.2.2. However, as a result of the non-linear motion of the plate the assumptions made with regard to the wake in the linear model are no longer valid. The wake vortices in this model are unrestrained and are freely able to influence each other and influence/be influenced by the plate. The position of a wake vortex, i , is given by,

$$x_i^{b,t+1} = x_i^{b,t} + (U_\infty + u_{bi}^{Tb} + u_{pi}^T) \delta t, \quad (7.2.3)$$

$$y_i^{b,t+1} = y_i^{b,t} + (u_{bi}^{Nb} + u_{pi}^N) \delta t. \quad (7.2.4)$$

Where x_i and y_i are the coordinates of wake vortex i , u^{Tb} and u^{Nb} are the wake-induced velocity at the position of vortex i in the x - and y - direction given by Equations 3.2.13a and 3.2.13b respectively, and the position of the wake vortices is calculated using a first-order Euler scheme. The u^T and u^N terms are the plate-induced velocity at point i and are determined using the lumped plate singularity strengths.

Owing to the large-amplitude oscillations allowed by the non-linear plate model, the flow may separate from the plate forming a free shear layer as observed in the experiments of Taneda [1968] and Zhang et al. [2000]. This will be represented in this model by the inclusion of a shear-layer vorticity separating from upstream of the plate trailing edge as illustrated in Figure 7.3.1. As flow separation is an explicit viscous effect the Kelvin condition, which was used to calculate the strength of the wake vortices in the linear model, is no longer guaranteed to apply at every time step. Thus when the flow is judged to be separating from the plate, circulation in the system is assumed to no longer be constant, the Kelvin condition is ignored, and two free-shear layers are formed.

Figure 7.4 shows flow separation as a pair of free-shear layers, the first leaving at the trailing edge and the second from the point of separation. The strength

of a vortex released as part of a free-shear layer is determined using the local circulation given by,

$$\gamma_{\text{shear}} = U_u - U_l, \quad (7.2.5)$$

where U_u and U_l are the flow velocities directly above and below the shear layer respectively. The length of shear layer generated within each time step is given by,

$$L_{\text{shear}} = \frac{1}{2}(U_u + U_l)\delta t, \quad (7.2.6)$$

and hence the vorticity shed into the shear layer at each time step is,

$$\begin{aligned} \Gamma_{\text{shear}} &= \gamma_{\text{shear}} \frac{1}{2}(U_u + U_l)\delta t, \\ &= \frac{1}{2}(U_u^2 - U_l^2)\delta t. \end{aligned} \quad (7.2.7)$$

The flow speed U_u is given by $U_u = U_\infty + \Delta U_{\text{local}}$, where ΔU_{local} is the local perturbation velocity. It is assumed that there is zero flow speed within the separation zone, and as a result of this assumption the wake does not exert influence on the side of the plate experiencing separation past the point of separation. The same process is applied to find the vorticity shed into the free-shear layer which forms at the trailing edge. As in the linear model the wake influences the plate through the no-flux condition written as Equation 7.2.1 where the total velocity induced at a point on the plate by the wake is given by,

$$\underline{u}_p^b = u^{Tb} \underline{i} + u^{Nb} \underline{j}, \quad (7.2.8)$$

as in the linear model.

7.2.3 Unsteady Flow Model

The pressure acting on the plate is calculated using the unsteady Bernoulli equation as in the linear model (Equation 3.2.16), and yields expressions for the pressure acting on the upper and lower surfaces of the plate (shown in Appendix B.3).

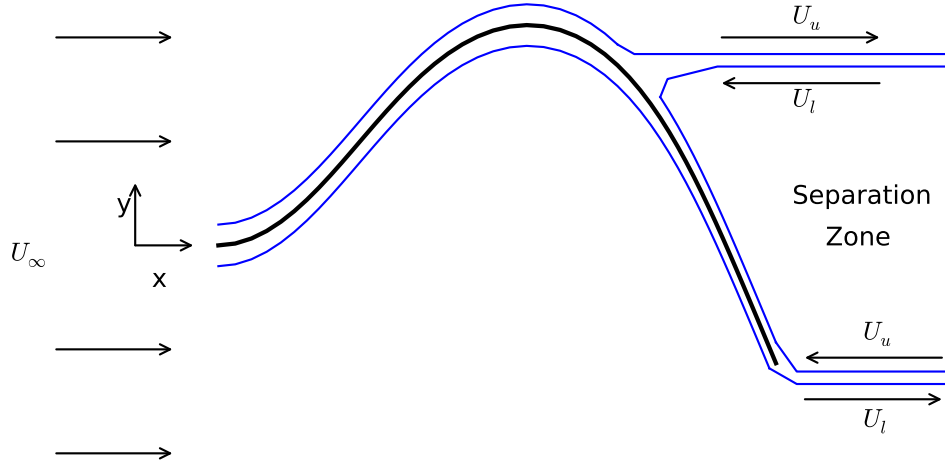


Figure 7.4: Representation of the free-shear layers that form at the point of separation and from the plate trailing edge.

Taking the difference between these two pressures yields the pressure difference acting across the plate,

$$\begin{aligned} \delta p|_{xp} &= p|_{\text{upper}} - p|_{\text{lower}}, \\ &= -2\rho_f u^{T'} (U_\infty \cos \theta + u^{T'b} \cos \theta + u^{N'b} \sin \theta) - \rho_f \frac{\partial \phi}{\partial t}|_{xp}, \end{aligned} \quad (7.2.9)$$

where $p|_{\text{upper}}$ and $p|_{\text{lower}}$ are given by Equations B.3.5a and B.3.5b respectively. The tangential and unsteady perturbation velocities are given by (Lucey et al. [1997]),

$$u^{T'} = [\mathbf{I}^T] \{\gamma\}, \quad (7.2.10a)$$

$$\frac{\partial \phi}{\partial t} = [\mathbf{I}^\phi] \{\dot{\gamma}\} + [\dot{\mathbf{I}}^\phi] \{\gamma\}, \quad (7.2.10b)$$

where $[\mathbf{I}^T]$ and $[\mathbf{I}^\phi]$ are the tangential and perturbation-potential influence coefficients. As the panels are now able to move care must be taken when calculating the polarity of the angles involved in determining the values of $[\mathbf{I}^\phi]$. The polarity of the off-diagonal terms in the $[\mathbf{I}^T]$ must also be modified in relation to the sum of the beam vorticity. The strength of the vortices, $\{\gamma\}$, and the rate of change

of vorticity, $\{\dot{\gamma}\}$, are found using Equation 7.2.1 and are given by,

$$\{\gamma\} = [\mathbf{I}^{\mathbf{N}}]^{-1} \{ (U_{\infty} - \dot{\xi} + u^{T_b}) \sin \theta + (\dot{\eta} - u^{N_b}) \cos \theta \} \quad (7.2.11)$$

$$\begin{aligned} \{\dot{\gamma}\} &= [\mathbf{I}^{\mathbf{N}}]^{-1} \{ (\dot{u}^{T_b} + u^{N_b} \dot{\theta} - \ddot{\xi} - \dot{\eta} \dot{\theta}) \sin \theta + (\ddot{\eta} + U_{\infty} \dot{\theta} + u^{T_b} \dot{\theta} - \dot{u}^{N_b} - \dot{\xi} \dot{\theta}) \cos \theta \} \\ &\quad + [\mathbf{I}^{\mathbf{N}}]^{-1} [\dot{\mathbf{I}}^{\mathbf{N}}]^{-1} \{\gamma\}, \end{aligned} \quad (7.2.12)$$

derived in Appendix B.2, where θ is the panel angle relative to the horizontal.

7.3 Computational Model Assembly

The solid and fluid models are now combined to produce a model capable of capturing the non-linear dynamics of a cantilevered plate undergoing large-amplitude oscillations in inviscid axial flow including the effects of separation. Combining Equations 7.1.1 and 7.2.9 yields the coupled system equation which can be rearranged to calculate the plate node acceleration at time t ,

$$\rho h [\mathbf{I}] \ddot{\eta} + p'' = -\delta p|_{\text{xp}} \quad (7.3.1)$$

$$\left[\rho h [\mathbf{I}] - [\mathbf{B}] \cos \theta \right] \ddot{\eta} = -(\delta p'|_{\text{xp}} + p_{\text{plate}}). \quad (7.3.2)$$

where $\delta p''$ is a combination of the induced tension and flexural rigidity terms in Equation 7.1.1 shown by Equation B.1.2a in Appendix B.1. Equation 7.3.2 is then solved using a semi-implicit Crank-Nicholson type method of solution detailed in Lucey and Carpenter [1992], which solves first for plate acceleration at the next time step and then follows by trapezoidal integration to determine the velocities and displacements using second-order Euler approximations,

$$\{\dot{\eta}\}^{t+\delta t} = \{\dot{\eta}\}^t + \frac{\{\ddot{\eta}\}^{t+\delta t} + \{\ddot{\eta}\}^t}{2} \delta t + \frac{\{\dot{\eta}\}^{t+\delta t} + \{\dot{\eta}\}^t}{2} \frac{\delta t^2}{2}, \quad (7.3.3a)$$

$$\{\eta\}^{t+\delta t} = \{\eta\}^t + \frac{\{\dot{\eta}\}^{t+\delta t} + \{\dot{\eta}\}^t}{2} \delta t + \frac{\{\ddot{\eta}\}^{t+\delta t} + \{\ddot{\eta}\}^t}{2} \frac{\delta t^2}{2}. \quad (7.3.3b)$$

The jerk terms are given by the change in acceleration between time steps.

7.3.1 Separation

Separation from the plate surface is adjudged to occur downstream of the point at which an adverse pressure gradient first occurs which exceeds a threshold value. We can set this threshold value of pressure gradient through a chosen value of a coefficient P_{thresh} that is a multiplicative factor on a characteristic pressure gradient defined by the dynamic pressure. By varying this threshold value we can investigate the effect of different levels of flow separation on the FSI; for example, at high P_{thresh} the flow separates at the trailing edge whereas for very low values it separates at an upstream location close to where the flow first enters an adverse pressure-gradient region. The effect of varying the value of P_{thresh} will be investigated because a suitable value can only otherwise be determined empirically (Leonard [1980], Sarpkaya [1989]). The results will be compared to those found in the literature, for example Shelley et al. [2005], to determine an appropriate threshold value. The assessment as to whether the flow is separating is made at each time step based on the pressure gradient present at that time step.

When the plate is experiencing flow separation wake vortices are released in pairs at a distance of $U_{\infty}\delta t$ from the separation point and the trailing edge. The strengths of the shed vortices are given by Equation 7.2.7 while the plate is undergoing separation, or otherwise using Equation 3.3.5.

The surface pressures, $p|_{\text{upper}}$ and $p|_{\text{lower}}$, are calculated independently and assessed to determine whether either meets the criteria for separation at each time step. The pressure acting on the surface experiencing separation is then modified by enforcing that the pressure on that surface after the separation point be equal to the pressure at the separation point. For example, if the flow were to separate from the upper plate surface,

$$p_{\text{upper}}|_{n>\delta} = p_{\text{upper}}|_{\delta}, \quad (7.3.4)$$

where δ is the point of separation, this is applied to the entire separation zone. This modified pressure is then used to calculate the pressure difference across the plate. It should be noted that a limitation of this model is that once the flow

has separated it will be unable to reattach to the plate surface at that time step. This limitation is judged to be unimportant for FSI modes of low order, expected in the behaviour at low \bar{L} . For higher-order FSI modes such reattachment may occur but modelling this is beyond the scope of the current study, but could be the subject of further work.

7.3.2 System Non-dimensionalisation

The method of Crighton and Oswell [1991] can be applied to Equation 7.3.1 to yield the non-dimensional control parameters of the non-linear system. Choosing the same relationships as in Section 3.3.3,

$$\eta = \bar{\eta}L_r, \quad s = \bar{s}L_r, \quad t = \bar{t}T_r, \quad U_\infty = \bar{U}\frac{L_r}{T_r}, \quad \phi = \bar{\phi}\frac{L_r^2}{T_r}, \quad u^{T'} = \bar{u}^{T'}\frac{L_r}{T_r},$$

where T_r and L_r are again reference time and length with units of seconds and metres respectively. Substituting these into the expanded form of Equation 7.3.1 yields,

$$\begin{aligned} & \rho h \frac{1}{\rho_f L_r} \left(\frac{\delta^2 \bar{\eta}}{\delta \bar{t}^2} + \frac{\delta \bar{\eta}}{\delta \bar{s}} f_1 - \frac{\delta^2 \bar{\eta}}{\delta \bar{s}^2} f_2 \right) + B \frac{T_r^2}{\rho_f L_r^5} f_3 \\ & = 2\bar{u}^{T'} (\bar{U} + \bar{u}^{T_b}) + \frac{\delta \bar{\phi}}{\delta \bar{t}}. \end{aligned} \quad (7.3.5)$$

Where f_1 , f_2 , and f_3 are functions of η -derivatives and defined as,

$$f_1 = \int_0^{\bar{s}} \left(\left(\frac{\delta^2 \bar{\eta}}{\delta \bar{t} \delta \bar{s}} \right)^2 + \frac{\delta \bar{\eta}}{\delta \bar{s}} \frac{\delta^3 \bar{\eta}}{\delta \bar{s} \delta \bar{t}^2} \right) d\bar{s}, \quad (7.3.6a)$$

$$f_2 = \int_{\bar{s}}^{\bar{L}} \int_0^{\bar{s}} \left(\left(\frac{\delta^2 \bar{\eta}}{\delta \bar{t} \delta \bar{s}} \right)^2 + \frac{\delta \bar{\eta}}{\delta \bar{s}} \frac{\delta^3 \bar{\eta}}{\delta \bar{s} \delta \bar{t}^2} \right) d\bar{s} d\bar{s}, \quad (7.3.6b)$$

$$f_3 = \frac{\delta^4 \bar{\eta}}{\delta \bar{s}^4} \left(1 + \left(\frac{\delta \bar{\eta}}{\delta \bar{s}} \right)^2 \right) + 4 \frac{\delta \bar{\eta}}{\delta \bar{s}} \frac{\delta^2 \bar{\eta}}{\delta \bar{s}^2} \frac{\delta^3 \bar{\eta}}{\delta \bar{s}^3} + \left(\frac{\delta^2 \bar{\eta}}{\delta \bar{s}^2} \right)^3. \quad (7.3.6c)$$

As in the linear non-dimensional scheme, choosing,

$$L_r = \frac{\rho h}{\rho_f}, \quad T_r = \frac{(\rho h)^{5/2}}{\rho_f^2 B^{1/2}},$$

Equation 7.3.5 becomes,

$$\frac{\delta^2 \bar{\eta}}{\delta \bar{t}^2} + \frac{\delta \bar{\eta}}{\delta \bar{s}} f_1 - \frac{\delta^2 \bar{\eta}}{\delta \bar{s}^2} f_2 + f_3 = 2\bar{u}^{T'} (\bar{U} + \bar{u}^{T_b}) + \frac{\delta \bar{\phi}}{\delta \bar{t}}. \quad (7.3.7)$$

The system response is again governed by \bar{U} and \bar{L} as in the linear model where,

$$\bar{U} = U_\infty \frac{(\rho h)^{3/2}}{\rho_f B^{1/2}}, \quad \bar{L} = \frac{\rho_f L}{\rho h}. \quad (7.3.8)$$

Finally, P_{thresh} is nondimensionalised by the dynamic pressure $\rho_f U_\infty^2$ divided by the plate length, L .

Chapter 8

Validation

This section presents the validation of the non-linear models developed in the previous section, and their combination into the full computational model. Unless otherwise stated $\bar{L} = 1$, $\bar{U} = 5.5$ and except in the *in vacuo* case the fluid density is taken to be 1.2 kg/m^3 . The wake model remains unchanged from that presented in the linear model and has already been validated. Only the initial value solution can be used to model the non-linear problem and so all results are in the time domain. Tang and Dowell [2002] show the non-linear strain and kinetic energy are given by Equations 8.0.1a and 8.0.1b respectively.

$$E_s = \frac{1}{2}B \int_0^L \left(\frac{\partial^2 \eta}{\partial s^2} \right)^2 \left/ \left[1 - \left(\frac{\partial \eta}{\partial x} \right)^2 \right] dx, \quad (8.0.1a)$$

$$E_k = \frac{1}{2}\rho h \int_0^L (\dot{\xi}^2 + \dot{\eta}^2) dx. \quad (8.0.1b)$$

8.1 Plate Model

The first step to validate the plate model is achieved by reducing the amplitude of oscillation to that used in the linear model, and comparing the *in-vacuo* period of oscillation to the linear model. The mechanical properties of the plate used are: $E = 7 \times 10^7 \text{ N/m}^2$, $\rho = 2710 \text{ kg/m}^3$, $\nu = 0.3$, $h = 5 \times 10^{-4} \text{ m}$ and $L = 1.355 \text{ m}$. The plate is initially deflected into an arbitrary shape before being released and allowed to oscillate freely. Figure 8.1 shows the result of applying each of the first four eigenmode shapes to the non-linear plate model and allowing the plate to oscillate freely. It is shown that the beam experiences stable, neutral

Table 8.1: Simulated oscillation frequencies at various levels of discretization.

Mode	Theoretical Period (/s)	Simulation period (/s)		
		50 nodes	100 nodes	200 nodes
1	133.363	132.468	133.077	133.343
2	21.279	21.087	21.153	21.270
3	7.541	7.67	7.545	7.541
4	3.878	3.97	3.909	3.874

oscillations, and fully maintains its initial shape. The perfect anti-phase of strain and kinetic energy is also shown, and the results are very similar to those shown in the validation of the linear model (Figure 4.1). In each case the strain and kinetic energies in the plate are calculated at each time step using Equations 8.0.1a and 8.0.1b respectively. The total energy (E_t) is given by the sum of the strain and kinetic energies, and the energies are non-dimensionalised by the initial energy in the plate ($E_t^{t=0}$). The progress of a single node was tracked over several oscillations enabling the calculation of the period. Table 8.1 shows the results of this analysis at increasing levels of discretization. It was found that a discretization of 50 nodes gave very good agreement between the theoretically and numerically determined oscillation period. The results are also in excellent agreement with the results of the same analysis of the linear plate model (Table 4.1). The effect of increasing the initial deflection from linear to non-linear amplitudes on the mode shape and tip deflection shown in Figure 8.2 (d), (e) and (f) respectively are compared with the corresponding results from Elliot et al. [2010] shown in Figures 8.2 (a), (b), and (c). The mode shapes and tip deflections are found to be very similar between the present model and that presented by Elliot et al. and a further comparison is made in Figure 8.3 which shows the ratio of the numerical results of the non-linear model to the theoretical frequency presented in the linear theory. It is shown that the flutter frequency of the non-linear model converges to that of the linear theory as the amplitude of oscillation approaches a linear regime. Good agreement between the current *in-vacuo* plate model and that presented in Elliot et al. [2010] is found, and convergence to the linear result is also shown lending further confidence to the validity of the plate model.

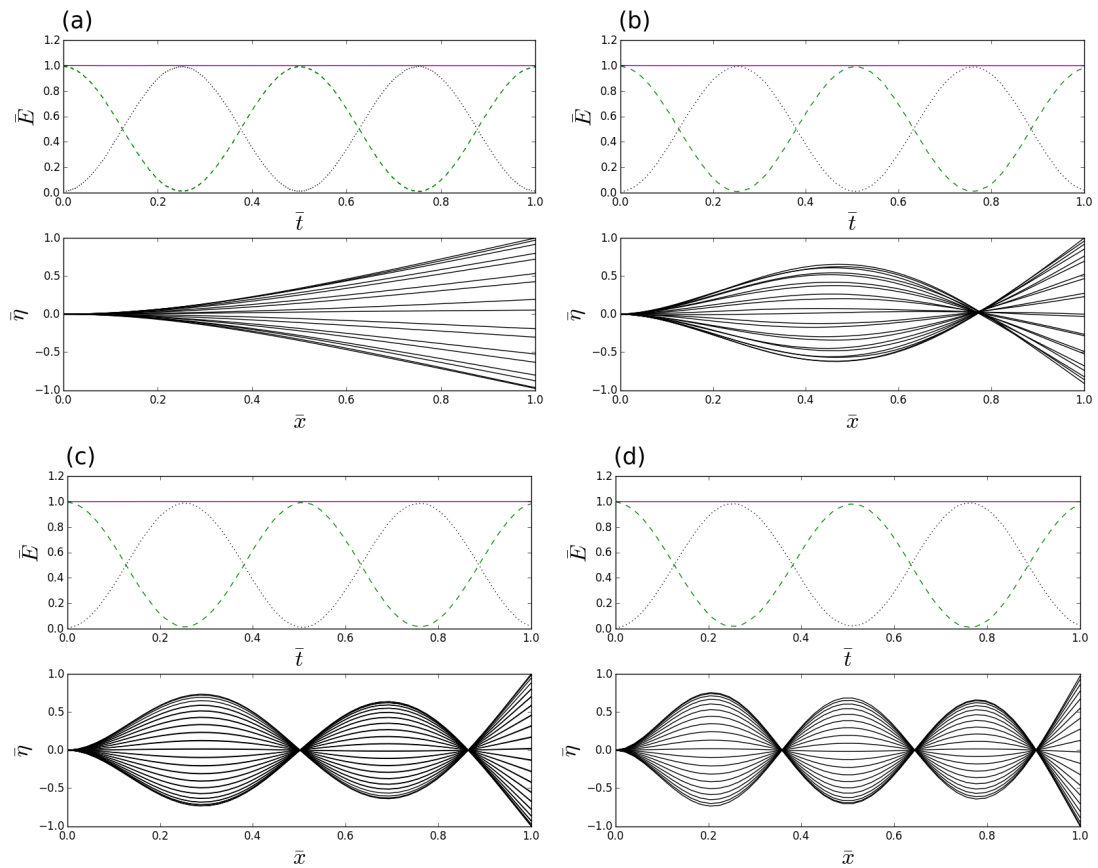


Figure 8.1: The cantilever model in the first four modes and their associated energies during one oscillation using 200 nodes. (a), (b), (c), and (d) show the first through fourth modes respectively. The total, strain, and kinetic energies are the solid, dashed, and dotted lines respectively in each subfigure.

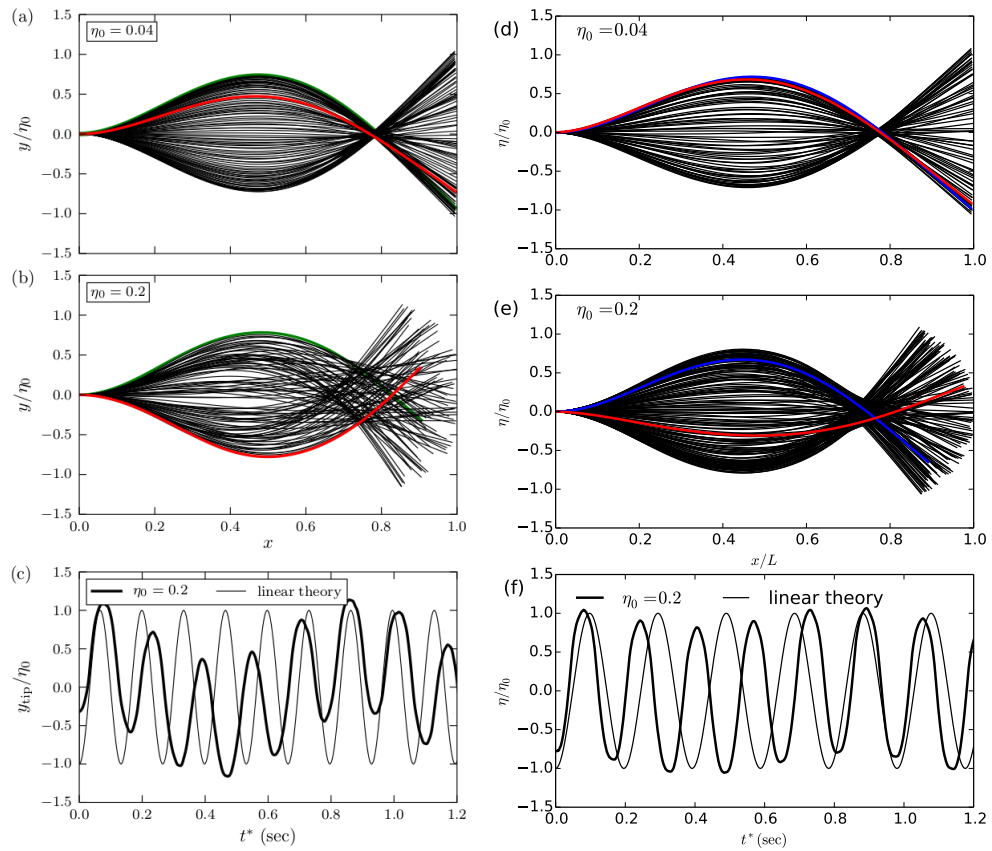


Figure 8.2: Effect of amplitude on mode shape and tip deflection in the current model (d), (e), and (f) compared to the equivalent figures in Elliot et al. [2010] reproduced in (a), (b), and (c).

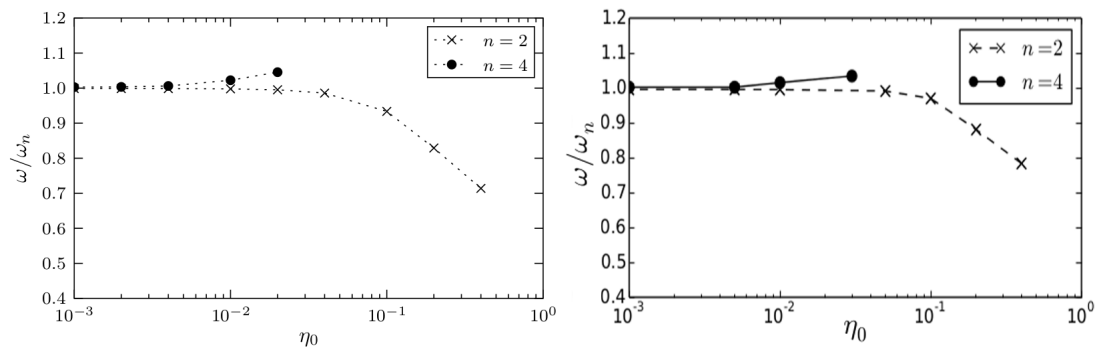


Figure 8.3: Convergence of model frequency, ω , to the linear theory at small amplitudes compared to that presented in Elliot et al. [2010] (left).

8.2 Fluid Model

The variation of the total pressure difference arising from linear to non-linear amplitudes is shown in Figures 8.4 (a-d). In each case the plate is deflected into the second mode shape predicted by the linear model and adjusted to account for large amplitude deflections, before being released and allowed to oscillate freely between $\bar{t} = 0 \rightarrow 1$. The non-linear pressure model recovers those pressures generated by the linear model as linear amplitudes are approached. It can be seen that the linear pressure model over-predicts the pressure at higher amplitudes, and that the pressure models grow out of phase as the amplitude increases. This was also noted by Lucey et al. [1997] in their study of non-linear flexible walls.

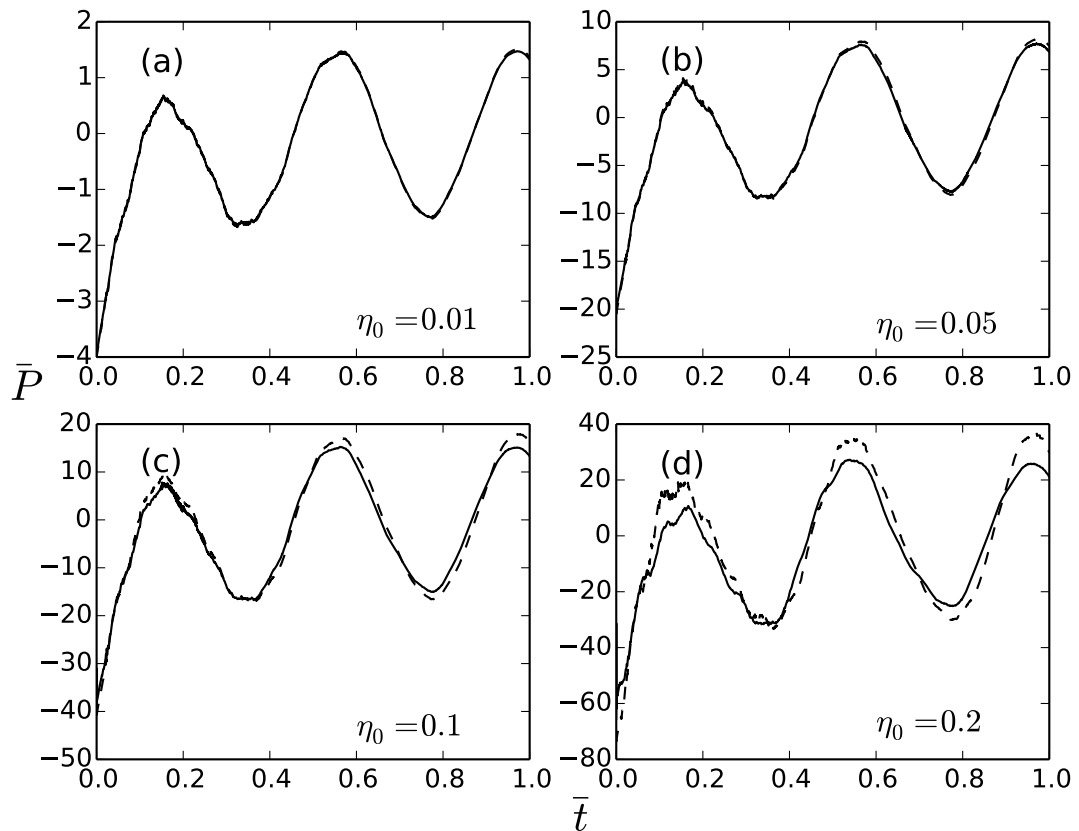


Figure 8.4: The pressure difference across the plate given by the present model (—) and the linear theory (- -) at increasing amplitude.

8.3 Unsteady Model

The plate and fluid models are first combined to produce a model of the unsteady system without a wake. Figure 8.5 shows the variations of plate deflection, tip deflection, and plate energy in time at two different flow speeds. In the top row of figures $\bar{U} = 5.50$, the critical velocity obtained for the no-wake case in the linear model, and in the bottom row $\bar{U} = 7.16$, which is approximately 30% above the linear critical velocity. In each case the plate is given the same initial deflection, $\eta_0 = 0.05$, and allowed to oscillate freely until a steady state is reached. The plate deflection and energy at the linear critical velocity compare very well with the linear model at this flow speed shown in Figure 4.5b. The figures representing the higher flow speed demonstrate that the model allows the amplitude of oscillation to grow in time, driven by the higher flow speed, until saturation occurs and the plate settles in to limit-cycle oscillations at approximately $\bar{T} = 2.5$. This is shown clearly in the tip deflection and plate energy plots. Further increasing the flow velocity yields higher deflections up until the limit of chaotic oscillations. Figure 8.6 shows the maximum tip deflection for a range of flow speeds above the linear critical velocity using both the non-linear and linear fluid models. It is seen that the non-linear model converges to the linear result at flow speeds close to the limit of linear instability. It is noted that even beyond the limits of the linear model the results yielded by the linear model are similar to those produced by the fully non-linear model. Beyond the maximum flow velocity shown the plate enters chaotic oscillations wherein the plate moves between several stable states, this region is not investigated in the current study. This transition to chaos was studied by Alben and Shelley [2008], who found that the chaotic nature of the oscillations above a certain flow velocity resulted in a wide range of excited frequencies rather than the one dominant frequency seen at lower flow velocities, and intermittent high-drag events when the plate would “snap”.

8.4 Wake Model

The wake model is broadly unchanged from the linear model, thus the validation presented in Section 4.4 still serves to validate the wake model for the case where

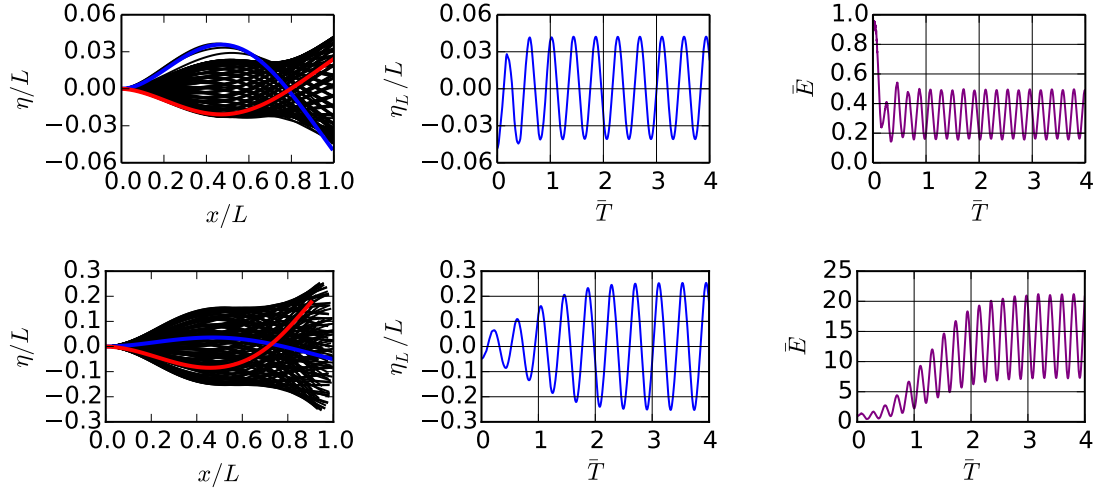


Figure 8.5: The plate deflection (left), tip deflection (middle), and energy (right) in time at $\bar{U} = 5.50$ (top) and $\bar{U} = 7.16$. The initial and final deflections are shown by the blue and red lines in the left column of figures respectively.

separation is not present. Further validation was performed by comparing the form of the wake presented by Alben and Shelley [2008] with the results produced by the current model. The properties of the plate were chosen to match the control parameters used by Alben and Shelley [2008], who used non-dimensional mass and rigidity given by,

$$R_1 = \frac{\rho_s}{\rho_f' L}, \quad (8.4.1a)$$

$$R_2 = \frac{B}{\rho_f' U_\infty^2 L^3}, \quad (8.4.1b)$$

respectively. Where ρ_s is the mass per unit length of the plate, and ρ_f' is the mass per area of the fluid. Results of simulations and the corresponding figures adapted from Alben and Shelley [2008] are shown in Figure 8.7. Figures (c) and (d) show the results generated by the current model after 400 time steps at $\bar{U} = 7.58$ and 7.77 respectively, and (a) and (b) are the respective results presented by Alben and Shelley. The current wake model takes a very similar form to that of Alben and Shelley in the case where a wake forms at the trailing edge of a plate undergoing large-amplitude oscillations.

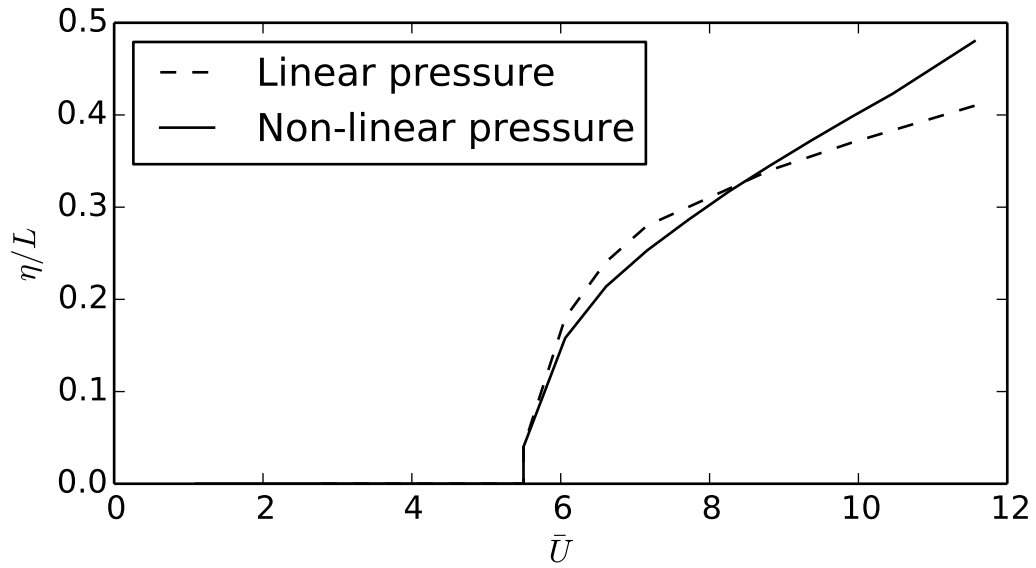


Figure 8.6: Tip deflections at increasing flow speed produced by the linear and non-linear fluid models without a wake.

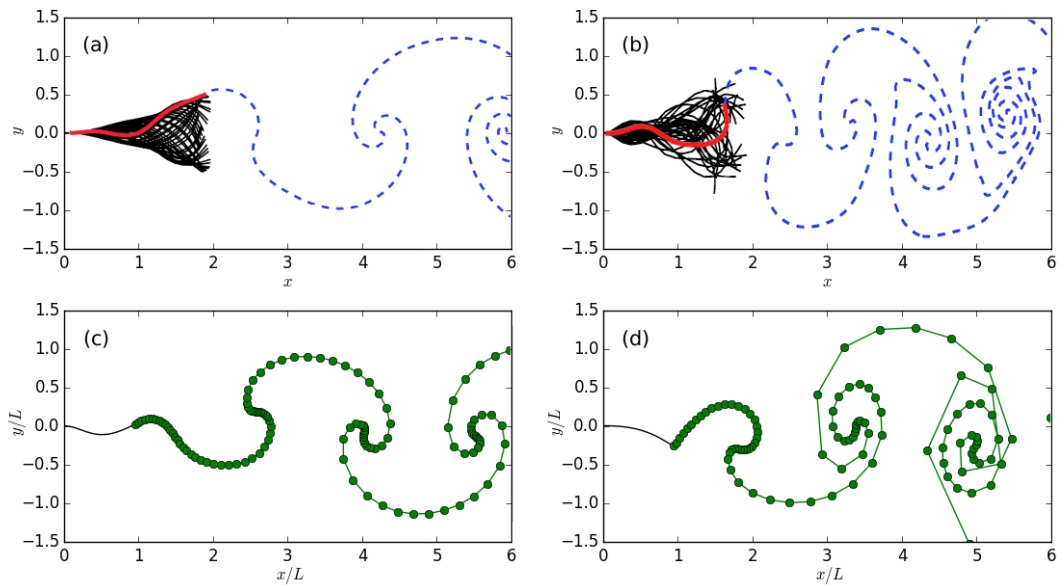


Figure 8.7: The wake roll-up found by the current model (c) and (d) compared to the equivalent figures in Alben and Shelley [2008], adapted in (a) and (b). Where (a) and (c) are at $\bar{U} = 7.58$, and (b) and (d) are at $\bar{U} = 7.77$.

8.5 Full Numerical Model

To validate the fully assembled model for the case where the wake is forced to leave from the plate trailing edge, physical properties were chosen such that the model was representative of that presented in Tang and Paidoussis [2007].

A comparison between the results produced by the present model and those of Tang and Païdoussis is shown in Figure 8.8. The left hand column of figures are adapted from Tang and Païdoussis [2007], and the corresponding result from the current model is shown in the right hand column. The first two rows of figures show the evolution of the vertical and horizontal tip deflection in time. It can be seen that in each case similar scale deflections are achieved, each model achieving saturation at approximately $\tau = 3$. The third row of figures shows snapshots of the plate at a number of time steps through the simulation. The fourth and fifth row of figures show the phase plots of the plate tip in the x - and y - directions respectively, and the final row shows a plot of the tip deflection in the x - and y - directions. In each of these final three rows there is good agreement seen between the two models, each achieving very similar shapes once the plate deflection has saturated and the limit cycle behaviour has been reached. It should be noted that there are two key difference between the model presented in Tang and Païdoussis [2007] and the current model. Firstly, in the current model the wake is allowed to move freely, whereas the wake used by Tang and Païdoussis is assumed to travel along a sinusoidal path. Secondly, the model presented by Tang and Païdoussis employs the Galerkin method and takes account of the first 6 modes, while the current model supports a far larger number of modal shapes that may arise.

8.5.1 Separation

The separation model is validated first against the well-known case of a cylinder in uniform flow. The properties of the cylinder, fluid, and flow speed were chosen to match those used in an image from Van Dyke [1982] and the model allowed to run for 1000 time steps. The results of this simulation and the figure adapted from Van Dyke [1982] are shown in Figure 8.9. In the numerical model the characteristic Von-Karman vortex street is formed from the two free-shear layers separating from the upper and lower extremes of the cylinder and matches very closely the form of the wake shown in the photograph.

The separation and wake models were also applied to two NACA aerofoils and the resulting predicted coefficients of lift are shown in Figure 8.10 where they are compared to predictions using thin aerofoil theory and the experimental results

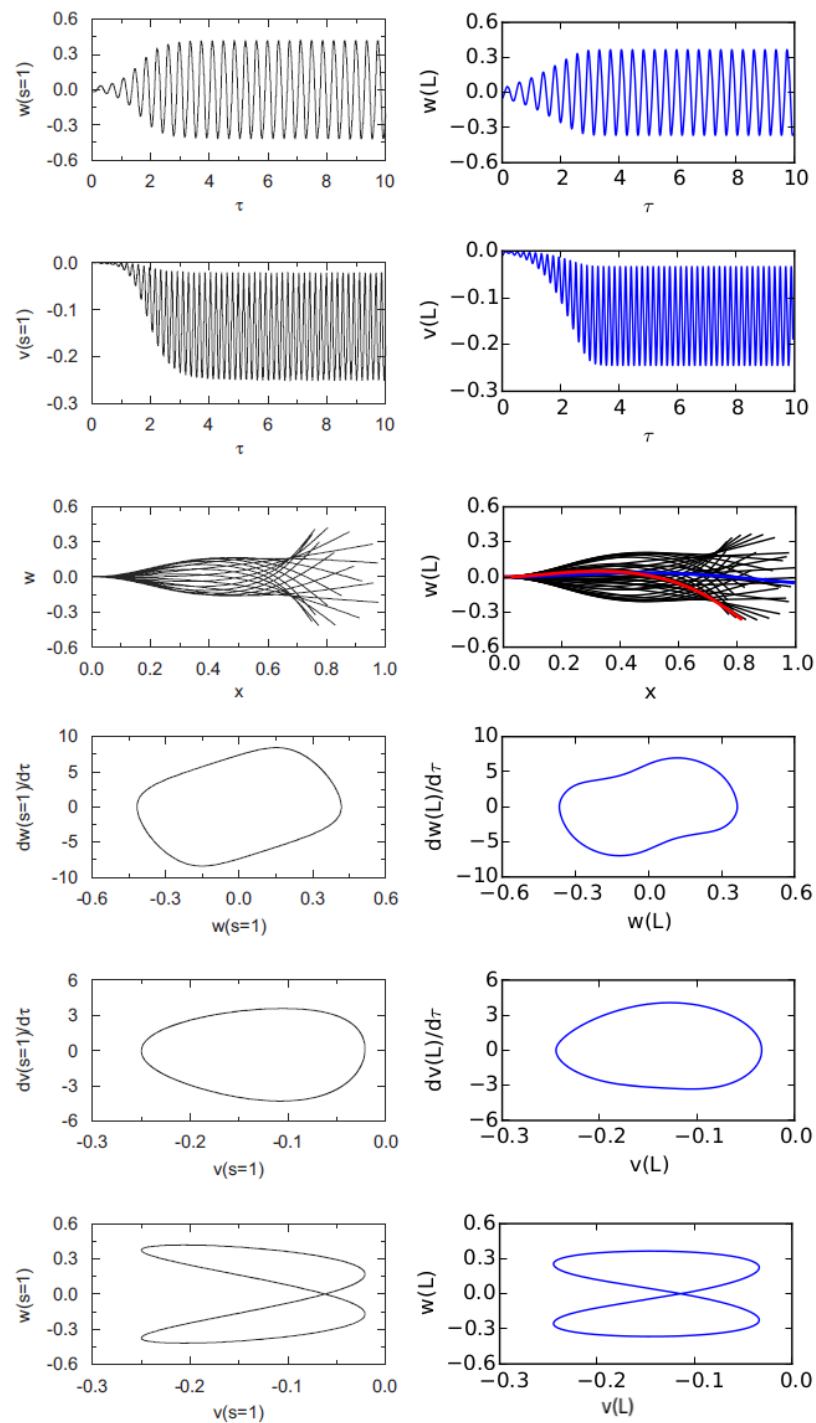


Figure 8.8: A comparison between the full numerical model (right) with no shear-layer separation, and the results presented by Tang and Paidoussis [2007] (left) for $\bar{L} = 0.2$ and $\bar{U} = 59.15$.

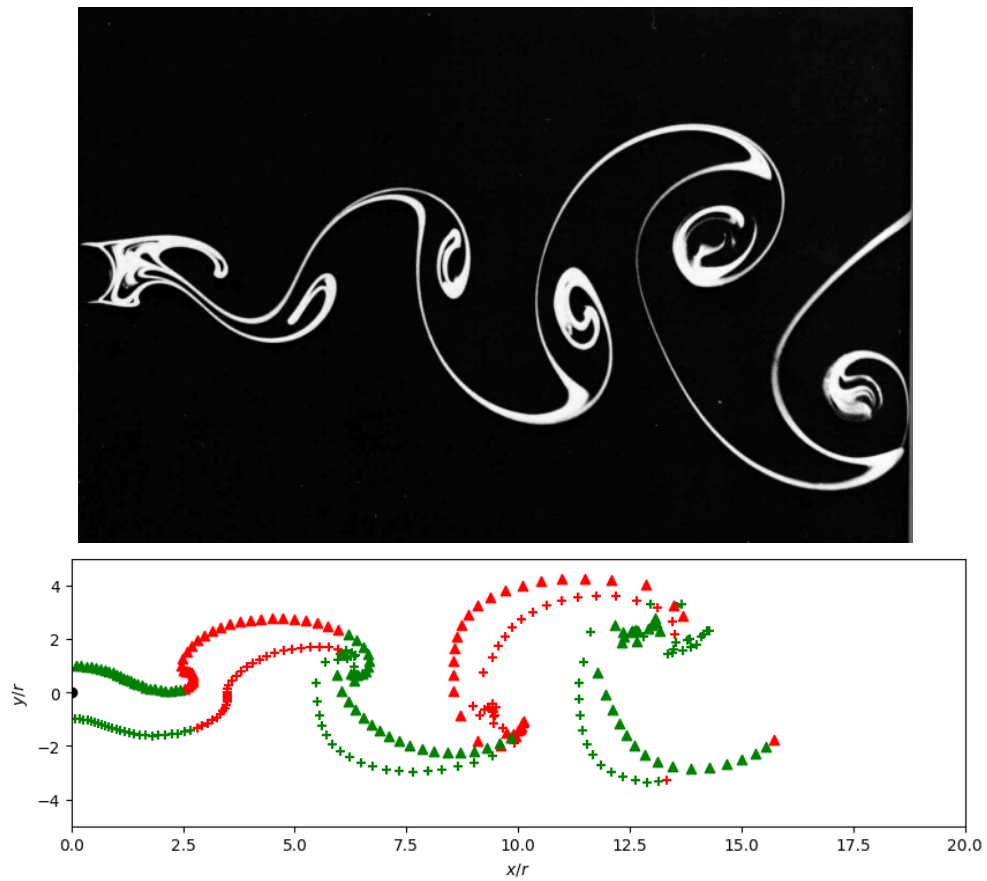


Figure 8.9: The wake formed behind a circular cylinder submerged in water, with a diameter of 1cm, and a flow speed of 1.4cm/s adapted from Van Dyke [1982] (top) and given by the present numerical model (bottom). Where the colour represents the sign of the vorticity, positive (green), negative (red), and the marker denotes the surface the vortex has been released from; upper (Δ), or lower (+).

of Abbott and Von Doenhoff [1959]. For the purposes of comparison a threshold value of 0 for the pressure gradient was selected, and separation was chosen to occur downstream of the point where an adverse pressure gradient was detected on either the upper or lower surface of the aerofoil. Figure 8.10a shows the model applied to a symmetric aerofoil and the results are seen to be in excellent agreement with the experimentally determined lift coefficient before the flow separates from the aerofoil. Examining the point at which the flow separates, it is seen that separation occurs at approximately $\pm 15^\circ$ in the experimental results, while the current model predicts separation at $\approx \pm 22^\circ$. Figure 8.10b shows the model applied to a cambered aerofoil, in this case the predicted separation point (16°) was much closer to the experimental result (14°). There are a number of potential reasons for differences between the theoretical model and the experimental results, for example there are other viscous effects that affect the result such as wall effects and blockage, which do not arise in the model presented. However, for both cases the predicted angle of attack required to achieve flow separation is close to the experimental value.

It is stated in the literature that it is impossible to predict the separation point accurately without some *a priori* knowledge from experiments (Leonard [1980], Sarpkaya [1989], Katz and Plotkin [2010]). Thus it is not known what the exact value of threshold pressure for separation should be for this study. However, the model can be calibrated against experimental results found in the literature, for example the results of Shelley et al. [2005] and Eloy et al. [2007, 2012] could be used to calibrate the model.

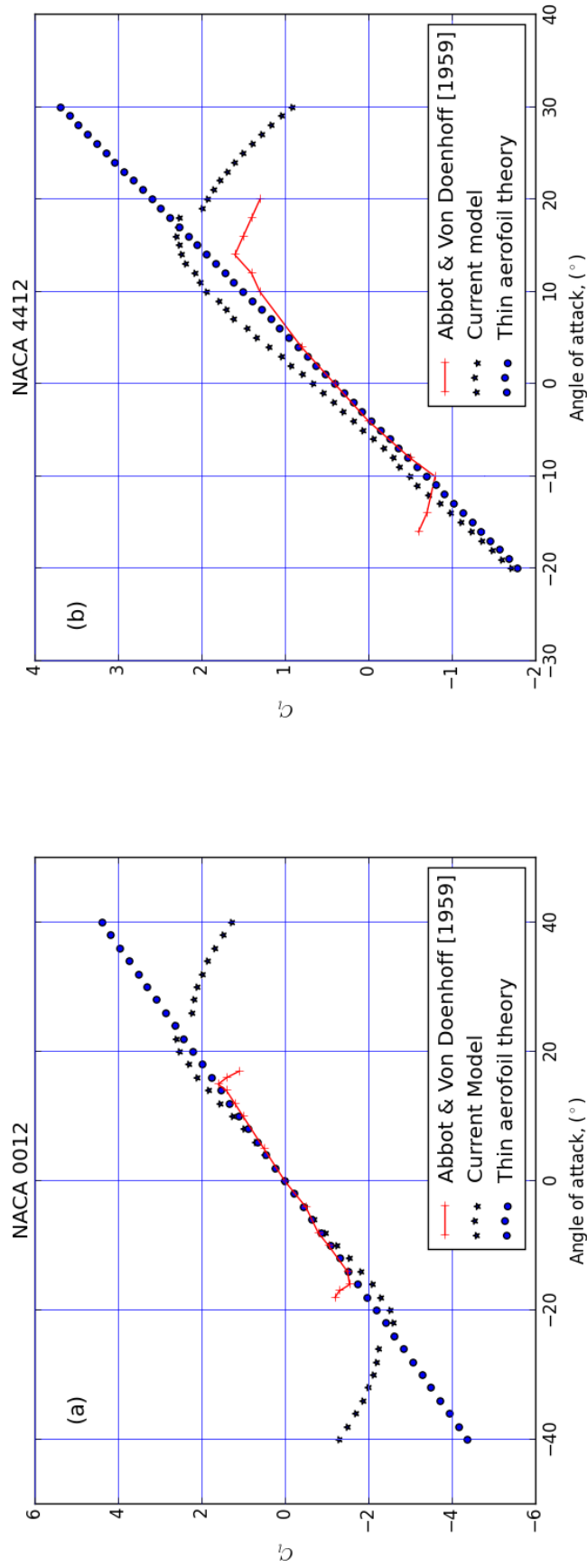


Figure 8.10: The coefficient of lift predicted by the current model, thin aerofoil theory, and the experimental results of Abbott and Von Doenhoff [1959] for the (a) NACA 0012 and (b) NACA 4412 aerofoils.

8.6 Summary

It is proposed that the components of the complete non-linear model have been validated. As in the linear model, a discretization of 50 nodes will be used as this provides results within an acceptable error of much finer discretizations but with a much lower computational cost. The plate will be initially deflected into the second *in-vacuo* mode shape with an initial amplitude at the upper limit of the linear regime. It is found that the non-linear plate and fluid models are able to recover the linear model result when the flutter amplitude is reduced down to a linear regime. When the wake is forced to separate from the trailing edge very good agreement is found with the model presented in Tang and Païdoussis [2007] which also made this assumption. The shape of the wake which forms as a result of this trailing edge separation serves to validate the prescribed sinusoidal form of the wake used by Tang and Païdoussis. The separation model has been validated in two different ways; firstly by applying the model to a submerged cylinder in steady flow - producing results which are a very close visual match to a corresponding experiment represented in Van Dyke [1982], and secondly it is used to predict the stall points of two different aerofoils which are then compared against the experimental results of Abbott and Von Doenhoff [1959]. The exact value of the separation criterion is unknown and the width of the hysteresis loop for sub-critical instability that this model is capable of identifying will depend on its value. However, this does not detract from the study, where the aim is to demonstrate flow separation can be a route to sub-critical instability. Thus it is proposed that the coupled non-linear model has been validated and can be used to generate new results which will elucidate on the phenomenology of flow separation and its effect on the system, perhaps without precise quantitative description.

Chapter 9

Results

The results focus on the maximum tip deflection achieved by the plate for a range of flow speeds, both above and below the critical speed for the onset of linear instability at which flutter first occurs for $\bar{L} = 1$.

It has been shown in section 7.3.2 that the system can be described by two control parameters, the non-dimensional flow speed \bar{U} and the mass ratio \bar{L} and thus these parameters are used herein. The results of including the effects of separation on the critical velocity and maximum stable deflection achieved are presented, and the results of varying the pressure threshold and initial deflection are examined. Finally the results of a pseudo-continuous model are shown and comparison is made between these results and those found in the literature.

9.1 Pressure Threshold Variation

The effect of separation was examined at a range of flow speeds and at a number of pressure gradient threshold (P_{thresh}) values. An example of these results is shown in Figure 9.1 for $\bar{U} = 7.16$ (approximately 40% above the critical velocity for the linear model). The first row shows the case where $P_{\text{thresh}} = 10.0$, which was found to be high enough to prohibit flow separation upstream of the trailing edge entirely. It was seen that the beam reaches neutrally stable oscillations at approximately $\bar{T} = 2.5$ and achieves a maximum amplitude of 0.28. The results shown in the second row are identical to the first, as the pressure threshold used (0.1) was still high enough to prevent separation upstream of the trailing edge.

Further decreasing the pressure threshold to 0.01 yielded the results shown in the third row. In this instance it can be seen that the system takes longer to reach saturation (approximately 0.15 at $\bar{T} = 4.0$), and that the system is much less stable. It was found that separation occurred at approximately 40% of the time steps using this pressure threshold value. The fourth row shows the results using $P_{\text{thresh}} = 0.001$, and it is seen that the maximum deflection achieved by the system in this case was further reduced from the previous result (achieving only $\eta_L/L = 0.13$), and taking almost the whole simulation time to reach this amplitude. Separation was observed to occur in 70% of the time steps in this simulation. Finally, using a pressure threshold of zero lead to the results shown in the last row, where it is clearly seen that the beam was unable to maintain self-sustaining oscillations, and that all energy was lost by the beam very quickly.

Figure 9.2 shows the results gained using these same pressure thresholds at a range of flow speeds and using different initial deflections. Figure 9.2a, b, and c show the results for $\eta_L^{t=0}/L = 0.01, 0.1, \text{ and } 0.2$ respectively. It is seen that as the flow speed increases each case has the same critical velocity, though for larger initial deflections; in Figures 9.2(b) and (c), the amplitude of the oscillations at these lower flow speeds is greater than in Figure 9.2(a) which represents the results when the initial deflection is close to the linear regime. At each initial deflection the line of $P_{\text{thresh}} = 0.1$ is identical to the $P_{\text{thresh}} = 10$ result until $\bar{U} \approx 7$, above which the results begin to diverge slightly as flow separation upstream of the trailing edge begins to occur as the combination of flow speed and amplitude are enough to overcome the threshold pressure. For the lower threshold pressures it is seen that this point is reached much sooner. In all cases each curve displays a consistent drop in steady-state amplitude above a certain flow speed. This is a result of the increasing levels of separation that were observed with increasing flow speed. For example it was seen during the experiments that for $P_{\text{thresh}} = 0.1$ at $\bar{U} = 8.81$ and $\eta_L^{t=0}/L = 0.2$ that the flow would separate in approximately 10% of the time steps, however at $\bar{U} = 11.5$ separation occurred at 50% of the time steps.

From Figure 9.1 and Figure 9.2 it is clear that separation upstream of the trailing edge has a significant effect on the system, causing the system to take

longer to reach saturation, and lowering the oscillation amplitude achieved. It can also be seen that the final results predicted by each model are mostly independent of the initial deflection, the only notable exception being at flow speeds close to the critical velocity, where bi-stability can be observed.

9.2 Hysteresis

To allow the model to more closely mimic the continuous transition between flow speeds seen in physical experiments, the final state of the model at one flow speed was used as the initial conditions for the next. Figure 9.3 shows the results produced by this pseudo-continuous model using (a) $P_{\text{thresh}} = 0.001$, (b) $P_{\text{thresh}} = 0.01$, and (c) $P_{\text{thresh}} = 0.1$. The dashed line shows the amplitude of the oscillations when the flow speed is increased, while the solid line shows the same amplitude when the flow speed is decreased. It can be seen that for $P_{\text{thresh}} = 0.001$ no hysteresis loop is observed. However, for $P_{\text{thresh}} = 0.01$ and 0.1 a clear sub-critical hysteresis loop is seen, where the system is able to maintain self-sustaining oscillations below the critical velocity. In each case the size of hysteresis loop is similar, the system becoming unstable initially at $\bar{U} = 5.51$, and returning to stability at $\bar{U} = 4.95$. At flow speeds much higher than the critical velocity for linear instability, the effects of separation are not significant. Amplification and subsequent non-linear saturation at finite amplitudes can be adequately modelled by wake formation from the trailing edge of the plate. However, at lower flow speeds separation can introduce an additional type of spatio-temporally varying fluid forcing to the flexible plate that enables energy transfer between flow and structure. Below the linear instability onset flow speed finite amplitude deflections can produce a curvature, combined with a sufficiently adverse pressure gradient, large enough to cause flow separation. Thus, at the flow speed for which the system is neutrally stable to linear disturbances, it is shown that separation can lead to non-linear instability and ensuing limit-cycle flutter.

Comparing the size of the hysteresis loop found to the experimental results presented by Watanabe et al. [2002a] shown in Figure 9.4 it can be seen that the hysteresis loop created by the present model is much smaller than that found in

the literature for the values of P_{thresh} examined herein. However, the amplitude of the deflections achieved by the present model are similar to those found by experiment. Overall, while complete agreement between the numerical model presented in this thesis and the experimental results of Watanabe et al. [2002a] is not seen, the flow speeds over which hysteresis is observed are similar, as are the amplitude of the oscillations.

9.3 Model Variation

The model presented is very flexible, in that it is possible to easily modify it in a number of ways to examine the influence of particular effects. For example, the effect of varying the pressure threshold but not modifying the pressure downstream of the separation point, as shown in Equation 7.3.4, is shown in Figure 9.5. The pressure along each surface being calculated using only Equations B.3.5a and B.3.5b. Where the maximum deflection once the simulation has reached a steady state for a range of pressure thresholds under these conditions are compared. This case would represent the formation of an additional free-shear layer owing to some other effect, for example an upstream disturbance such as a clamping mechanism, another beam, or some plate surface irregularity. Overall these results show that (i) a sub-critical hysteresis loop can be achieved by allowing the flow to separate under these conditions, and (ii) that the size of the hysteresis loop can be controlled through modifying the pressure threshold to satisfy the conditions for separation. It should be noted that for each P_{thresh} value the results when increasing flow speed were identical.

At higher flow speeds the results converge to give consistent maximum deflections regardless of flow separation before the transition to chaos as a result of the rapid convection of the wake vortices downstream. At lower flow speeds the forcing effect of the additional wake was found to be very significant and it is seen that the inclusion of this additional wake allows stable sub-critical instability in the system. Varying the pressure threshold, it is shown that it is possible to produce a range of hysteresis loops, the size of which depends on the threshold chosen. As the threshold is reduced the size of the hysteresis loop increases, until

a certain value where the loop begins decreasing in size.

Figure 9.6 shows the system behaviour at three different flow speeds (a) $\bar{U} = 5.50$ (the critical flow speed for linear instability), (b) $\bar{U} = 7.16$, and (c) $\bar{U} = 9.13$ for $\bar{L} = 1$. The first row of figures in each pair of rows shows the results of applying a high pressure threshold, such that the flow is unable to separate upstream of the trailing edge. The second row of figures shows the results where a threshold pressure of $P_{\text{thresh.}} = 0.01$. These two models are referred to as “forced” and “free” respectively. Figure 9.6 (a) shows that when the wake is forced to separate from the trailing edge the plate motion quickly settles into low-amplitude steady oscillations as predicted in linear studies. The bottom row shows a growth in amplitude, reaching non-linear saturation at approximately $\bar{T} = 1$ when the plate enters limit-cycle oscillations where the mode shape of the deflections is comprised principally of the first and second modes, and is captured by the red line at $\bar{T} = 4$. This is also seen in the time series of both the tip deflection (second column of sub-figures), and plate energy (third column of sub-figures). Figure 9.6 (b) compares the forced- and free-separation results at $\bar{U} = 7.13$, for which little difference is seen in the limit-cycle oscillations. However the free-separation model achieves saturation sooner than the tip-separation model, and achieves a slightly greater level of energy. From Figure 9.6 (c) it can be seen that there is little to no difference between the forced- and free-separation models, both achieving similar energy profiles and reaching steady oscillations at the same time. Indicating that the free-shear layers have a limited effect on the beam at higher flow speeds, where the wake is quickly convected downstream.

This modification to the model shows the importance of modifying the pressure downstream of the separation point, and that the inclusion of an additional free-shear layer without this pressure modification acts as an extra forcing term, allowing non-linear amplitude oscillations well below the critical velocity.

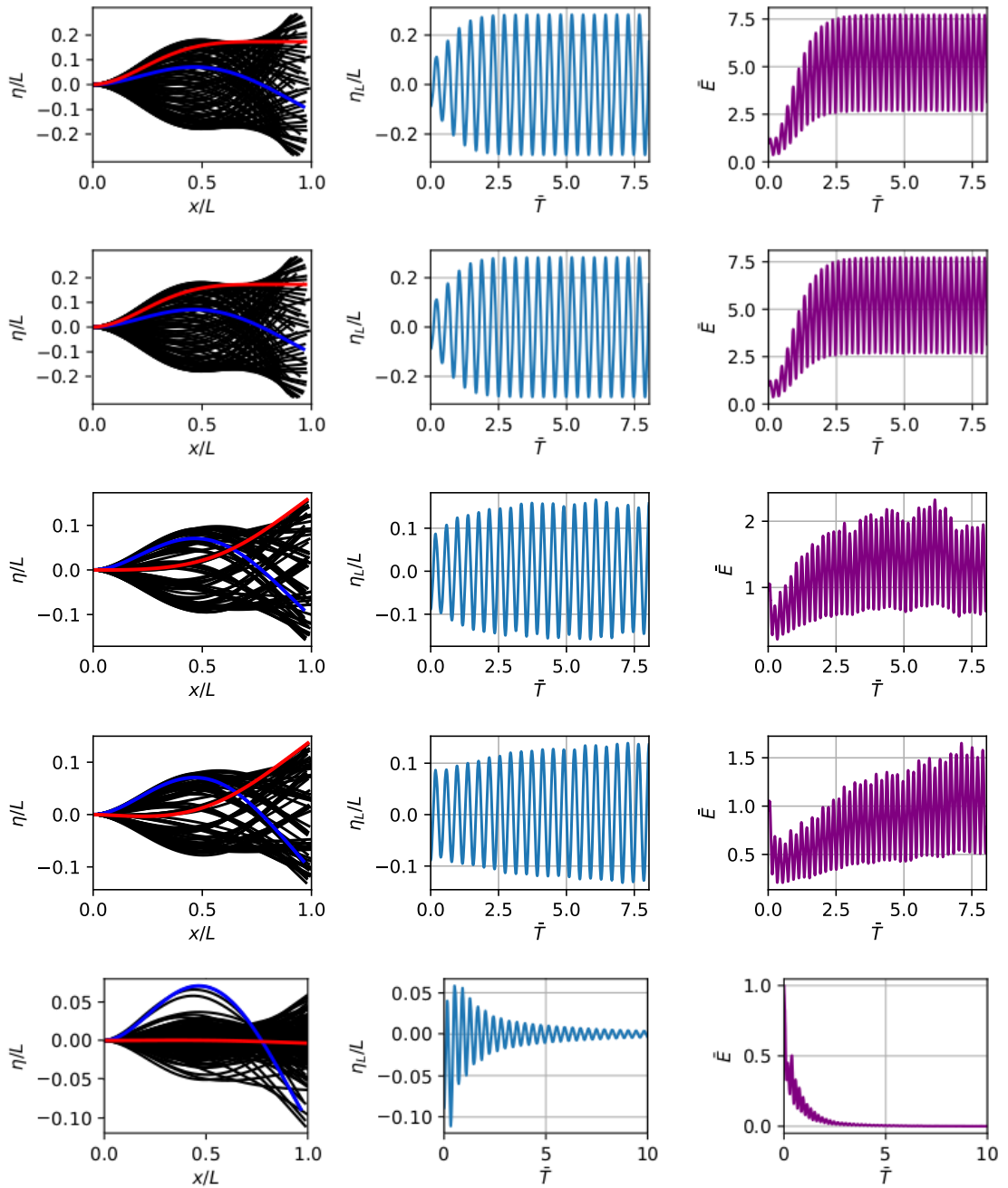


Figure 9.1: The deflection predicted for $\bar{L} = 1$, and $\bar{U} = 7.16$ where each row from top to bottom represents the results when $P_{\text{thresh}} = 10.0, 0.1, 0.01, 0.001$, and 0.0 . In each row the first column of figures shows snapshots of the beam deflection at regular intervals throughout the experiment with the blue and red lines showing the initial and final displacement respectively. The second and third columns show a trace of the vertical tip deflection and beam energy in time.

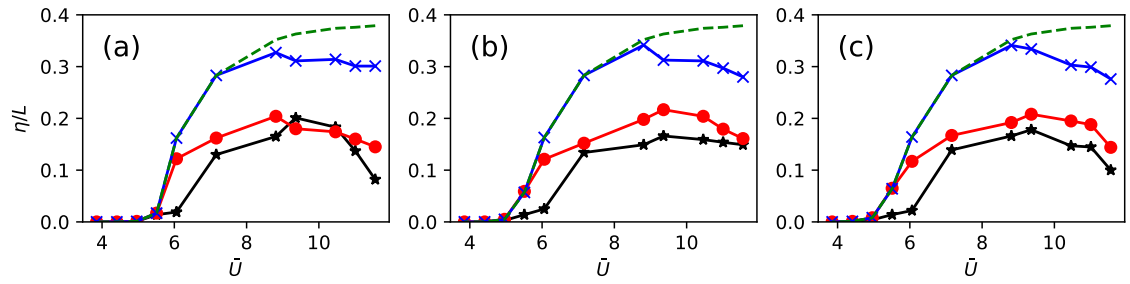


Figure 9.2: The deflection predicted for (a) $\eta_L^{t=0} = 0.01L$, (b) $\eta_L^{t=0} = 0.1L$, and (c) $\eta_L^{t=0} = 0.2L$. Each line represents the results for a different threshold pressure value; $P_{\text{thresh}} = 0.001$ (\star), $P_{\text{thresh}} = 0.01$ (\bullet), $P_{\text{thresh}} = 0.1$ (\times). $P_{\text{thresh}} = 10.0$ is shown by the dashed line.

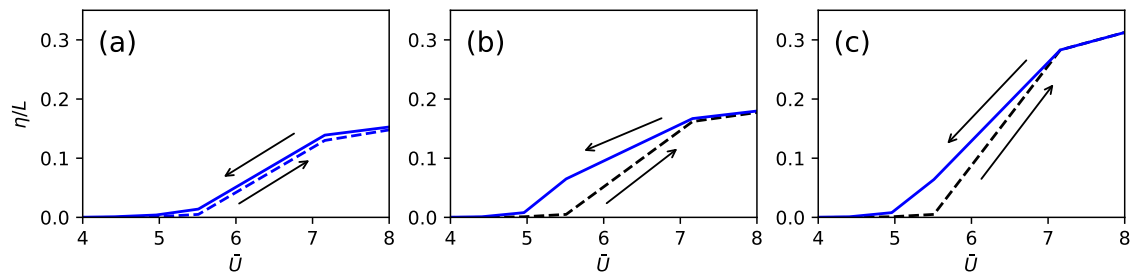


Figure 9.3: The maximum stable deflection achieved when first increasing and then decreasing the flow speed for (a) $P_{\text{thresh}} = 0.001$, (b) $P_{\text{thresh}} = 0.01$, and (c) $P_{\text{thresh}} = 0.1$. In each case the dashed and solid lines represent the deflection achieved when increasing and decreasing the flow speed respectively.

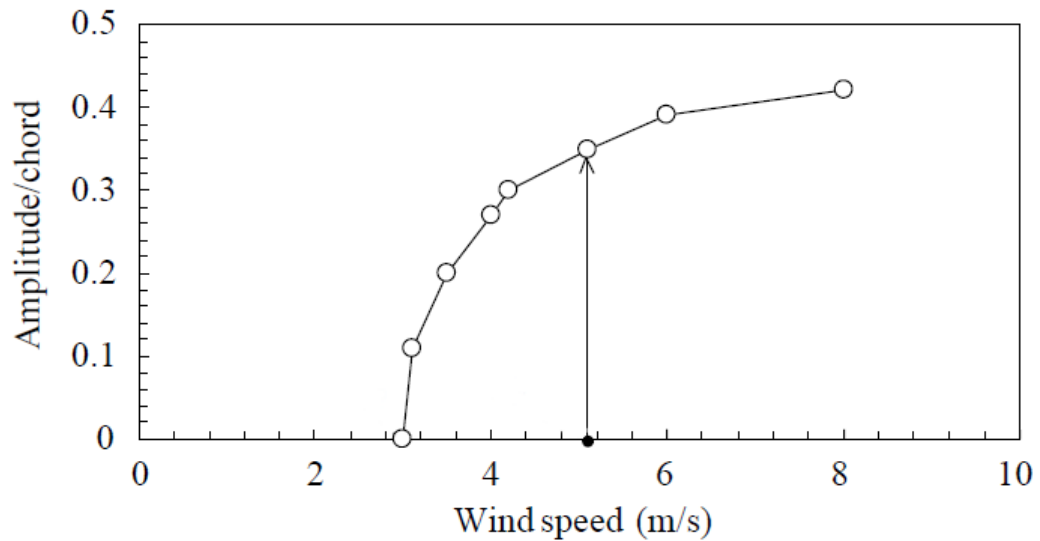


Figure 9.4: The hysteresis loop found in experiment for $\bar{L} = 1$, adapted from Watanabe et al. [2002a]. Where the black marker indicates the flow speed at which the oscillations began.

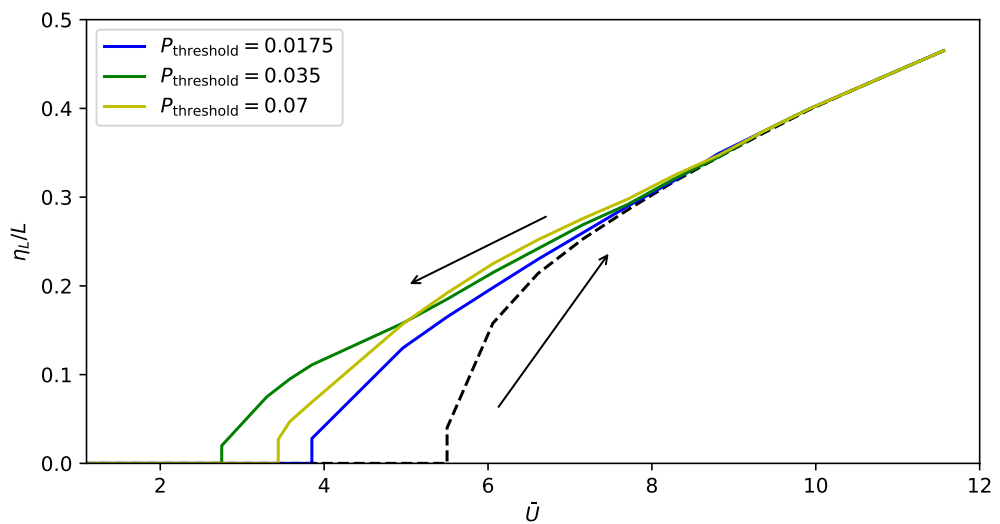


Figure 9.5: The maximum deflection achieved using a modified version of the non-linear model once the system has entered self-sustaining oscillations at various pressure gradient thresholds for $\bar{L} = 1$. The dashed and solid lines represent the results when the flow speed is increased and decreased respectively.

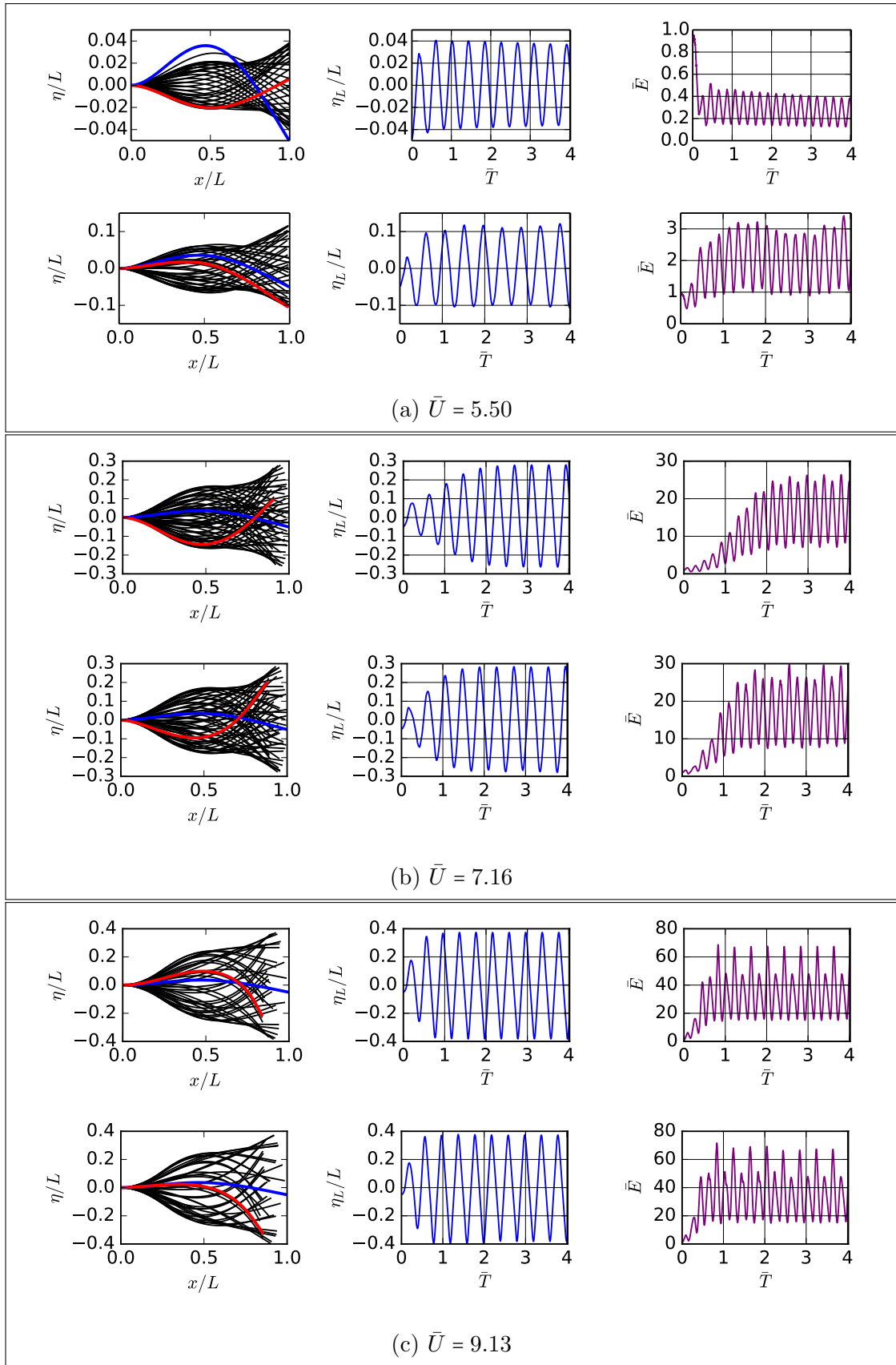


Figure 9.6: Oscillation of a cantilevered plate in axial flow at $\bar{L} = 1$. Within each group of sub-figures, the top row shows the results when wake formation is restricted to the trailing edge, and the bottom row shows corresponding results when separation is allowed to occur upstream of the trailing edge. The first column of sub-figures are snapshots in time of plate displacement; blue and red profiles are respectively the initial and final deflections. Second and third columns respectively show time series of plate-tip deflection and plate energy, the latter normalised by the strain energy of the plate in its initial deflection.

Chapter 10

Summary

A new model has been developed which allows the effect of the wake and flow separation upstream of the trailing edge on the fluid-structure system to be examined, extending upon the work presented in Part II, and the work of Howell et al. [2009]. This new model shows that it is possible to modify the result of numerical experiments by varying the ease with which flow can separate from the beam. At flow speeds much higher than the critical flow velocity for linear instability the effects of separation are significant, causing a large deviation from the result where this separation is not modelled. It was also shown that flow separation inhibits the transfer of energy to the beam, slowing the rate at which non-linear saturation at finite amplitudes can be reached.

At the flow speed for which the system is neutrally stable to linear disturbances, separation can lead to non-linear instability and ensuing limit-cycle flutter. This suggests that flow separation may be a mechanism for the sub-critical instability that is observed in experimental work, for example that of Watanabe et al. [2002a]. Correctly modelling sub-critical instability relies upon choosing a threshold value of pressure gradient for separation that can only be found from experiment. However this does not negate the significance of the findings presented here which show that flow separation is a route and potential contributor to the sub-critical instability found in the experiments presented in the literature.

The present model provides benefits over other more complete models, for example that used by Connell and Yue [2007], as it is possible to examine the underlying physics present within this system with regards to the specific inter-

actions involved and the effects they each have.

Part IV

Conclusions

Chapter 11

Conclusions and Further Work

11.1 Conclusions

A number of new models, involving a combination of boundary-value, initial-value, and discrete vortex methods have been developed to investigate the interaction between ideal flow and a flexible cantilevered plate at both small- and large-amplitude deflections.

11.1.1 Small-Amplitude Oscillations

Investigation into the importance of the wake with regards to the onset of instability in a cantilevered flexible plate was performed by combining finite-difference and boundary-value techniques similar to those developed in Howell et al. [2009]. The effect of jerk on the system stability was examined and it was shown that its omission resulted in a more stable system than when the jerk was included in the fully discretised wake model. A numerical simulation was then developed in which the wake was modelled as a single vortex and was found to give similar stability predictions to the distributed wake model.

Two boundary-value models were then developed to include the effect of the wake as an extension to the methods developed by Howell et al. [2009] and Pitman and Lucey [2009]. The difference between the first and second boundary-value models is a result of the way in which the wake vorticity is determined through interpretations of the Kelvin condition. Both models are capable of capturing the qualitative effect of a wake on the stability of the system using only a single vortex.

The first model produced results which compared very well to the full-wake initial-value results for $\bar{L} \leq 2$ with regards to the predicted critical velocity and the point at which the wake changed from having a stabilising to a destabilising effect on the system stability. The second model gave results which were very similar to the no-wake case and indicated that the wake always had a stabilising effect on the system which is not consistent with the other results presented in the present work or in the literature. Both models showed the appearance of higher order modes with increasing mass ratio, the instability changing from single-mode to modal-coalescence type flutter as noted in the literature (for example in Howell et al. [2009], Eloy et al. [2012], and Tang and Paidoussis [2007]). These new models show that it is possible to model the wake using only a single lumped vortex while still producing qualitatively correct results especially for $\bar{L} \leq 2$.

Finally a strong dependence on a fluid-to-plate density ratio beyond that contained within the mass ratio was found in both the full initial-value model and in the boundary-value models. It was shown that for high density ratios the wake had no effect on the system, while having a noticeable stabilising or destabilising effect on systems of low density ratio. This dependence appears as a result of the implicit inclusion of viscosity through the Kutta condition which introduces a Strouhal number to the system. This phenomenon has been noted in the study of compliant panels (Carpenter et al. [2001]). However, to the author's knowledge it has not been observed or commented upon with regards to studies of cantilevered flexible plates.

11.1.2 Large-Amplitude Oscillation

The investigation into the effects of flow separation as a possible route to the sub-critical instability and hysteresis was performed by extending the small-amplitude oscillation model to account for large-amplitude deflections, and allowing a free-shear layer to form upstream of the trailing edge when separation was adjudged to occur. This separation was controlled by introducing a pressure threshold parameter, below which separation would not occur. It was shown that by varying this parameter the model predicted sub-critical hysteresis.

Firstly, a comparison was made between five pressure thresholds at a flow

speed above the critical velocity for linear instability: the first high enough to only permit flow separation at the trailing edge, and the last, such that separation would always occur upstream of the trailing edge, and others that were selected to cover a range between these two cases. It was found that allowing separation to occur along the body of the beam resulted in lower oscillation amplitudes and a slower rate of amplification to saturation. It was also noted that the inclusion of flow separation made the oscillations more irregular. Raising the threshold pressure produced results increasingly similar to the case where no separation was permitted until the results converged entirely. The range of flow speeds examined was then expanded and it was seen that there was a large difference in the saturated states observed between each pressure threshold value at higher flow speeds, however at lower flow speeds the results tended to converge. The results predicted by each model were very similar. It was also found that the results were largely unaffected by the initial deflection applied to the beam, except at lower flow speeds where some bi-stability was observed.

Secondly, the model was modified to take the final saturated state of a previous simulation as the input to a subsequent simulation at a lower flow speed, allowing the model to approximate the continuous change in velocity used in experiments. It was found that self-sustaining oscillations were present at sub-critical velocities for certain pressure threshold values, enabled by the upstream flow separation. For $\bar{L} = 1$ and $P_{\text{thresh}} = 0.01$ the width of the separation loop was found to be approximately $\Delta\bar{U} = 0.6$. These results show that it is possible to produce self-sustaining sub-critical oscillations if the affect of flow separation upstream of the trailing edge is included. The model was then compared to the experimental results of Watanabe et al. [2002a]. It was shown that it is possible to produce sub-critical instability hysteresis loops very similar to those presented in the literature. However the size of the hysteresis loop predicted by the present model was much smaller than that found by Watanabe et al. although the amplitude of the oscillations was similar. This demonstrates that flow separation upstream of the trailing edge could be a cause of the sub-critical hysteresis loop observed in these experiments. This is in disagreement with other numerical results found in the literature, for example the work of Yadykin et al. [2001], and Tang and

Païdoussis [2007], who predicted super-critical effects and proposed that the sub-critical hysteresis observed in experiments was the result of in-plane bending, or material defects not included in their models. A key difference between the models presented in Yadykin et al. [2001], and Tang and Païdoussis [2007], is that neither included flow separation upstream of the trailing edge, which could be the source of the differing conclusions.

Finally the versatility of the present model was demonstrated by suppressing modified pressure acting on the surface of the beam downstream of the point of separation (Equation 7.3.4). In this case it was found that flow separation was capable of producing a much larger hysteresis loop which compares much better with results found in the literature. It was also found that there was a critical pressure threshold that was capable of producing the largest hysteresis loop, and that above and below this value the loop would decrease in size. This demonstrates the importance of modifying the pressure downstream of the separation point on the surface of the beam, as without it the additional wake acts as an extra forcing term over a large portion of the beam promoting non-linear oscillations at very low flow speeds. This can be seen by comparing the size of the hysteresis loops produced in Figure 9.2 and Figure 9.5.

11.2 Further Work

The work presented in each half of this thesis can be extended in a number of interesting and valuable directions.

11.2.1 Linear Model

- The state-space model could be developed to take account of multiple wake vortices, and used to explore the effect of the Strouhal number further. Extending this model to include the effects of added mass or stiffened panels would be further extensions.
- Rigid channel walls could also be added to the state-space model in a similar way to that described in Howell et al. [2009].

- The effect of the Strouhal number can also be examined on the non-linear system developed in this thesis. This could be compared directly with the results presented in Connell and Yue [2007] who discuss the Strouhal number and its effect on a non-linear, post-critical system.
- Deeper examination and experimentation with the wake model, for example timing the release of wake vortices with the oscillation frequency of the plate, and allowing vortices to leave the trailing edge in pairs representing the vorticity on the upper and lower surface.

11.2.2 Non-Linear Model

- The non-linear models developed could also be readily extended to include multiple flexible plates in various configurations, for example side-by-side or in-line. Examples of these configurations exist in the literature (such as in Alben [2009b], who studied flags in both parallel and series configurations to show that the combination of wakes could lead to unusual synchronous and erratic flapping behaviour observed in experiments) as both experimental and theoretical results. However, the simplicity of the model presented in this thesis would allow a deeper exploration of the interactions between multiple plates and their respective wakes.
- The non-linear model could be improved by allowing the inclusion of a time-dependent mean flow rate (the present model only permits a constant velocity). This would allow for a more direct comparison with the experimental results presented in the literature.
- The wake model can be extended in several ways, for example it could allow for flow reattachment and thus allow the exploration of how that particular phenomenon affects the coupled system. The viscosity, implicitly present through the introduction of flow separation, would also result in the dissipation of vortices in time. While this effect was not included in this study the wake model could be extended to take account of this additional effect by additionally solving the heat equation in an operator-splitting approach to solving the vorticity evolution within the discrete-vortex method.

- Exploring the flutter regimes that exist beyond limit-cycle oscillation.
- Migrating the code base to a more structured language to allow for more detailed simulations.
- Further exploration of the present wake model, for example deeper examination of the mechanisms underlying separation, the location and times that separation occurs, and the percentage time that the system experiences separation.

Bibliography

- I. H. Abbott and A. E. Von Doenhoff. *Theory of Wing Sections*. Dover Publications Inc., first edition, 1959.
- S. Alben. Optimal flexibility of a flapping appendage in an inviscid fluid. *Journal of Fluid Mechanics*, 614:355–380, 2008.
- S. Alben. Simulating the dynamics of flexible bodies and vortex sheets. *Journal of Computational Physics*, 228:2587–2603, 2009a.
- S. Alben. Wake-mediated synchronization and drafting in coupled flags. *Journal of Fluid Mechanics*, 641:489–496, 2009b.
- S. Alben and M. J. Shelley. Flapping states of a flag in an inviscid fluid: Bistability and the transition to chaos. *Physical Review Letters*, 100(074301), 2008.
- J. J. Allen and A. J. Smits. Energy harvesting eel. *Journal of Fluids and Structures*, 15:629–640, 2001.
- M. Argentina and L. Mahadevan. Fluid-flow-induced flutter of a flag. *Proceedings of the National Academy of Sciences U.S.A.*, 102(6):1892–1834, 2008.
- P. Attar, E. Dowell, and D. Tang. Modeling aerodynamic nonlinearities for two aeroelastic configurations: Delta wing and flapping flag. In *A collection of technical papers: 44th AIAA/ASME/ASCE/AHS/ASC Structures, Structural Dynamics, and Materials Conference*, pages 12–22. American Institute of Aeronautics and Astronautics, April 2003.
- Y. Aurégan and C. Depollier. Snoring: linear stability analysis and *in-vitro* experiments. *Journal of Sound and Vibration*, 188(1):39–54, 1995.

- T. S. Balint and A. D. Lucey. Instability of a cantilevered flexible plate in viscous channel flow. *Journal of Fluids and Structures*, 20:893–912, 2005.
- T. B. Benjamin. Effects of a flexible boundary on hydrodynamic instability. *Journal of Fluid Mechanics*, 9:513–532, 1960.
- T. B. Benjamin. The threefold classification of unstable disturbances in flexible surfaces bounding inviscid flows. *Journal of Fluid Mechanics*, 16:436–450, 1963.
- G. J. Cafolla. *Hydroelastic Instability of Compliant Panels*. PhD thesis, University of Warwick, 1997.
- P. W. Carpenter and A. D. Garrad. The hydrodynamic stability of flow over kramer-type compliant surfaces. part 2. flow-induced surface instabilities. *Journal of Fluid Mechanics*, 170:199–232, 1986.
- P. W. Carpenter, A. D. Lucey, and C. Davies. Progress on the use of compliant walls for laminar-flow control. *Journal of Aircraft*, 38(3):504–512, 2001.
- A. J. Chorin. Numerical study of slightly viscous flow. *Journal of Fluid Mechanics*, 57:785–796, 1973.
- B. S. H. Connell and D. K. Yue. Flappy dynamics of a flag in a uniform stream. *Journal of Fluid Mechanics*, 581:33–67, 2007.
- D. G. Crighton and J. E. Oswell. Fluid loading with mean flow. i. response of an elastic plate to localized excitation. *Philosophical Transactions of the Royal Society of London A*, 335:557–592, 1991.
- S. K. Datta and W. G. Gottenberg. Instability of an elastic strip hanging in an airstream. *Journal of Applied Mechanics*, 42:195–198, 1975.
- O. Doaré and S. Michelin. Piezoelectric coupling in energy-harvesting fluttering flexible plates: linear stability analysis and conversion efficiency. *Journal of Fluids and Structures*, 27:1357–1375, 2011.
- N. S. J. Elliot, A. D. Lucey, and M. Heil. Large-amplitude oscillations of a finite-thickness cantilevered flexible plate in viscous channel flow. In *3rd*

- Joint US-European Fluids Engineering Summer Meeting and 8th International Conference on Nanochannels, Microchannels and Minichannels (FEDSM-ICNMM2010)*, pages 287–295. Montreal, Canada: American Society of Mechanical Engineers (ASME), Aug 2010.
- C. Eloy, C. Souilliez, and L. Schouveiler. Flutter of a rectangular plate. *Journal of Fluids and Structures*, 23:904–919, 2007.
- C. Eloy, R. Lagrange, C. Souilliez, and L. Schouveiler. Aeroelastic instability of cantilevered flexible plates in uniform flow. *Journal of Fluid Mechanics*, 611:97–106, 2008.
- C. Eloy, N. Kofman, and L. Schouveiler. The origin of hysteresis in the flag instability. *Journal of Fluid Mechanics*, 691:583–593, 2012.
- J. P. Giesing. Nonlinear interaction of two lifting bodies in arbitrary unstable motion. *Journal of Basic Engineering*, pages 387–394, 1968.
- J. P. Giesing. Vorticity and kutta condition for unsteady multienergy flows. *Journal of Applied Mechanics*, pages 608–613, 1969.
- J. P. Giesing. Two-dimensional potential flow theory for multiple bodies in small amplitude motion. *The American Institute of Aeronautics and Astronautics*, 8(11):1944–1953, 1970.
- C. Q. Guo and M. P. Paidoussis. Stability of rectangular plates with free side-edges in two-dimensional inviscid channel flow. *Journal of Applied Mechanics*, 67:171–176, 2000.
- E. L. Houghton and P. W. Carpenter. *Aerodynamics for Engineering Students*. Edward Arnold, fourth edition, 1993.
- R. M. Howell. *Snoring: A Flow-Structure Interaction*. PhD thesis, University of Warwick, 2006.
- R. M. Howell, A. D. Lucey, P. W. Carpenter, and M. W. Pitman. Interaction between a cantilevered-free flexible plate and ideal flow. *Journal of Fluids and Structures*, 25:544–566, 2009.

- R. M. Howell, A. D. Lucey, and M. W. Pitman. The effect of inertial inhomogeneity on the flutter of a cantilevered flexible plate. *Journal of Fluids and Structures*, 27(3):383–393, 2011.
- L. Huang. Flutter of cantilevered plates in axial flow. *Journal of Fluids and Structures*, 9:127–147, 1995.
- L. Huang and C. Zhang. Modal analysis of cantilever plate flutter. *Journal of Fluids and Structures*, 38:273–289, 2013.
- J. Katz and A. Plotkin. *Low-Speed Aerodynamics*. Cambridge University Press, second edition, 2010.
- A. Kornecki, E. H. Dowell, and J. O’Brien. On the aeroelastic instability of two-dimensional panels in uniform incompressible flow. *Journal of Sound and Vibration*, 47(2):163–178, 1976.
- A. M. Kuethe and J. D. Schetzer. *Foundations of aerodynamics*. John Wiley & Sons, inc., second edition, 1959.
- H. Lamb. *Hydrodynamics*. Dover Publications, sixth edition, 1945.
- M. T. Landahl. On the stability of a laminar incompressible boundary layer over a flexible surface. *Journal of Fluids Mechanics*, 13(4):609–632, 1962.
- C. Lemaitre, P. Hémon, and E. de Langre. Instability of a long ribbon hanging in axial air flow. *Journal of Fluids and Structures*, 20:913–925, 2005.
- A. Leonard. Vortex methods for flow simulation. *Journal of Computational Physics*, 37:289–335, 1980.
- J. C. Liao, D. N. Beal, G. V. Lauder, and M. S. Triantafyllou. Fish exploiting vortices decrease muscle activity. *Science*, 302(5650):1566–1569, 2003a.
- J. C. Liao, D. N. Beal, G. V. Lauder, and M. S. Triantafyllou. The kármán gait: novel body kinematics of rainbow trout swimming in a vortex street. *Journal of Experimental Biology*, 206:1059–1073, 2003b.

- M. J. Lighthill. Large-amplitude elongated-body theory of fish locomotion. *Proceedings of the Royal Society of London B*, 179:125–138, 1971.
- A. D. Lucey. *Hydroelastic Instability of a Flexible Surface*. PhD thesis, University of Exeter, 1989.
- A. D. Lucey and P. W. Carpenter. A numerical simulation of the interaction of a compliant wall and inviscid flow. *Journal of Fluid Mechanics*, 234:121–146, 1992.
- A. D. Lucey, G. J. Cafolla, P. W. Carpenter, and M. Yang. The nonlinear hydroelastic behaviour of flexible walls. *Journal of Fluids and Structures*, 11:717–744, 1997.
- A. Manela and M. S. Howe. The forced motion of a flag. *Journal of Fluid Mechanics*, 635:439–454, 2009.
- W. McKinney and J. DeLaurier. The wingmill: An oscillating-wing windmill. *Journal of Energy*, 5:109–115, 1981.
- S. Michelin, S. G. Llewellyn Smith, and B. J. Glover. Vortex shedding model of a flapping flag. *Journal of Fluid Mechanics*, 617(4):1–10, 2008.
- P. M. Moretti. Tension on fluttering flags. *Journal of Acoustics and Vibration*, 8:227–230, 2003.
- P. M. Moretti. Flag flutter amplitudes. *Flow Induced Vibration, de Langre & Arisa ed. Ecole Polytechnique, Paris, 6-9th July 2004*, 2004.
- M. T. Morris-Thomas and S. Steen. Experiments on the stability and drag of a flexible sheet under in-plane tension in uniform flow. *Journal of Fluids and Structures*, 25(5):815–830, 2009.
- U. K. Müller. Fish 'n flag. *Science*, 302(5650):1511–1512, 2003.
- W. Nowacki. *Dynamics of Elastic Systems*. Chapman and Hall, first edition, 1963.

- F. Paraz, C. Eloy, and L. Schouveiler. Vortex patterns generated by a heaving flexible plate. *Journal of Visualization*, 17(4):295–297, 2014.
- M. W. Pitman and A. D. Lucey. On the direct determination of the eigenmodes of finite flow-structure systems. *Proceedings of the Royal Society A*, 465:257–281, 2009.
- Lord Rayleigh. On the instability of jets. *Proceedings of the London Mathematical Society*, 10:4–12, 1879.
- P. G. Saffman. *Vortex Dynamics*. Cambridge University Press, 1992.
- P. G. Saffman and G. R. Baker. Vortex interactions. *Annual Review of Fluid Mechanics*, 11:95–122, 1979.
- T. Sarpkaya. Computational methods with vortices - the 1988 freeman scholar lecture. *Journal of Fluids Engineering*, 111:5–51, 1989.
- C. Semler, G. X. Li, and Paidoussis. The non-linear equations of motion of pipes conveying fluid. *Journal of Sound and Vibration*, 169(5):577–599, 1994.
- L. K. Shayo. The stability of cantilever panels in uniform incompressible flow. *Journal of Sound and Vibration*, 68(3):341–350, 1980.
- M. Shelley, N. Vandenberghe, and J. Zhang. Heavy flags undergo spontaneous oscillations in flowing water. *Physical Review Letters*, 94(094302), 2005.
- R. Stearman. Small aspect ratio membrane flutter. *California Institute of Technology Report AFOSR-TR*, 1:45–59, 1959.
- S. Taneda. Waving motions of flags. *Journal of the Physical Society of Japan*, 24(2):392–401, 1968.
- D. M. Tang and E. H. Dowell. Limit cycle oscillations of two-dimensional panels in low subsonic flow. *International Journal of Non-Linear Mechanics*, 37:1199–1209, 2002.
- D. M. Tang, H. Yamamoto, and E. H. Dowell. Flutter and limit cycle oscillations of two-dimensional panels in three-dimensional axial flow. *Journal of Fluids and Structures*, 17:225–242, 2003.

- L. Tang and M. P. Paidoussis. On the instability and the post-critical behaviour of two-dimensional cantilevered flexible plates in axial flow. *Journal of Sound and Vibration*, 305:97–115, 2007.
- L. Tang and M. P. Paidoussis. The influence of the wake on the stability of cantilevered flexible plates in axial flow. *Journal of Sound and Vibration*, 310:512–526, 2008.
- L. Tang, M. P. Paidoussis, and J. Jiang. The dynamics of variants of two-dimensional cantilevered flexible plates in axial flow. *Journal of Sound and Vibration*, 323:214–231, 2009a.
- L. Tang, M. P. Paidoussis, and J. Jiang. Cantilevered flexible plates in axial flow: Energy transfer and the concept of a flutter-mill. *Journal of Sound and Vibration*, 326:263–276, 2009b.
- G. W. Taylor, J. R. Burns, S. A. Kammann, W. B. Powers, and T. R. Welsh. The energy harvesting eel: a small subsurface ocean/river power generator. *Journal of Oceanic Engineering*, 26:539–547, 2001.
- D. Thoma. Warum flattert die fahne. *Mitteilungen des Hydraulischen Instituts der Technischen Hochschule München*, 9:30–34, 1939.
- M. Van Dyke. *An Album of Fluid Motion*. Parabolic Press, 1982.
- Y. Watanabe, S. Suzuki, M. Sugihara, and Y. Sueoka. An experimental study of paper flutter. *Journal of Fluids and Structures*, 16(4):529–542, 2002a.
- Y. Watanabe, K. Isogai, S. Suzuki, and M. Sugihara. A theoretical study of paper flutter. *Journal of Fluids and Structures*, 16(4):543–560, 2002b.
- Y. Yadykin, V. Tenetov, and D. Levin. The flow-induced vibration of a flexible strip hanging vertically in a parallel flow part 1: Temporal aeroelastic instability. *Journal of Fluids and Structures*, 15:1167–1185, 2001.
- N. Yamaguchi, K. Yokota, and Y. Tsumimoto. Flutter limits and behaviours of a flexible thin sheet in high speed flow — I: analytical method for prediction of the sheet behaviour. *Journal of Fluids Engineering*, 122:65–73, 2000a.

- J. Zhang, S. Childress, A. Libchaber, and M. Shelley. Flexible filaments in a flowing soap film as a model for one-dimensional flags in a two-dimensional wind. *Nature*, 408:836–839, 2000.
- W. Zhao, M. P. Paidoussis, L. Tang, M. Liu, and J. Jiang. Theoretical and experimental investigations of the dynamics of cantilevered flexible plates subjected to axial flow. *Journal of Sound and Vibration*, 331:575–587, 2012.
- L. Zhu and C. S. Peskin. Simulation of a flapping flexible filament in a flowing soap film by the immersed boundary method. *Journal of Computational Physics*, 179:452–468, 2002.

Every reasonable effort has been made to acknowledge the owners of copyright material. I would be pleased to hear from any copyright owner who has been omitted or incorrectly acknowledged.

Appendices

Appendix A

Linear Equations

A.1 Normal Matrix

$[I^N]$ has the form,

$$[I^N] = \begin{bmatrix} [I^{N_\gamma}] & [I^{N_\lambda}] \\ [I] & [S] \end{bmatrix}, \quad (\text{A.1.1})$$

where $[I]$ is an identity matrix, and $[S]$ contains the panel lengths,

$$[S] = \begin{bmatrix} \frac{s}{2} & \frac{s}{2} & 0 & 0 \\ 0 & \frac{s}{2} & \frac{s}{2} & 0 \\ 0 & 0 & \frac{s}{2} & \frac{s}{2} \\ 0 & 0 & 0 & \frac{s}{2} \end{bmatrix}. \quad (\text{A.1.2})$$

A.2 Pressure Equation

$$\delta p = \frac{1}{2}\rho_f (\underline{U}_\infty \cdot \underline{U}_\infty) - \frac{1}{2}\rho_f (\underline{u}_m \cdot \underline{u}_m) - \rho_f \frac{\delta\phi}{\delta t}. \quad (\text{A.2.1})$$

Where;

$$\underline{u} = \underline{U}_\infty + \underline{u}'_m + \underline{u}^b_m, \quad (\text{A.2.2a})$$

$$\underline{U}_\infty = U_\infty \underline{i} + 0 \underline{j}, \quad (\text{A.2.2b})$$

$$\underline{u}'_m = u_m^{T'} \underline{i} + u_m^{N'} \underline{j} = u_m^{T'} \underline{i} + 0 \underline{j}, \quad (\text{A.2.2c})$$

$$\underline{u}^b_m = u_m^{T_b} \underline{i} + u_m^{N_b} \underline{j} = 0 \underline{i} + u_m^{N_b} \underline{j} \quad (\text{A.2.2d})$$

Inserting Equations A.2.2b, A.2.2a, A.2.2c and A.2.2d in to Equation A.2.1 gives the final linearised pressure equation,

$$\begin{aligned} \delta p_m &= \frac{1}{2} \rho_f (\underline{U}_\infty \cdot \underline{U}_\infty - (\underline{U}_\infty \cdot \underline{U}_\infty + 2 \underline{U}_\infty \cdot \underline{u}'_m + 2 \underline{U}_\infty \cdot \underline{u}^b_m)) - \rho_f \frac{\partial \phi}{\partial t}, \\ &= -\rho_f (\underline{U}_\infty \cdot \underline{u}'_m + \underline{U}_\infty \cdot \underline{u}^b_m) - \rho_f \frac{\partial \phi}{\partial t}, \\ &= -\rho_f \left((U_\infty \underline{i} + 0 \underline{j}) \cdot (u_m^{T'} \underline{i} + 0 \underline{j}) + (U_\infty \underline{i} + 0 \underline{j}) \cdot (0 \underline{i} + u_m^{N_b} \underline{j}) \right) - \rho_f \frac{\partial \phi}{\partial t}, \\ &= -\rho_f U_\infty u_m^{T'} - \rho_f \frac{\partial \phi}{\partial t}, \end{aligned} \quad (\text{A.2.3})$$

hence the pressure acting across the cantilever is,

$$\delta p_m|_{xp} = -2\rho_f U_\infty u_m^{T'} - \rho_f \frac{\partial \phi}{\partial t} \Big|_{xp}. \quad (\text{A.2.4})$$

The second part of Equation A.2.4 is not multiplied by two as the vortex velocity potential influence coefficients are already calculated across the cantilever (Howell [2006]).

A.3 Steady Singularity Strengths

Extending the no-flux/normal boundary condition shown in Equation 3.2.4 to include the wake,

$$\left\{ \begin{array}{c} \gamma \\ \dots \\ \lambda \end{array} \right\} = [I^N]^{-1} \{ \underline{v}_p \cdot \underline{n} - \underline{U}_\infty \cdot \underline{n} - \underline{u}^b \cdot \underline{n} \}, \quad (\text{A.3.1})$$

where the linearised velocity and normal vectors are,

$$\underline{v}_p = \dot{\xi}\underline{i} + \dot{\eta}\underline{j} = 0\underline{i} + \dot{\eta}\underline{j}, \quad (\text{A.3.2a})$$

$$\underline{n} = -\sin\theta\underline{i} + \cos\theta\underline{j} = -\theta\underline{i} + 1\underline{j}. \quad (\text{A.3.2b})$$

Substituting Equations A.2.2b, A.2.2d, A.3.2a and A.3.2b in to Equation A.3.1 gives an expression for the linear singularity strengths,

$$\begin{aligned} \begin{pmatrix} \gamma \\ \dots \\ \lambda \end{pmatrix} &= [I^N]^{-1}\{(0\underline{i} + \dot{\eta}\underline{j}) \cdot (-\theta\underline{i} + 1\underline{j}) - (U_\infty\underline{i} + 0\underline{j}) \cdot (-\theta\underline{i} + 1\underline{j}) - (0\underline{i} + u^{N_b}\underline{j}) \cdot (-\theta\underline{i} + 1\underline{j})\}, \\ &= [I^N]^{-1}\{\dot{\eta} + U_\infty\theta - u^{N_b}\}. \end{aligned} \quad (\text{A.3.3})$$

A.4 Unsteady Singularity Strengths

Taking the time derivative of Equation A.3.1,

$$\frac{\partial}{\partial t} \begin{pmatrix} \gamma \\ \dots \\ \lambda \end{pmatrix} = \frac{\partial}{\partial t} [I^N]^{-1}\{v_p \cdot \underline{n} - U_\infty \cdot \underline{n} - u^b \cdot \underline{n}\} + [I^N]^{-1} \frac{\partial}{\partial t} \{v_p \cdot \underline{n} - U_\infty \cdot \underline{n} - u^b \cdot \underline{n}\} \quad (\text{A.4.1})$$

owing to the linearity of the current model there is no change in the influence coefficients in time, additionally the free-stream flow speed is assumed to be constant, hence,

$$\begin{aligned} \frac{\partial}{\partial t} \begin{pmatrix} \gamma \\ \dots \\ \lambda \end{pmatrix} &= [I^N]^{-1} \frac{\partial}{\partial t} \{v_p \cdot \underline{n} - U_\infty \cdot \underline{n} - u^b \cdot \underline{n}\}, \\ &= [I^N]^{-1} \{\dot{v}_p \cdot \underline{n} + v_p \cdot \dot{\underline{n}} - U_\infty \cdot \dot{\underline{n}} - \dot{u}^b \cdot \underline{n} - u^b \cdot \dot{\underline{n}}\}. \end{aligned} \quad (\text{A.4.2})$$

Taking the time differentials of A.3.2a, A.3.2b and A.2.2d respectively;

$$\dot{\underline{p}} = 0\underline{i} + \dot{\eta}\underline{j}, \quad (\text{A.4.3a})$$

$$\dot{\underline{n}} = -\dot{\theta}\underline{i} + 0\underline{j}, \quad (\text{A.4.3b})$$

$$\dot{\underline{u}}^b = 0\underline{i} + \dot{u}^{N_b}\underline{j}. \quad (\text{A.4.3c})$$

Inserting Equations A.3.2a, A.3.2b, A.2.2d, A.4.3a, A.4.3b and A.4.3c in to Equation A.4.2 results in the calculation for unsteady singularity strengths,

$$\frac{\partial}{\partial t} \begin{Bmatrix} \gamma \\ \dots \\ \lambda \end{Bmatrix} = [I^N]^{-1} \{ \ddot{\eta} + U_\infty \dot{\theta} - \dot{u}^{N_b} \}. \quad (\text{A.4.4})$$

A.5 Expanded Pressure Equation

In the expansion and simplification of the pressure equation (Equation 3.2.23) to arrive at Equation 3.3.1 the following substitutions are made for θ and $\dot{\theta}$,

$$\tan \theta = \frac{\eta_{m+1} - \eta_m}{\delta x}, \quad (\text{A.5.1a})$$

$$\dot{\theta} = \frac{\dot{\eta}_{m+1} - \dot{\eta}_m}{\delta x}. \quad (\text{A.5.1b})$$

With the inclusion of these in Equation 3.2.23 the influence coefficient matrices $[\mathbf{A}]$ and $[\mathbf{B}]$ can be altered so that there is only one η or $\dot{\eta}$ term in the accompanying vector.

A.5.1 A^- and B^- :

This section uses the A-matrix as an example, the same process was applied to the B-matrix. Focusing on the *hydrodynamic stiffness* term in Equation 3.2.23,

the matrix and vector having substituted in Equations A.5.1a and A.5.1b are,

$$\begin{bmatrix} A_{1,1} & A_{1,2} & \cdots & A_{1,m} \\ A_{2,1} & A_{2,2} & \cdots & A_{2,m} \\ \vdots & \vdots & \ddots & \vdots \\ A_{m,1} & A_{m,2} & \cdots & A_{m,m} \end{bmatrix} \begin{Bmatrix} (\eta_1 - \eta_0)/\delta x \\ (\eta_2 - \eta_1)/\delta x \\ \vdots \\ (\eta_m - \eta_{m-1})/\delta x \end{Bmatrix}. \quad (\text{A.5.2})$$

Multiplying out the first line of the matrix as an example gives,

$$\begin{aligned} &\equiv A_{1,1}(\eta_1 - \eta_0) + A_{1,2}(\eta_2 - \eta_1) + \cdots + A_{1,m}(\eta_m - \eta_{m-1}), \\ &\equiv -A_{1,1}\eta_0 + (A_{1,1} - A_{1,2})\eta_2 + \cdots + (A_{1,m-1} - A_{1,m})\eta_{m-1} + A_{1,m}\eta_m. \end{aligned} \quad (\text{A.5.3})$$

Performing the same operation with the remaining lines of the matrix and rearranging gives,

$$\begin{bmatrix} (A_{1,1} - A_{1,2}) & \cdots & (A_{1,m-1} - A_{1,m}) & A_{1,m} \\ (A_{2,1} - A_{2,2}) & \cdots & (A_{2,m-1} - A_{2,m}) & A_{2,m} \\ \vdots & \vdots & \ddots & \vdots \\ (A_{m,1} - A_{m,2}) & \cdots & (A_{m,m-1} - A_{m,m}) & A_{m,m} \end{bmatrix} \begin{Bmatrix} \eta_1 \\ \eta_2 \\ \vdots \\ \eta_m \end{Bmatrix}, \quad (\text{A.5.4})$$

$$= [A^-] \{\eta_m\}. \quad (\text{A.5.5})$$

A.5.2 A^+ :

$$\begin{bmatrix} A_{1,1} & A_{1,2} & \cdots & A_{1,m} \\ A_{2,1} & A_{2,2} & \cdots & A_{2,m} \\ \vdots & \vdots & \ddots & \vdots \\ A_{m,1} & A_{m,2} & \cdots & A_{m,m} \end{bmatrix} \begin{Bmatrix} \dot{\eta}_0 + \dot{\eta}_1 \\ \dot{\eta}_1 + \dot{\eta}_2 \\ \vdots \\ \dot{\eta}_m + \dot{\eta}_{m+1} \end{Bmatrix}. \quad (\text{A.5.6})$$

Expanding and simplifying the first line as before gives,

$$\begin{aligned} &\equiv A_{1,1}(\dot{\eta}_0 + \dot{\eta}_1) + A_{1,2}(\dot{\eta}_1 + \dot{\eta}_2) + \cdots + A_{1,m}(\dot{\eta}_{m-1} + \dot{\eta}_m), \\ &\equiv A_{1,1}\dot{\eta}_0 + (A_{1,1} + A_{1,2})\dot{\eta}_2 + \cdots + (A_{1,m-1} + A_{1,m})\dot{\eta}_{m-1} + A_{1,m}\dot{\eta}_m. \end{aligned} \quad (\text{A.5.7})$$

Which can be rearranged as before to give,

$$\begin{bmatrix} (A_{1,1} + A_{1,2}) & \cdots & (A_{1,m-1} + A_{1,m}) & A_{1,m} \\ (A_{2,1} + A_{2,2}) & \cdots & (A_{2,m-1} + A_{2,m}) & A_{2,m} \\ \vdots & \vdots & \ddots & \vdots \\ (A_{m,1} + A_{m,2}) & \cdots & (A_{m,m-1} + A_{m,m}) & A_{m,m} \end{bmatrix} \begin{Bmatrix} \dot{\eta}_1 \\ \dot{\eta}_2 \\ \vdots \\ \dot{\eta}_m \end{Bmatrix}, \quad (\text{A.5.8})$$

$$= [A^+] \{ \dot{\eta}_m \}. \quad (\text{A.5.9})$$

A.6 The $[I^{N-+}]$ and $[I^{N+}]$ matrices

The summation of vorticity along the length of the beam using the second term in Equation 6 as an example,

$$\sum [I^N]^{-1} \{ \ddot{\eta} \}.$$

Expanding this term as in section A.5,

$$\begin{aligned} & \begin{bmatrix} I_{1,1} & I_{1,2} & \cdots & I_{1,m} \\ I_{2,1} & I_{2,2} & \cdots & I_{2,m} \\ \vdots & \vdots & \ddots & \vdots \\ I_{m,1} & I_{m,2} & \cdots & I_{m,m} \end{bmatrix} \begin{Bmatrix} \ddot{\eta}_1 \\ \ddot{\eta}_2 \\ \vdots \\ \ddot{\eta}_m \end{Bmatrix} \\ & \equiv \begin{aligned} & I_{1,1}\ddot{\eta}_1 + I_{1,2}\ddot{\eta}_2 + \cdots + I_{1,m}\ddot{\eta}_m + \\ & I_{2,1}\ddot{\eta}_1 + I_{2,2}\ddot{\eta}_2 + \cdots + I_{2,m}\ddot{\eta}_m + \\ & \vdots \\ & I_{m,1}\ddot{\eta}_1 + I_{m,2}\ddot{\eta}_2 + \cdots + I_{m,m}\ddot{\eta}_m. \end{aligned} \end{aligned}$$

Arranging back into a matrix form gives,

$$\begin{bmatrix} (I_{1,1} + I_{2,1} + \cdots + I_{m,1}) & (I_{1,2} + I_{2,2} + \cdots + I_{m,2}) & \cdots & (I_{1,m} + I_{2,m} + \cdots + I_{m,m}) \end{bmatrix} \begin{Bmatrix} \ddot{\eta}_1 \\ \ddot{\eta}_2 \\ \vdots \\ \ddot{\eta}_m \end{Bmatrix},$$

$$= \left[[\mathbf{I}^N]^{-1} \right]^+ \{ \ddot{\eta} \} \quad (\text{A.6.1})$$

The same method applies to the $[I^N]^{-1-+}$ and $[I^N]^{-1++}$ matrices.

Appendix B

Non-linear Equations

B.1 Non-linear Beam Discretization

The discretization of the non-linear beam equation is shown in Equation B.1.1b.

$$\begin{aligned}
 -\delta p|_{\text{xp}} &= \rho h \ddot{\eta}_s + \rho h \frac{\partial \eta}{\partial s} \int_0^s \left(\left(\frac{\partial^2 \eta}{\partial t \partial s} \right)^2 + \frac{\partial \eta}{\partial s} \frac{\partial^3 \eta}{\partial t^2 \partial s} \right) ds \\
 &\quad - \rho h \frac{\partial^2 \eta}{\partial s^2} \int_s^L \int_0^s \left(\left(\frac{\partial^2 \eta}{\partial t \partial s} \right)^2 + \frac{\partial \eta}{\partial s} \frac{\partial^3 \eta}{\partial t^2 \partial s} \right) ds ds \\
 &\quad + B \left[\frac{\partial^4 \eta}{\partial s^4} + \frac{\partial^4 \eta}{\partial s^4} \left(\frac{\partial \eta}{\partial s} \right)^2 + 4 \frac{\partial \eta}{\partial s} \frac{\partial^2 \eta}{\partial s^2} \frac{\partial^3 \eta}{\partial s^3} + \left(\frac{\partial^2 \eta}{\partial s^2} \right)^3 \right], \quad (\text{B.1.1a})
 \end{aligned}$$

$$\begin{aligned}
 -\delta p(\ddot{\eta}, \dot{\eta}, \eta) &= \rho h [\mathbf{I}] \ddot{\eta} + \rho h [\mathbf{D}_1] \eta [\Delta_0^s] \left(([\mathbf{D}_1] \dot{\eta})^2 + [\mathbf{D}_1] \eta [\mathbf{D}_1] \ddot{\eta} \right) \Delta s \\
 &\quad - \rho h [\mathbf{D}_2] \eta [\Delta_s^L] [\Delta_0^s] \left(([\mathbf{D}_1] \dot{\eta})^2 + [\mathbf{D}_1] \eta [\mathbf{D}_1] \ddot{\eta} \right) \Delta s \Delta s \\
 &\quad + B \left[[\mathbf{D}_4] \eta + [\mathbf{D}_4] \eta ([\mathbf{D}_1] \eta)^2 \right. \\
 &\quad \left. + 4 [\mathbf{D}_1] \eta [\mathbf{D}_2] \eta [\mathbf{D}_3] \eta + ([\mathbf{D}_2] \eta)^3 \right]. \quad (\text{B.1.1b})
 \end{aligned}$$

Which can be represented as,

$$-\delta p(\ddot{\eta}, \dot{\eta}, \eta) = \rho h [\mathbf{I}] \ddot{\eta} + \delta p''. \quad (\text{B.1.2a})$$

Where $[\mathbf{D}_1]$, $[\mathbf{D}_2]$, $[\mathbf{D}_3]$, and $[\mathbf{D}_4]$ are centred spatial differencing matrices of increasing order (1st to 4th) given by,

$$[\mathbf{D}_1] = \begin{bmatrix} 1 & 0 & 0 & 0 & 0 \\ -1 & 0 & 1 & 0 & 0 \\ 0 & -1 & 0 & 1 & 0 \\ 0 & 0 & -1 & 0 & 1 \\ 0 & 0 & 0 & 2 & -2 \end{bmatrix} \frac{1}{2\Delta_s}, \quad (\text{B.1.3a})$$

$$[\mathbf{D}_2] = \begin{bmatrix} -2 & 1 & 0 & 0 & 0 \\ 1 & -2 & 1 & 0 & 0 \\ 0 & 1 & -2 & 1 & 0 \\ 0 & 0 & 1 & -2 & 1 \\ 0 & 0 & 0 & 0 & 0 \end{bmatrix} \frac{1}{\Delta_s^2}, \quad (\text{B.1.3b})$$

$$[\mathbf{D}_3] = \begin{bmatrix} -2 & 1 & 0 & 0 & 0 \\ 2 & 0 & -2 & 1 & 0 \\ -1 & 2 & 0 & -2 & 1 \\ 0 & -1 & 2 & -1 & 0 \\ 0 & 0 & -1 & 2 & -1 \end{bmatrix} \frac{1}{2\Delta_s^3}, \quad (\text{B.1.3c})$$

$$[\mathbf{D}_4] = \begin{bmatrix} 6 & -4 & 1 & 0 & 0 \\ -4 & 6 & -4 & 1 & 0 \\ 1 & -4 & 6 & -4 & 1 \\ 0 & 1 & -4 & 5 & 2 \\ 0 & 0 & 1 & -2 & 1 \end{bmatrix} \frac{1}{\Delta_s^4}. \quad (\text{B.1.3d})$$

The $[\Delta_0^s]$ and $[\Delta_s^L]$ matrices are summation matrices and take the form,

$$[\Delta_0^s] = \begin{bmatrix} 1 & 0 & 0 & 0 & 0 \\ 1 & 1 & 0 & 0 & 0 \\ 1 & 1 & 1 & 0 & 0 \\ 1 & 1 & 1 & 1 & 0 \\ 1 & 1 & 1 & 1 & 1 \end{bmatrix}, \quad (\text{B.1.4a})$$

$$[\Delta_s^L] = \begin{bmatrix} 1 & 1 & 1 & 1 & 1 \\ 0 & 1 & 1 & 1 & 1 \\ 0 & 0 & 1 & 1 & 1 \\ 0 & 0 & 0 & 1 & 1 \\ 0 & 0 & 0 & 0 & 1 \end{bmatrix}. \quad (\text{B.1.4b})$$

B.2 Steady and Unsteady Singularity Strengths

The velocity at a point on the plate is given $\underline{v}_p = \underline{U}_\infty + \underline{u}' + \underline{u}^b$, and hence the normal velocity on a panel is given by,

$$\underline{v}_p \cdot \underline{n} = \underline{U}_\infty \cdot \underline{n} + \underline{u}' \cdot \underline{n} + \underline{u}^b \cdot \underline{n}, \quad (\text{B.2.1})$$

$$\underline{u}' \cdot \underline{n} = [\mathbf{I}^N] \{\gamma\} = \{\underline{v}_p \cdot \underline{n} - \underline{U}_\infty \cdot \underline{n} - \underline{u}^b \cdot \underline{n}\}. \quad (\text{B.2.2})$$

Where,

$$\underline{u}' = u^{T'} \underline{i} + u^{N'} \underline{j}, \quad (\text{B.2.3a})$$

$$\underline{u}^b = u^{T'b} \underline{i} + u^{N'b} \underline{j}, \quad (\text{B.2.3b})$$

$$\underline{U}_\infty = U_\infty \underline{i} + 0 \underline{j}, \quad (\text{B.2.3c})$$

$$\underline{v}_p = \dot{\xi} \underline{i} + \dot{\eta} \underline{j}, \quad (\text{B.2.3d})$$

$$\underline{n} = -\sin \theta \underline{i} + \cos \theta \underline{j}. \quad (\text{B.2.3e})$$

The steady non-linear singularity strengths are therefore,

$$\{\gamma\} = [\mathbf{I}^N]^{-1} \{(U_\infty - \dot{\xi} + u^{T'b}) \sin \theta + (\dot{\eta} - u^{N'b}) \cos \theta\}. \quad (\text{B.2.4})$$

Taking the time derivative of Equation B.2.4 the unsteady non-linear singularity strengths can be determined and are given by,

$$\dot{v}_p \cdot \underline{n} + \underline{v}_p \cdot \dot{\underline{n}} = \underbrace{\dot{U}_\infty \cdot \underline{n} + U_\infty \cdot \dot{\underline{n}}}_{=0} + \dot{u}' \cdot \underline{n} + \underline{u}' \cdot \dot{\underline{n}} + \dot{u}^b \cdot \underline{n} + \underline{u}^b \cdot \dot{\underline{n}}, \quad (\text{B.2.5a})$$

$$\begin{aligned} [\mathbf{I}^{\dot{\mathbf{N}}}] \{\dot{\gamma}\} + [\mathbf{I}^{\mathbf{N}}] \{\dot{\gamma}\} &= (-\ddot{\xi} - \dot{\eta}\dot{\theta} + \dot{u}^{T'b} + u^{N'b}\dot{\theta}) \sin \theta \\ &+ (\ddot{\eta} - \dot{\xi}\dot{\theta} + U_\infty\dot{\theta} - \dot{u}^{N'b} + u^{T'b}\dot{\theta}) \cos \theta, \end{aligned} \quad (\text{B.2.5b})$$

$$\begin{aligned} \{\dot{\gamma}\} &= [\mathbf{I}^{\mathbf{N}}]^{-1} \left\{ (-\ddot{\xi} - \dot{\eta}\dot{\theta} + \dot{u}^{T'b} + u^{N'b}\dot{\theta}) \sin \theta \right. \\ &+ (\ddot{\eta} - \dot{\xi}\dot{\theta} + U_\infty\dot{\theta} - \dot{u}^{N'b} + u^{T'b}\dot{\theta}) \cos \theta \left. \right\} \\ &- [\mathbf{I}^{\mathbf{N}}]^{-1} [\mathbf{I}^{\dot{\mathbf{N}}}] \{\dot{\gamma}\}. \end{aligned} \quad (\text{B.2.5c})$$

B.2.1 Tangential Perturbation Velocity

The tangential perturbation velocity is given by $[\mathbf{I}^{\mathbf{T}}]\gamma$ and is therefore,

$$u^{T'} = [\mathbf{I}^{\mathbf{T}}][\mathbf{I}^{\mathbf{N}}]^{-1} \left\{ (U_\infty - \dot{\xi} + u^{T'b}) \sin \theta + (\dot{\eta} - u^{N'b}) \cos \theta \right\}, \quad (\text{B.2.6a})$$

$$= [\mathbf{B}_1] \left\{ (U_\infty - \dot{\xi} + u^{T'b}) \sin \theta + (\dot{\eta} - u^{N'b}) \cos \theta \right\}. \quad (\text{B.2.6b})$$

B.2.2 Unsteady Velocity Potential

Equations B.2.4 and B.2.5c are substituted into Equation 7.2.10b to give,

$$\frac{\partial \phi}{\partial t} = [\mathbf{I}^\phi] \dot{\gamma} + [\mathbf{I}^{\dot{\phi}}] \gamma, \quad (\text{B.2.7a})$$

$$\begin{aligned} [\mathbf{I}^\phi] \dot{\gamma} &= [\mathbf{I}^\phi][\mathbf{I}^{\mathbf{N}}]^{-1} \left\{ (-\ddot{\xi} - \dot{\eta}\dot{\theta} + \dot{u}^{T'b} + u^{N'b}\dot{\theta}) \sin \theta + (\ddot{\eta} - \dot{\xi}\dot{\theta} + U_\infty\dot{\theta} - \dot{u}^{N'b} + u^{T'b}\dot{\theta}) \cos \theta \right\} - \\ &[\mathbf{I}^\phi][\mathbf{I}^{\mathbf{N}}]^{-1} [\mathbf{I}^{\dot{\mathbf{N}}}] [\mathbf{I}^{\mathbf{N}}]^{-1} \left\{ (U_\infty - \dot{\xi} + u^{T'b}) \sin \theta + (\dot{\eta} - u^{N'b}) \cos \theta \right\}, \end{aligned} \quad (\text{B.2.7b})$$

$$\begin{aligned} &= [\mathbf{B}_2] \left\{ (-\ddot{\xi} - \dot{\eta}\dot{\theta} + \dot{u}^{T'b} + u^{N'b}\dot{\theta}) \sin \theta + (\ddot{\eta} - \dot{\xi}\dot{\theta} + U_\infty\dot{\theta} - \dot{u}^{N'b} + u^{T'b}\dot{\theta}) \cos \theta \right\} - \\ &[\mathbf{B}_3] \left\{ (U_\infty - \dot{\xi} + u^{T'b}) \sin \theta + (\dot{\eta} - u^{N'b}) \cos \theta \right\}, \end{aligned} \quad (\text{B.2.7c})$$

$$[\mathbf{I}^{\dot{\phi}}] \gamma = [\mathbf{I}^\phi][\mathbf{I}^{\mathbf{N}}]^{-1} \left\{ (U_\infty - \dot{\xi} + u^{T'b}) \sin \theta + (\dot{\eta} - u^{N'b}) \cos \theta \right\}, \quad (\text{B.2.7d})$$

$$= [\mathbf{B}_4] \left\{ (U_\infty - \dot{\xi} + u^{T'b}) \sin \theta + (\dot{\eta} - u^{N'b}) \cos \theta \right\}, \quad (\text{B.2.7e})$$

$$\begin{aligned} \therefore \frac{\partial \phi}{\partial t} &= [\mathbf{B}_2] \left\{ (-\ddot{\xi} - \dot{\eta}\dot{\theta} + \dot{u}^{T'b} + u^{N'b}\dot{\theta}) \sin \theta + (\ddot{\eta} - \dot{\xi}\dot{\theta} + U_\infty\dot{\theta} - \dot{u}^{N'b} + u^{T'b}\dot{\theta}) \cos \theta \right\} + \\ &[[\mathbf{B}_4] - [\mathbf{B}_3]] \left\{ (U_\infty - \dot{\xi} + u^{T'b}) \sin \theta + (\dot{\eta} - u^{N'b}) \cos \theta \right\}. \end{aligned} \quad (\text{B.2.7f})$$

B.3 Pressure Equation

Following a streamline from far upstream to a point on the beam yields,

$$\delta p = \frac{1}{2}\rho_f (\underline{U}_\infty \cdot \underline{U}_\infty - \underline{u}_m \cdot \underline{u}_m) - \rho_f \frac{\partial \phi}{\partial t}. \quad (\text{B.3.1})$$

Where,

$$\underline{u}_m = \underline{U}_\infty + \underline{u}'_m + \underline{u}^b_m, \quad (\text{B.3.2a})$$

$$\underline{U}_\infty = U_\infty \underline{i} + 0 \underline{j}, \quad (\text{B.3.2b})$$

$$\underline{u}'_m = u^{T'} \underline{i} + u^{N'} \underline{j}, \quad (\text{B.3.2c})$$

$$\underline{u}^b_m = u^{T_b} \underline{i} + u^{N_b} \underline{j}. \quad (\text{B.3.2d})$$

These are the non-linear versions of the vectors listed as Equations A.2.2b, A.2.2a, A.2.2c and A.2.2d in Section A.2. The total velocity, \underline{u}_m , is therefore given by,

$$\underline{u} = (\underline{U}_\infty \cdot \underline{t} + \underline{u}' \cdot \underline{t} + \underline{u}^b \cdot \underline{t}) \underline{t} + \underbrace{(\underline{U}_\infty \cdot \underline{n} + \underline{u}' \cdot \underline{n} + \underline{u}^b \cdot \underline{n})}_{=v_p \cdot \underline{n}} \underline{n}, \quad (\text{B.3.3a})$$

$$= (U_\infty \cos \theta + u^{T'} + u^{T'_b} \cos \theta + u^{N'_b} \sin \theta) \underline{t} + (\dot{\eta} \cos \theta - \dot{\xi} \sin \theta) \underline{n}, \quad (\text{B.3.3b})$$

$$\therefore \underline{u} \cdot \underline{u} = (U_\infty \cos \theta + u^{T'} + u^{T'_b} \cos \theta + u^{N'_b} \sin \theta)^2 + (\dot{\eta} \cos \theta - \dot{\xi} \sin \theta)^2. \quad (\text{B.3.3c})$$

Where \underline{t} and \underline{n} replace \underline{i} and \underline{j} as the panels no longer align with these axes. Placing Equation B.3.3c into Equation B.3.1 gives,

$$\delta p = \frac{1}{2}\rho_f (U_\infty^2 - (U_\infty \cos \theta + u^{T'} + u^{T'_b} \cos \theta + u^{N'_b} \sin \theta)^2 - (\dot{\eta} \cos \theta - \dot{\xi} \sin \theta)^2) - \rho_f \frac{\partial \phi}{\partial t}. \quad (\text{B.3.4})$$

Using the conventions for the normal and tangential velocities outlined in Figure B.1 Equation B.3.4 allows the calculation of the pressure on the upper and lower

surfaces of the plate,

$$\begin{aligned}
p_U &= \frac{1}{2}\rho_f \left(U_\infty^2 - (U_\infty \cos \theta)^2 - u^{T'2} - (u^{T'_b} \cos \theta)^2 - (u^{N'_b} \sin \theta)^2 \right. \\
&\quad - 2U_\infty u^{T'} \cos \theta - 2U_\infty u^{T'_b} \cos^2 \theta - 2U_\infty u^{N'_b} \sin \theta \cos \theta \\
&\quad - 2u^{T'} u^{T'_b} \cos \theta - 2u^{T'} u^{N'_b} \sin \theta \\
&\quad \left. - 2u^{T'_b} u^{N'_b} \sin \theta \cos \theta \right), \tag{B.3.5a}
\end{aligned}$$

$$\begin{aligned}
p_L &= \frac{1}{2}\rho_f \left(U_\infty^2 - (U_\infty \cos \theta)^2 - u^{T'2} - (u^{T'_b} \cos \theta)^2 - (u^{N'_b} \sin \theta)^2 \right. \\
&\quad + 2U_\infty u^{T'} \cos \theta - 2U_\infty u^{T'_b} \cos^2 \theta - 2U_\infty u^{N'_b} \sin \theta \cos \theta \\
&\quad + 2u^{T'} u^{T'_b} \cos \theta + 2u^{T'} u^{N'_b} \sin \theta \\
&\quad \left. - 2u^{T'_b} u^{N'_b} \sin \theta \cos \theta \right). \tag{B.3.5b}
\end{aligned}$$

Taking the difference between Equations B.3.5a and B.3.5b yields the overall pressure difference across the plate,

$$\begin{aligned}
\delta p|_{xp} &= p_U - p_L \\
&= \frac{1}{2}\rho_f \left(-4U_\infty u^{T'} \cos \theta - 4u^{T'} u^{T'_b} \cos \theta - 4u^{T'} u^{N'_b} \sin \theta \right) - \rho_f \frac{\partial \phi}{\partial t} \Big|_{xp} \tag{B.3.6}
\end{aligned}$$

$$= -2\rho_f u^{T'} (U_\infty \cos \theta + u^{T'_b} \cos \theta + u^{N'_b} \sin \theta) - \rho_f \frac{\partial \phi}{\partial t} \Big|_{xp}. \tag{B.3.7}$$

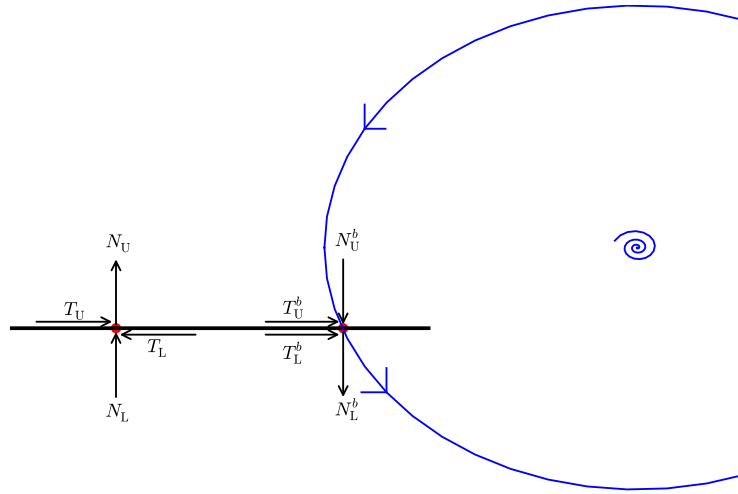


Figure B.1: Normal and tangential directions on the upper and lower surfaces of wake-induced and plate-induced velocities.